

Electrical Impedance Spectroscopy-derived 3D Conductivity Tomography for Atherosclerosis Detection

Thesis by
Zi-Yu Huang

In Partial Fulfillment of the Requirements for the
Degree of
Doctor of Philosophy in Medical Engineering

The logo for the California Institute of Technology (Caltech), featuring the word "Caltech" in a bold, orange, sans-serif font.

CALIFORNIA INSTITUTE OF TECHNOLOGY
Pasadena, California

2022
Defended December 9, 2021

© 2022

Zi-Yu Huang

ORCID: 0000-0001-5998-3097

All rights reserved except where otherwise noted

ACKNOWLEDGEMENTS

I would like to thank my faculty advisor, Yu-Chong Tai, for his dedication to research and consistent technical advice regarding the work described herein. My sincere thanks to the other committee members, Lihong Wang, Azita Emami, and Wei Gao for their assistance and advice. To everyone in the MEMS lab; Allen, Suhash, Haixu, Jake, Shane, Colin, Nick, and Aubrey for many useful conversations and contributing both directly and indirectly to this work. Special thanks to Dr. Yuan Luo for all of his guidance throughout my Ph.D., even after leaving the MEMS lab. Christine and Trevor; thank you for all your assistance and support. None of my work could have been completed without you.

To my collaborators from University of California, Los Angeles. Parinaz Abiri and Chih-Chiang Chang, thank you for your hard work on both the animal and human studies. Special thanks to Dr. Sandra Duarte-Vogel, Dr. Rene Packard, and Dr. Peyman Benharash for your assistance on the swine model. Thanks to Dr. Zhaoping Li and Dr. Holden Wu for facilitating the human studies and MRI work. Lastly, thanks to my collaborators from Amgen, Dr. Bruce Eu and Dr. Chia-Jung Wu for our work on autoinjectors and the associated funding.

A special thanks to my roommates, Yun-Ting Chang and Chien-I Yang for their emotional support throughout the challenging moments during my Ph.D. Everyone from the Taiwanese Association at Caltech, thanks for holding all sorts of dining and social events. And finally my parents, my family in Taiwan, and my old friend Tai-Ying Lee.

I want to acknowledge Sensors and Actuators: B. Chemical, Scientific Reports, and IEEE Transactions on Biomedical Engineering for permission to include and adapt previously published material from my manuscripts in Chapters 2, 3, and 4. Finally, thanks to the Taiwan-Caltech Scholarship for supporting my Ph.D.

ABSTRACT

Electrical impedance tomography (EIT) utilizes voltage/current data measured from the surface of interest to reconstruct the electrical conductivity distribution. This results in a noninvasive medical imaging procedure with many applications. Some examples would be: lung ventilation monitoring, breast cancer detection, and fatty liver detection. Non-alcoholic fatty liver disease (NAFLD) is one of the most common causes of cardiometabolic diseases in overweight individuals. The gold standard for NAFLD diagnosis is a liver biopsy which is a risky and invasive procedure. A non-invasive and cost effective method to detect fatty liver is an important unmet clinical need. Due to the distinct electrical properties of fatty tissue versus normal tissue, EIT can be applied to detect the fat infiltrate in the liver. We conducted EIT measurements and reconstructions on 19 subjects where the fat infiltrate was validated by MRI proton-density fat fraction (PDFF). The liver EIT conductivity was shown to be inversely correlated with MRI PDFF, demonstrating the ability of EIT to detect fatty infiltrate in the liver.

This thesis also extends the EIT reconstruction to detect atherosclerosis, which is a build-up of fatty tissue in the arteries (plaque). Some plaques are prone to rupture and the current gold standard has a false negative rate of 20 % when distinguishing between vulnerable plaque and stable plaque. We sought to use EIT to detect the fatty content (mainly oxidize LDL) inside these vulnerable plaques. Therefore, the reconstruction method was modified into an outward setting that can measure from the inner surface of interest. *Ex vivo* experiments have demonstrated the ability to detect the location of fatty tissue in swine aorta. This technique has the potential to detect vulnerable plaque. However, the dimension of the device and the required electrode number limits the application from *in vivo* animal artery experiments.

Finally EIS-derived EIT, a new method we proposed, utilizes impedance values at a fixed frequency to solve for the conductivity distribution. This approach circumvents the mathematically ill-posed problem found when performing traditional EIT methods. We designed a 6-point EIS electrode array that was circumferentially configured to a balloon catheter and deployed in Yorkshire mini-pigs with induced stenosis in the right carotid artery. The EIS spectra demonstrated an elevated impedance in the right carotid arteries and the EIS-derived EIT mappings were reconstructed. The low conductivity regions in the EIS-derived EIT mappings were correlated with the positive E06 immunostaining for oxLDL-laden regions.

Thus, we establish the capability of 3D EIS-derived EIT to detect oxLDL-laden arterial walls with translational implication to predict metabolically active plaques prone to acute coronary syndromes.

PUBLISHED CONTENT AND CONTRIBUTIONS

- [1] P. Abiri, Y. Luo, Z.-Y. Huang, Q. Cui, S. Duarte-Vogel, M. Roustaei, C.-C. Chang, X. Xiao, R. Packard, S. Cavallero, *et al.*, “3-dimensional electrical impedance spectroscopy for in situ endoluminal mapping of metabolically active plaques,” *Sensors and Actuators B: Chemical*, p. 131–152, 2021. DOI: 10.1016/j.snb.2021.131152,
Z.-Y. Huang designed and performed the experiments, conducted the EIS-derived EIT reconstructions and analyses, performed the computational modeling, and participated in the writing of the manuscript.
- [2] C.-C. Chang, Z.-Y. Huang, S.-F. Shih, Y. Luo, A. Ko, Q. Cui, J. Sumner, S. Cavallero, S. Das, W. Gao, *et al.*, “Electrical impedance tomography for non-invasive identification of fatty liver infiltrate in overweight individuals,” *Scientific Reports*, vol. 11, no. 1, pp. 1–12, 2021. DOI: 10.1038/s41598-021-99132-z,
Z.-Y. Huang participated in the EIT measurements, conducted the EIT reconstructions and analyses, and participated in the writing of the manuscript.
- [3] Y. Luo, D. Huang, Z.-Y. Huang, T. K. Hsiai, and Y.-C. Tai, “An ex vivo study of outward electrical impedance tomography (oeit) for intravascular imaging,” *IEEE Transactions on Biomedical Engineering*, 2021. DOI: 10.1109/TBME.2021.3104300,
Z.-Y. Huang conducted the *ex vivo* measurements and collected the data.
- [4] Z.-Y. Huang, Y. Luo, P. Abiri, R. R. Packard, T. K. Hsiai, and Y.-C. Tai, “Double-ballooned local drug delivery catheter with blood bypassing function,” in *2019 20th International Conference on Solid-State Sensors, Actuators and Microsystems & Eurosensors XXXIII (TRANSDUCERS & EUROSENSORS XXXIII)*, IEEE, 2019, pp. 2213–2216,
Z.-Y. Huang designed and fabricated the device, performed the experiments and participated in the writing of the manuscript.

TABLE OF CONTENTS

Acknowledgements	iii
Abstract	iv
Published Content and Contributions	vi
Table of Contents	vi
List of Illustrations	ix
List of Tables	xvi
Chapter I: Introduction to Electrical Impedance-based Methodologies	1
1.1 Electrical Impedance Spectroscopy	1
1.2 Electrical Impedance Tomography	8
1.3 Summary	14
Chapter II: EIT for Fatty Liver Detection	16
2.1 Fatty Liver	16
2.2 Previous EIT Studies for Fatty Liver Detection	18
2.3 Human Study Recruitment	19
2.4 MRI Scan and PDFF	21
2.5 EIT Experiments	23
2.6 Reconstruction of the EIT Images	28
2.7 EIT and PDFF Correlation	33
2.8 Correlation Analyses with the Demographics Data	36
2.9 Discussion	39
2.10 Summary	41
Chapter III: An Improved EIT Algorithm for 3D Reconstruction and Differ- ential EIT	42
3.1 3D Reconstruction of EIT	42
3.2 EIT Reconstruction without MRI	43
3.3 Preliminary Results for fdEIT	44
3.4 Summary	46
Chapter IV: Outward EIT for Intravascular Imaging	48
4.1 Outward EIT Device and Experimental Setup	48
4.2 <i>ex vivo</i> Experimental Results	52
4.3 Discussion	55
4.4 Summary	56
Chapter V: EIS-derived Electrical Impedance Tomography	57
5.1 Theoretical Framework for EIS-derived EIT	57
5.2 3D Model of the Reconstruction	58
5.3 Initial Conductivity	61
5.4 Optimization of the Conductivity Distribution	65
5.5 Matlab Implementation	66
5.6 Summary	67

Chapter VI: EIS Application for Atherosclerosis Detection	68
6.1 Atherosclerosis	68
6.2 Previous Study of EIS on Plaque Detection	70
6.3 EIS Balloon Catheter	72
6.4 EIS Experiments	77
6.5 Animal Study Design	79
6.6 Histology and Immunostaining	83
6.7 EIS-derived Electrical Conductivity Maps	86
6.8 Reconstruction of Histology-based Modeling	91
6.9 Discussion	96
6.10 Summary	97
Chapter VII: 12-point EIS for Atherosclerosis Detection	98
7.1 12-point Device	98
7.2 EIS Measurement Procedure	99
7.3 Preliminary Reconstruction Result	100
7.4 Summary	103
Chapter VIII: Future Work	104
Bibliography	107
Appendix A: EIT Reconstruction Code	119
Appendix B: EIS Reconstruction Code	123

LIST OF ILLUSTRATIONS

<i>Number</i>	<i>Page</i>
1.1 Nyquist plot (left) and Bode plot (right) for a simplified Randles circuit. Note, the Nyquist plot for a Randles cell is always a semi-circle with a diameter equal to the magnitude of the charge transfer resistance. The value of the real axis at the high frequency intercept gives the solution resistance. Adapted from reference [8]	3
1.2 Simplified illustration of the double layer at the electrode-electrolyte interface. The positively charged oxidants diffuse toward the electrode with negative charge and become the reductants after accepting the electrons from the electrode at the interface. IHP and OHP define the inner and outer Helmholtz planes, respectively.[9] Adapted from reference [10].	4
1.3 The associated circuit for the Randles Cell, where R_e , C_{dl} , R_{ct} , and Z_w are electrolyte resistance, double layer capacitance, charge transfer resistance, and Warburg impedance, respectively.	5
1.4 Illustration of the simplified equivalent electrical circuit model for tissue. Note the resistance from the intracellular fluid and extracellular fluid and the capacitance from the cell membrane. Adapted from reference [17].	6
1.5 Cartoon depiction of the electrical current at different frequencies and how it flows through the tissue. Adapted from reference [19]. . .	7
1.6 An example impedance Bode plot for biological tissue. Adapted from reference [20].	8
1.7 Schematic of electrodes positions and MRI markers on the abdomen surface with respect to liver and other organs positions.	10
1.8 Schematic flowchart of the EIT reconstruction. A regularized Gauss-Newton solver is applied for solving the inverse problem.	11
1.9 Illustration showing (A) electrodes distribution with respect to the thorax, (B) the reconstruction mesh, and (C) image obtained during ventilation. Adapted from reference [22].	14

1.10	Impedance maps from EIT and “silent spaces” values at different levels of positive end-expiratory pressure. Adapted from reference [21].	14
2.1	Schematic diagram and liver biopsy images of different stages in NAFLD progression including simple steatosis, NASH, fibrosis/cirrhosis, and hepatocellular carcinoma. Adapted from reference [40].	17
2.2	Schematic workflow of the comparison and validation of the MRI and EIT studies. Volunteers were recruited according to the UCLA Institutional Human Subjects Protection Committee. Multi-echo MRI scans were performed to provide the liver anatomy and proton density fat fraction, and were followed by EIT measurements. Finally, EIT conductivity maps were reconstructed and the MRI PDFF was used to quantify fatty liver infiltrate, and to compare with EIT liver conductivity. Adapted from reference [28].	19
2.3	Human subject recruitment flow chart.	21
2.4	Example ROI on one slice of the PDFF image, avoiding blood vessels and imaging artifacts.	23
2.5	Photo of the SenTec EIT Pioneer set used for EIT measurements.	24
2.6	Software interface showing the impedance values of the 32 electrodes.	25
2.7	Software interface and the programmable current setting.	26
2.8	Schematic of the EIT current injection and voltage recording. The “Skipping 4” pattern was used for both current injection and voltage acquisition. 4 electrodes separated each pair of stimulating and detecting electrodes.	27
2.9	Software interface showing the IQ plot (upper left).	28
2.10	The required <i>a priori</i> knowledge needed for EIT reconstruction. The geometric information obtained from MRI images is incorporated to stabilize the ill-posed inverse problem. This includes the abdomen outer boundary, the peripheral boundary, and the liver boundary.	29
2.11	MRI multi-echo and EIT images for subjects 1-4. The transverse MRI images show the liver anatomy, the fat fractions provide the corresponding MRI PDFF, annotation reveals the liver boundary condition following image segmentation, and 2D EIT images unveil the abdomen conductivity distribution and average liver conductivity.	30
2.12	MRI multi-echo and EIT images for subjects 5-8.	31
2.13	MRI multi-echo and EIT images for subjects 9-12.	31

2.14	MRI multi-echo and EIT images for subjects 13-16.	32
2.15	MRI multi-echo and EIT images for subjects 17-19.	32
2.16	Statistical analyses of BMI vs. MRI PDFF and vs. EIT liver conductivity. (A) BMI values are not significantly correlated with MRI PDFF. (Pearson correlation coefficient $R = -0.037$, $p = 0.89$, $n = 16$.) (B) BMI values are also not significantly correlated with EIT liver conductivity values ($R = -0.19$, $p = 0.47$, $n = 16$.)	34
2.17	Statistical analysis of BMI vs. MRI PDFF and vs. EIT liver conductivity. EIT liver conductivity values were negatively correlated with MRI PDFF ($R = -0.69$, $p = 0.003$, $n = 16$). The shaded region reflects the 95% confidence intervals of the linear slopes.	35
2.18	Analysis of EIT liver conductivity vs. MRI PDFF for all subjects and results excluding anemic subjects. (A) The negative correlation between EIT conductivity and MRI PDFF was reduced to $R = -0.21$ in the presence of preexisting medical conditions ($p = 0.4$, $n = 18$). (B) The correlation between EIT liver vs. MRI PDFF was increased to $R = -0.70$ in the absence of anemia subjects ($p = 0.0049$, $n = 14$). The shaded areas reflect the 95% confidence intervals of the linear slopes.	36
2.19	MRI PDFF vs. age, waist, height, and weight. The Pearson's correlation coefficients (R) and p values were analyzed for (A) age, (B) waist circumference, (C) height, and (D) weight. The circles denote female subjects and the triangles denote male subjects. The 95% confidence intervals of the linear slopes are illustrated as the shaded area. R values are -0.13 for age ($p = 0.64$, $n = 16$), -0.23 for waist circumference ($p = 0.4$, $n = 16$), 0.59 for height ($p = 0.016$, $n = 16$), and -0.41 for weight ($p = 0.12$, $n = 16$), demonstrating low to intermediate correlation with MRI PDFF.	38
2.20	EIT liver conductivity vs. age, waist, height, and weight. The R values for age ($R = -0.1$, $p = 0.71$, $n = 16$), waist circumference ($R = -0.05$, $p = 0.85$, $n = 16$), height ($R = -0.63$, $p = 0.0092$, $n = 16$), and weight ($R = -0.19$, $p = 0.47$, $n = 16$) demonstrate low to intermediate correlation with EIT conductivity.	39
3.1	3D rendering images of (A) liver anatomy, (B) MRI PDFF, and (C) EIT liver conductivity. Scale bar: 5 cm.	43

3.2	Representative 2D differential EIT images compared with MRI images. The voltage data was acquired at 50 kHz and 250 kHz for 2D differential EIT reconstruction. The peripheral boundary is marked in black.	45
3.3	Representative MRI and EIT images. Only the abdomen boundary information was acquired using an MRI. The peripheral boundary information was reconstructed by differential EIT and the liver boundary was assumed.	46
3.4	Correlation between MRI PDFF (%) and EIT liver conductivity (S/m). (A) The liver conductivity distribution was reconstructed within the abdomen including the liver (in purple). But the two regions (in yellow) closer to the electrodes were selected by average conductivity calculations. (B) EIT liver conductivity values were negatively correlated with MRI PDFF ($R = -0.54$, $p = 0.05$, $n = 13$). The shaded area reflects the 95 % confidence intervals of the linear slope.	46
4.1	Schematics of the outward EIT device and experimental setup. (A) The OEIT device with 32 electrodes wrapped around the cylindrical rod as a catheter. (B) A close-up view of the fat tissue placement inside the aorta filled with real blood. (C) A side view of the setup configuration.	50
4.2	Schematic for the reconstruction model.	51
4.3	Reconstruction images of the 4 different fat tissue sizes immersed in real blood inside an aorta lumen.	52
4.4	The regions of interest identified from the tomographic imaging for all conditions. The area stenosis percentage is the ratio of the area in blue to the overall area.	54
4.5	Comparison of area stenosis between real samples and tomographic imaging extracted results.	55
5.1	Schematic for the EIS-derived EIT.	58
5.2	A comparison between before and after Pt-black electroplating which demonstrates a significant decrease in contact impedance.	59

5.3	Schematics for the model. (A) The arterial wall was comprised of three rings: inner and outer define the smooth muscle while the third ring represents collagen. (B) The vessel wall was divided into 8 layers in the z dimension. (C) Each ring contains 36 elements separated by 10 degrees. (D) The 3D model of the arterial wall (864 elements), where yellow regions represent collagen, and red regions represent smooth muscle.	60
5.4	The lumen radius, vessel wall radius, and the collagen radius illustrated using a Movat histology slice.	61
5.5	The circuit diagram for the 6-electrode network. The region between sets of electrodes is represented as a resistance value, R_{ij}	62
5.6	Configuration of the 6-point electrodes on the EIS sensor. Results in 15 permutations which are represented by segmented impedance heat maps.	64
5.7	The finite element 3D model. (A) 12-element mapping scheme for the initial conductivity calculations. (B) 576-element mapping scheme representing the inner smooth muscle cell. (C) 864-element mapping scheme including the collagen layer.	65
6.1	Illustrations of a stable (left) and a vulnerable plaque (right). Adapted from reference [111].	69
6.2	The normalized biological component resistance of different types of lesions with and without oxLDL. Adapted from reference [128]. . . .	71
6.3	Histology images and EIS profiles of a control aorta (left panel), an aorta with fatty streaks (middle panel) and an aorta with mild plaque (right panel). Adapted from reference [128].	72
6.4	Polyimide PCB layout for 6-point EIS. Unit: mm.	73
6.5	Sideview of the polyimide flexible PCB.	73
6.6	Detailed schematics of the cross section of the catheter assembling procedure. (A) Miniaturized holes were created using tweezers on the catheter before encapsulation with a heat shrink tube. A supporting tubing was used to increase the mechanical robustness of the catheter. (B) The balloon and the syringe connector were fixated at both ends of the catheter with epoxy glue. (C) A pair of radioopaque markers was secured using a heat shrink tube and the remainder of the catheter was encapsulated.	75

6.7	Device Schematic. (A) Schematic of the dual EIS-FFR sensor deployed in the artery. (B) Cross-sectional view of the device. (C) A photo of the dual-sensor catheter.	76
6.8	Experimental setup for the EIS measurements. The Gamry system applied voltage and recorded the impedance spectrum. A pump was used to inflate the balloon catheter.	77
6.9	The software interface showing (A) the protocol and (B) the impedance spectrum for a good pair of Pt-black plated electrodes in saline. . . .	78
6.10	A cotton swab is used to clean the surface of the electrode from the balloon end to the tip.	79
6.11	Partial ligation of the carotid artery. (A) A midline skin incision was placed at the neck and then the right common carotid artery was dissected and tied off along with a spacer, (B) . The spacer was removed to create a 50-70% stenosis, (C) 3D image of the anatomy demonstrates the presence of stenosis in the right common carotid artery and the absence of stenosis in the left common carotid artery. .	81
6.12	Carotid artery stenosis. ((A)) Baseline and (B) terminal axial CT of left (red arrow) and right (blue arrow) carotid arteries. (C) Comparison of the mean carotid artery diameters at 0 weeks (baseline), 8 weeks post-surgery (intermediate), and 16 weeks post-surgery (terminal).	82
6.13	Cross-section of the left carotid artery (control) at upstream, middle, and downstream of the vessel with (A) Movat staining for the connective tissue, (B) Picrosirius Red staining for collagen type I and III fibers, (C) E06 immunostaining for oxidized-LDL. I: tunica intima; M: tunica media; E: tunica externa.	84
6.14	Cross-section of the right carotid artery #1 (RCA1) at upstream, middle and downstream of the vessel with (A) Movat staining for the connective tissue, (B) Picrosirius Red staining for collagen type I and III fibers, (C) E06 immunostaining for oxidized-LDL. I: tunica intima; M: tunica media; E: tunica externa.	85
6.15	Cross-section of the right carotid artery #2 (RCA2) at upstream, middle and downstream of the vessel with (A) Movat staining for the connective tissue, (B) Picrosirius Red staining for collagen type I and III fibers, (C) E06 immunostaining for oxidized-LDL. I: tunica intima; M: tunica media; E: tunica externa.	86

6.16	EIS profiles from 1-300 kHz were compared between the LCA (control) and RCA1 and RCA2.	88
6.17	3D EIS-derived conductivity mappings of the LCA and two RCAs (RCA1 and RCA2). The tunica intima and tunica media were constructed from the impedance magnitude at 10 kHz.	90
6.18	Finite Element Model for the impedance modeling. (A) Representative histological cross-sections from the right carotid artery were demarcated by the Movat staining for connective tissue, the boundaries for collagen, smooth muscle, and the lipid component. (B) These demarcations from the histological slices allowed for reconstruction of a 3D model. The positions of the electrodes (red) were defined by the z and θ coordinates.	91
6.19	Electrode Position Definition. The position of the electrodes in the 3D model is defined by the polar coordinates, where z is the distance between the edge of the electrodes and $z = 0$, and θ is the angle between the midpoint of the first pair of electrodes and $\theta = 0$	92
6.20	Deviation plots for (A) LCA, (B) RCA1, (C) RCA2 position A, and (D) RCA2 position B.	94
6.21	Computational EIS resulting from four different electrode positions are compared with the experimental EIS for (A) LCA, (B) RCA1, (C) RCA2 position A, and (D) RCA2 position B.	95
6.22	EIS profiles and simulation result comparison for (A) LCA, (B) RCA1, (C) RCA2 position A, and (D) RCA2 position B.	96
7.1	Polyimide PCB layout for 12-point EIS. Unit: mm.	98
7.2	The 12-point electrode balloon catheter.	99
7.3	Schematic of the electrode arrays and the 30 permutations.	100
7.4	The EIS profiles of the ligated carotid artery (right) from 1 to 300 kHz with 30 permutations.	101
7.5	Fitness value vs dimension parameter of the vessel model including (A) lumen radius, (B) smooth muscle cell layer thickness, and (C) collagen layer thickness.	102
7.6	The reconstructed conductivity map using the impedance values measured by the 12-point EIS balloon catheter.	103

LIST OF TABLES

<i>Number</i>	<i>Page</i>
2.1 BMI (Kg/m^2), MRI PDFF (%), EIT liver conductivity (S/m) and injection current (mA) for all subjects. (*: Subject 4; electrode malfunction, Subject 14; renal failure, Subject 18; leukemia)	33
2.2 Demographics for the 19 overweight subjects including sex, BMI, age, waist circumference, height, and weight. (*: Subject 4; electrode malfunction, Subject 14; renal failure, Subject 18; leukemia.)	37
5.1 Dimensions of the artery models.	61
6.1 Tissue properties used for the computational model.[91]	93

Chapter 1

INTRODUCTION TO ELECTRICAL IMPEDANCE-BASED METHODOLOGIES

Electrical impedance analysis is a widely studied field. The approach is low cost and noninvasive, allowing one to characterize body and tissue composition, and can be used for disease diagnosis and monitoring patients vitals.[1] The electrical response of tissues can be viewed from three different perspectives. 1. The endogenous electrical responses caused by biological tissues via the ionic concentrations inside the cells. Some common examples would be the electrocardiograph (ECG) signals from the heart, and the electroencephalography signals from the brain. 2. Active responses to external electrical stimulation, such as nerve and muscle stimulation. And 3. passive responses to external electrical stimulation by a current source.[2] The ability of biological tissue to impede the current is defined as bioimpedance.[3] In this thesis, I will focus on two electrical impedance-based methodologies: electrical impedance tomography (EIT), and electrical impedance spectroscopy (EIS)-derived tomography, and their application to diseases detection.

1.1 Electrical Impedance Spectroscopy

Electrical impedance spectroscopy is a technique to characterize materials and systems by their electrical properties. This is accomplished by inducing alternating electrical signals within a range of frequencies and measuring the response.[4] I will briefly review some concepts in electrical engineering and provide references for interested readers.

Electrical Impedance

Electrical resistance (R) is the measure of a circuit element's ability to impede the flow of electrical current. This is generally approximated using Ohm's law

$$R = \frac{E}{I},$$

where E is the voltage and I is the current.

However, this simple expression will only provide accurate evaluations when considering an ideal resistor where the resistance is independent of the frequency, and the current and voltage through the resistor are in phase with each other. Real

materials exhibit more complicated behavior, thus, the impedance is introduced to describe the ability of an element to impede the flow of electrical current.

To measure the electrical impedance of a tissue, a small excitation signal is applied such that no biological changes (such as electrolyte oxidation/reduction, surface, and volume fluctuations, etc) occur. The tissue's response is therefore expected to be pseudo-linear. The resulting current responses to the sinusoidal excitation potential will likewise be a sinusoid at the same frequency, but shifted in phase. This shift can be described as:

$$\begin{aligned} V &= |V|e^{j\omega t} \\ I &= |I|e^{j(\omega t - \theta)}, \end{aligned}$$

where $\omega = 2\pi f$ is the radial frequency and θ is the phase. Then the impedance can be expressed as:

$$\begin{aligned} Z &= \frac{V}{I} = \frac{|V|e^{j\omega t}}{|I|e^{j(\omega t - \theta)}} \\ &= \frac{|V|}{|I|}e^{j\theta} = |Z|(\cos(\theta) + j \sin(\theta)), \end{aligned} \tag{1.1}$$

where $|Z|$ is the impedance magnitude. We can also view the impedance as the summation of a real component: the resistance (R) and an imaginary component: reactance (X):

$$Z = R + jX.$$

Electrical impedance spectroscopy measures the impedance over a range of frequencies. This approach contains more information when compared to traditional DC resistance measurements. There are several benefits to implementing EIS methods: label-free and real-time detection capabilities[5], ability to distinguish between two or more electrochemical reactions, identification of diffusion-limited reactions, and information on the capacitive behavior of a system.[6]

Bode and Nyquist Plots

EIS data is usually presented using a Bode Plot (frequency vs impedance magnitude and phase), and a Nyquist Plot (real part vs imaginary part).[7] A Bode plot usually presents a logarithmic scale of the frequency versus a dual y-axis (logarithm scale) of impedance magnitude and the phase shift. This plot explicitly shows the system response over a range of frequencies and allows for relative comparisons of the small and large impedances. A Nyquist plot presents the negative imaginary part of the

impedance versus the real part of the impedance. Each data point in the Nyquist plot reflects the complex impedance measured at a specific frequency, however, the frequency information is not explicit in the plot. The Nyquist plot is very sensitive to small changes and can be used to analyze the stability of the system.

Fig. 1.1 shows an example Bode plot and Nyquist plot for a simplified Randles circuit (discussed below).

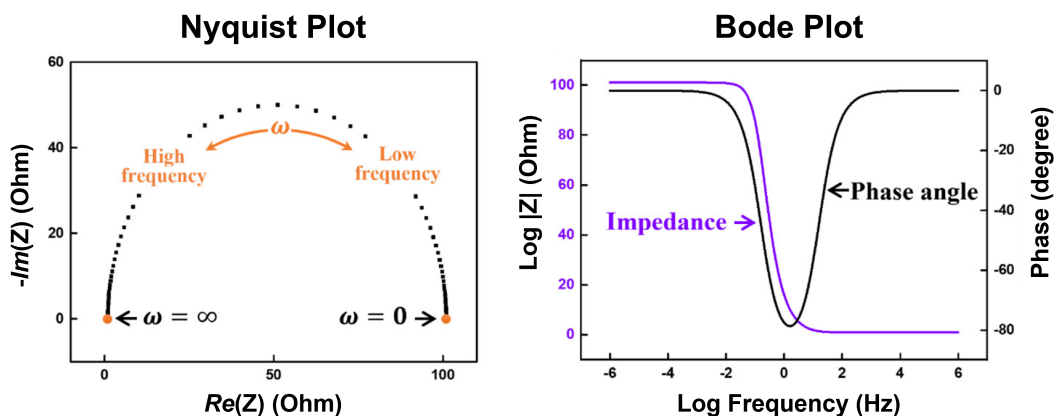


Figure 1.1: Nyquist plot (left) and Bode plot (right) for a simplified Randles circuit. Note, the Nyquist plot for a Randles cell is always a semi-circle with a diameter equal to the magnitude of the charge transfer resistance. The value of the real axis at the high frequency intercept gives the solution resistance. Adapted from reference [8]

Metal-Liquid Interface

When measuring the EIS of a tissue, an electrode pair is used to apply the sinusoidal signal and record the corresponding response. To understand the electrical response of the tissue, we want to model the entire, complex circuit using simplified elements.

Upon contact with a tissue current will spontaneously flow from the surface of the electrode to the electrolyte. This results in a “double layer” at the electrode-electrolyte interface.[9] Due to the absorption of ions from the electrolyte onto the electrode surface, two layers of charges with opposite polarity form as shown in Fig. 1.2. This double layer structure can be thought of as a capacitor with one layer of electrons on the electrode and one layer of ions in the electrolyte, separated by an electrolyte solvent (dielectric layer).

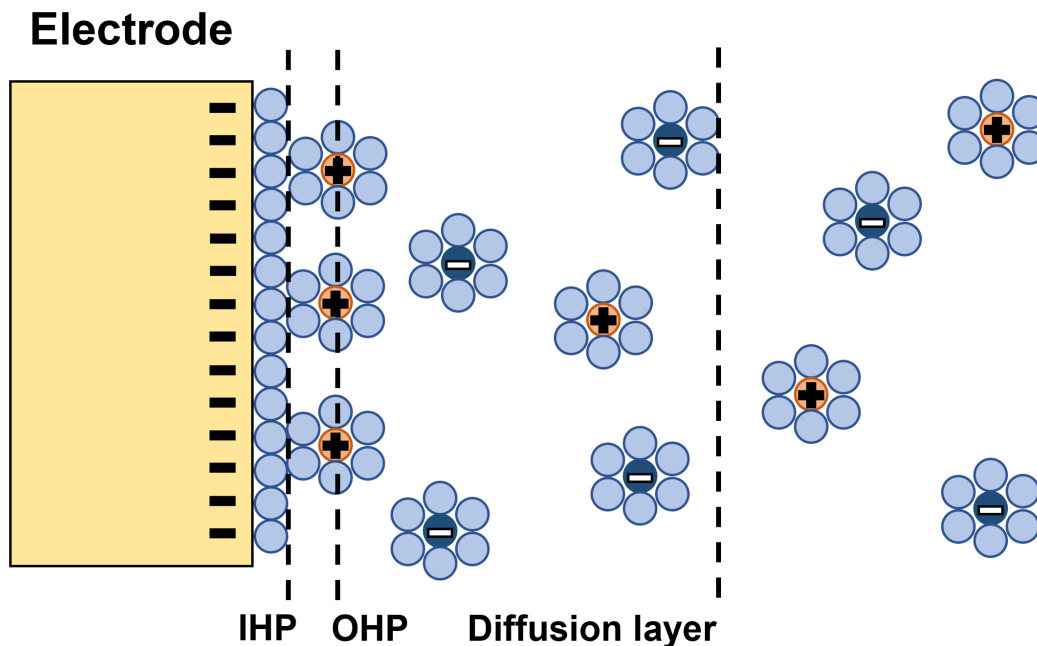


Figure 1.2: Simplified illustration of the double layer at the electrode-electrolyte interface. The positively charged oxidants diffuse toward the electrode with negative charge and become the reductants after accepting the electrons from the electrode at the interface. IHP and OHP define the inner and outer Helmholtz planes, respectively.[9] Adapted from reference [10].

Another factor that we must consider in our circuit is the resistance of the electrolyte between the pair of electrodes. The electrolyte resistance depends on the type of electrolyte, the concentration, the temperature, and the geometry of the electrodes.

In a typical electrochemical cell, charge transfer resistance needs to be considered too. When the oxidation-reduction reactions occur at the surface of the electrodes, corresponding charge transfers between the metal surface of the electrode and electrolyte occur. The speed of the transfer reaction is dependent on the potential, the temperature, and the concentration of the products. The diffusion of the reaction reagents induces a fixed-phase impedance known as the Warburg impedance, which increases as the frequency of the potential perturbation decreases.[11]

By combining the circuit elements described above, we make a “Randles Circuit” proposed by John Edward Brough Randles. These circuits are used to model interfacial electrochemical reactions in the presence of a semi-infinite linear diffusion of ions to the electrodes.[12] The circuit, as shown in Fig. 1.3, is the series combination of the electrolyte resistance R_e and the double layer capacitance C_{dl} . If

redox reactions occur, the charge transfer resistance R_{ct} in series with the Warburg impedance Z_w is in parallel with C_{dl} . When measuring the impedance of tissues with small voltage and current, the R_{ct} and Z_w can safely be neglected.

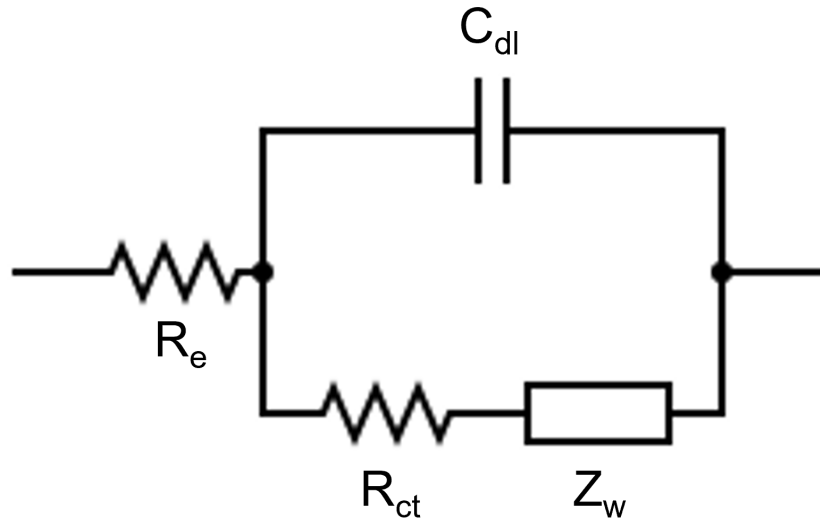


Figure 1.3: The associated circuit for the Randles Cell, where R_e , C_{dl} , R_{ct} , and Z_w are electrolyte resistance, double layer capacitance, charge transfer resistance, and Warburg impedance, respectively.

Simplified Circuit for Tissues

Next, we want to understand the electrical behavior of tissues. One can think of a tissue as a set of similarly structured cells that function together. A cell can be modeled as three components: the intracellular fluid (the cytoplasm), the cell membrane, and the extracellular fluid. Both the intracellular fluids and extracellular fluids are complex mixtures of substances and ions dissolved in water. They can both be treated as conductive mediums with a given resistivity ρ . We denote the intracellular fluid resistance as R_{ICF} and the extracellular fluid resistance as R_{ECF} . [13]–[15]. The cell membrane consists of a semi-permeable lipid bilayer with embedded membrane proteins. The main components of the membrane are lipids, therefore the cell membrane is relatively insulating. Due to its bilayer structure, the cell membrane can be modeled as a “leaky” capacitor; a capacitor C_{CM} in series with a resistor R_{CM} . [16] This simplified circuit model is illustrated in Fig. 1.4.

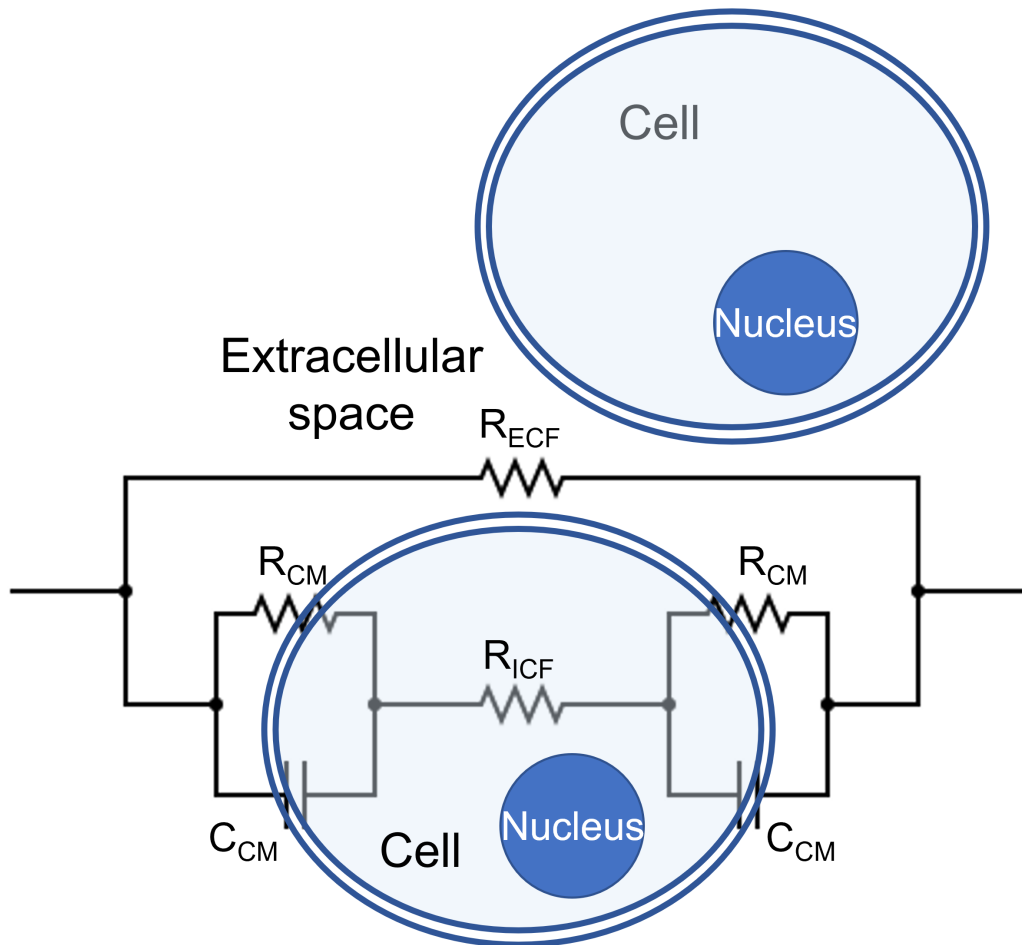


Figure 1.4: Illustration of the simplified equivalent electrical circuit model for tissue. Note the resistance from the intracellular fluid and extracellular fluid and the capacitance from the cell membrane. Adapted from reference [17].

When electrical current is applied on a tissue with tightly packed cells held together by “tight junctions”, the current must pass through the cell membranes and the intracellular fluid. At some locations, there are “gap junctions” that provide inter-cellular space for ions and current to flow through. An electrical circuit model for these tissues would be a series combination of R_{ICF} and C_{CM} representing the tight junction path in parallel with R_{ECF} for the gap junction path.

When doing EIS measurements, we apply current/voltage over a range of frequencies. Among the electrical components we mentioned above, the capacitor has frequency-dependent properties. The impedance of a capacitor decreases as the frequency increases ($Z_c = \frac{1}{j\omega C}$). [18] Therefore, at low frequencies the impedance from the cell membrane capacitor C_{CM} is high and the electrical signal tends to

flow through the extracellular space. On the other hand, at high frequencies the impedance of the cell membrane capacitor C_{CM} is low, allowing the electrical signal to pass through the cells (Fig. 1.5). The impedance spectrum for a biological tissue is shown in Fig. 1.6. The corners of the impedance spectrum are determined by the double layer impedance and the tissue impedance. The first corner is related to the double layer of the metal-liquid junction with a 20 dB/decade decrease in impedance. The flat band between the first (usually around 1 kHz) and second corner is correlated with the extracellular space of the tissue (R_{ECF}). The second corner is dominated by the cell membrane, and intracellular properties, and usually is around 1 MHz but can vary depending on the cell types. After the second corner, the flat band reflects the impedance of R_{ECF} in parallel with R_{ICF} .

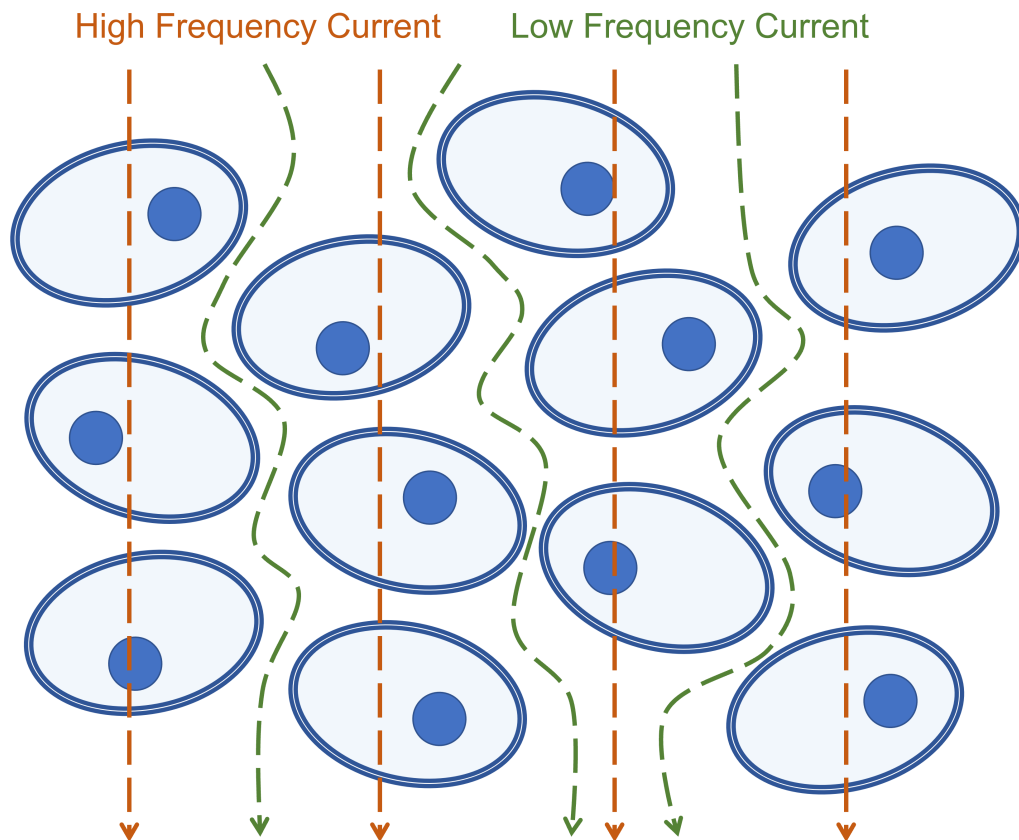


Figure 1.5: Cartoon depiction of the electrical current at different frequencies and how it flows through the tissue. Adapted from reference [19].

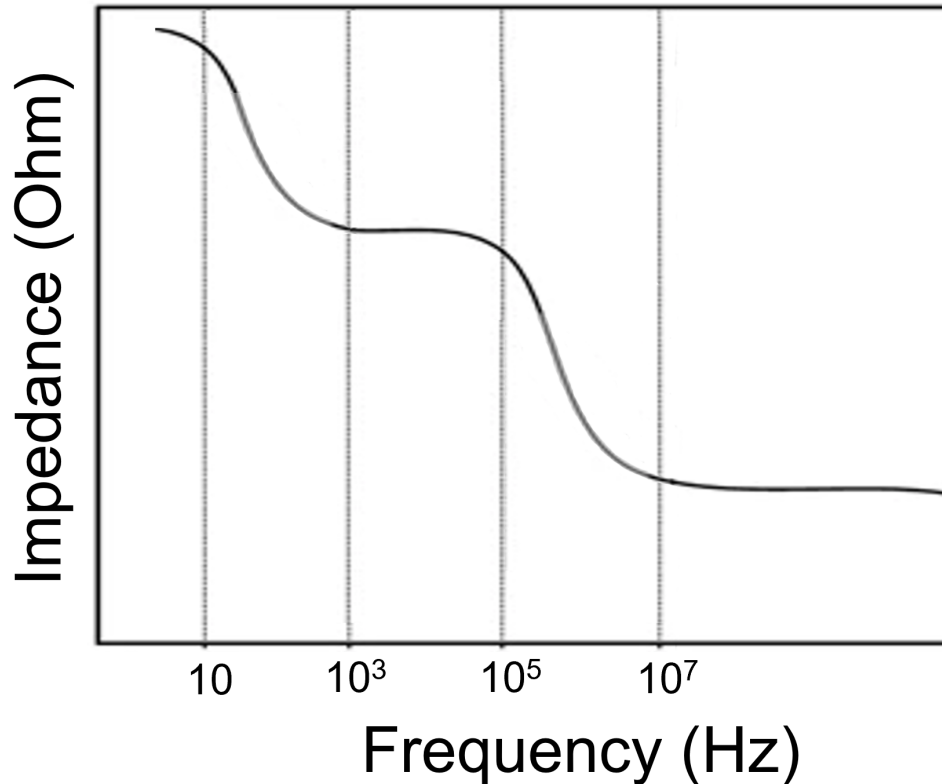


Figure 1.6: An example impedance Bode plot for biological tissue. Adapted from reference [20].

1.2 Electrical Impedance Tomography

Electrical impedance tomography (EIT), a subset of EIS techniques, utilizes voltage data measured at the boundary of the domain of interest to reconstruct the electrical conductivity distribution in 3D space. This results in a noninvasive medical imaging procedure with many applications; for example lung ventilation monitoring [21], [22], breast cancer detection, and brain imaging. Typically small AC current is applied to surface electrodes attached directly on the patients skin. The resulting voltage data is recorded using a separate set of electrodes. From this data, an image reconstruction algorithms can construct a conductivity tomogram.

Types of EIT

Tissues such as muscle and blood with a high fluid content have higher conductivity when compared to fat and bone.[23] Absolute EIT aims to reconstruct cross section images using this property.[24] Formally speaking, the problem of reconstructing the conductivity from the surface electrical measurements is an ill-posed, non-linear inverse problem. Extensive mathematical research has been developed regarding the

uniqueness of solution and associated numerical algorithms to address this family of problems.[25] Another complication for absolute EIT is the electrical currents trajectory. The current passes through the tissue following the lowest resistance path, resulting in a loss of current through the transverse plane.

For some applications, we care about the difference between two or more physiological states such as the inspiration and expiration of the lungs. For these problems, time-difference EIT has major advantages when compared to absolute EIT. Namely the elimination of error associated with absolute EIT approaches because time-difference EIT simply subtracts the reconstructed images at different points in time.[26]

Another common EIT method is the so-called frequency-different EIT, which utilizes electrical measurements at multiple frequencies. These approaches have been shown to detect localized abnormal tissue within normal tissue. It has even been suggested they may resolve the technical difficulties resulting from unknown boundary geometry and uncertainty in the electrode positions.[27] Because tissues have different frequency responses due to their unique electrical properties, cleverly selecting specific frequencies could potentially distinguish different tissues.[28]

Theoretical Framework for EIT Reconstruction

In this subsection, I will discuss the EIT imaging reconstruction algorithm used in this work which is based on previous publications, i.e. see references [28], [29]. Following the injection of a known current to the abdomen, an EIT conductivity map across the abdomen is reconstructed with a set of voltages recorded by an electrode array placed on the surface of the upper abdomen (Fig. 1.7). With *a priori* knowledge of the target (the liver in this example), the geometric boundary conditions are established, being careful to establish a high degree of precision to mitigate the instability due to the ill-posed inverse problem.[30] The solution is then obtained by using a regularized Gauss-Newton (GN) type solver. This process is depicted in Fig. 1.8.

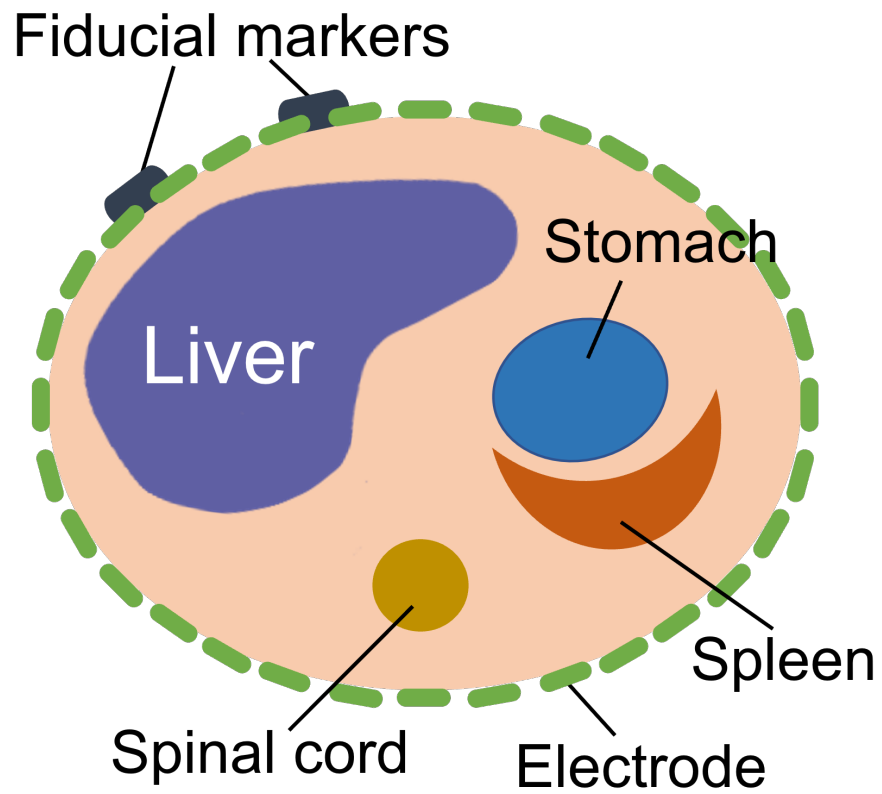


Figure 1.7: Schematic of electrodes positions and MRI markers on the abdomen surface with respect to liver and other organs positions.

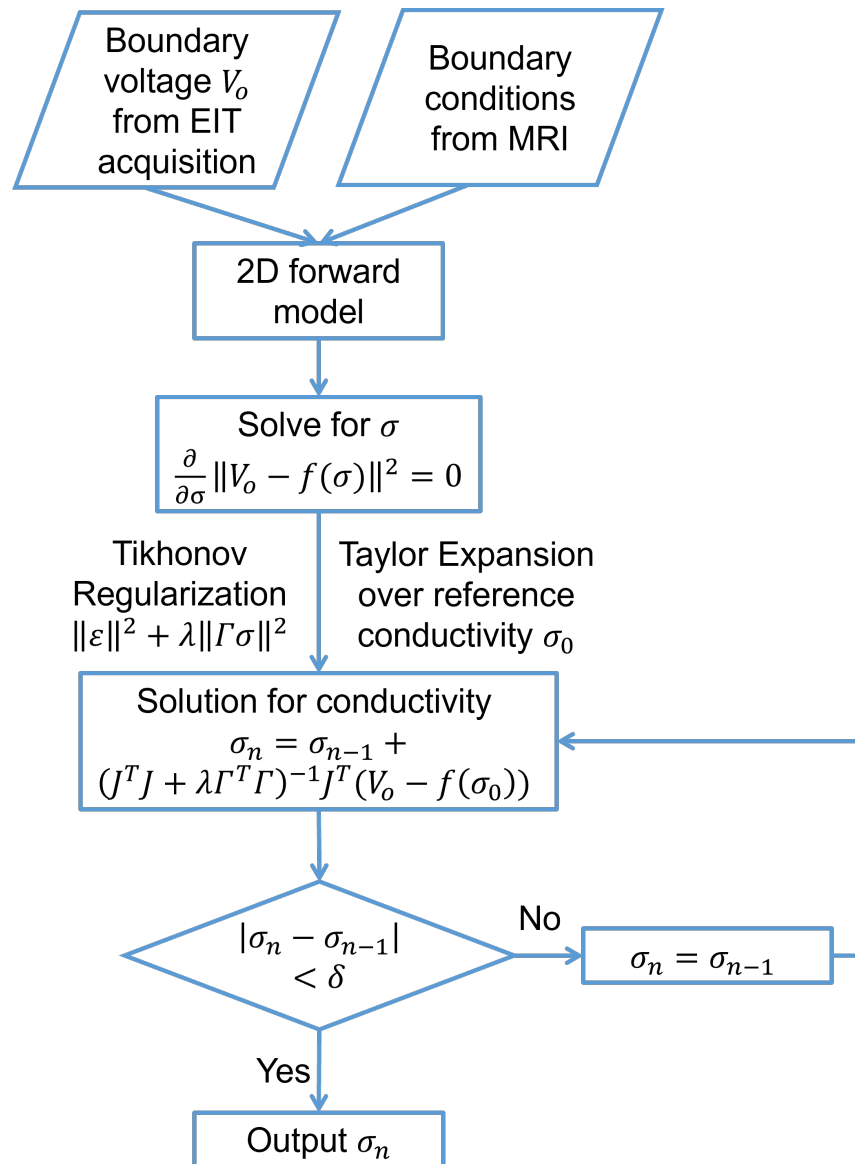


Figure 1.8: Schematic flowchart of the EIT reconstruction. A regularized Gauss-Newton solver is applied for solving the inverse problem.

The Gauss-Newton solver calculates the conductivity by minimizing ϕ , the L2 norm (the square root of the sum of the squares) of the difference between the measured voltage V_o , and a function of the conductivity $f(\sigma)$:

$$\phi = \|V_o - f(\sigma)\| \quad (1.2)$$

where $f(\sigma)$ is considered to be the “forward problem” derived from the Laplace equations:

$$\nabla \cdot (-\sigma \nabla V) = 0. \quad (1.3)$$

By taking the first-order Taylor series expansion of ϕ :

$$\phi = \|V_o - f(\sigma)\| \simeq \|(V_o - f(\sigma_0)) - J(\sigma - \sigma_0)\| \quad (1.4)$$

where σ_0 is a reference conductivity value, and J is the Jacobian matrix of our inverse problem, and setting $\frac{\partial \phi}{\partial \sigma} = 0$, one can minimize ϕ and obtained σ :

$$\sigma = \sigma_0 + (J^T J)^{-1} J^T (V_o - f(\sigma_0)). \quad (1.5)$$

Eq. 1.5 represents the ill-posed inverse problem one is required to solve when implementing the EIT reconstruction. The subsequent solution, σ , is highly sensitive to perturbations in the voltage. A general method to mitigate the instability issue is to introduce a constraint term that guides the trial solution towards a preferred solution,

$$\phi^2 = \|\varepsilon\|^2 + \lambda \|\Gamma \sigma\|^2. \quad (1.6)$$

The constraint term, $\lambda \|\Gamma \sigma\|^2$, is incorporated into the objective function directly, an approach commonly referred to as Tikhonov Regularization. The coefficient, λ , is known as the regularization parameter, and aims to suppress the conductivity spikes in the solution space.

With *a priori* conductivity of a similar area, the term, Γ , acts as a “weighted” Laplacian operator that enables one to adjust the conductivity properties and suppress non-smooth regions. The approach is utilized heavily in Chapter 2, and in general the strategy is useful for medical imaging, where *a priori* anatomic information of individual organs can be obtained from an MRI multi-echo sequence and subsequently integrated with the EIT solutions. By applying the regulation term to Eq. 1.3, the following solution is found:

$$\sigma_1 = \sigma_0 + (J^T J + \lambda \Gamma^T \Gamma)^{-1} J^T (V - f(\sigma_0)). \quad (1.7)$$

To obtain the absolute conductivity mapping, an iterated approach was used. First, by assuming an arbitrary conductivity, σ_0 , one can calculate J , Γ , and $f(\sigma_0)$. Then from Eq. 1.7 a new conductivity value set, σ_1 , is computed and a new set of J , Γ and $f(\sigma_1)$ are generated. This iterative procedure can then be continued until a desired convergence is achieved, for example the difference between σ_n and $\sigma_{(n-1)}$ being converged within a predefined threshold.

To implement the reconstruction algorithm described above, the online open source library Electrical Impedance Tomography and Diffuse Optical Tomography Reconstruction Software (EIDORS) [31] was used. The library is capable of constructing

finite element models with accurate dimensions for geometries, and proper meshing with through the mesh generator (Netgen).[32] Rather than using a presumed geometry for the finite element model, we combined the MRI multi-echo images topology with the multi-electrode-measured voltage data to reconstruct the liver EIT conductivity map. As a result, the computational errors from the variations in the geometry of the abdomen of different subjects were greatly reduced.

EIT Medical Application

One well studied application of EIT in the medical field is the monitoring of lung activity. By collecting impedance data and reconstructing an image, EIT allows for continuous and functional respiratory monitoring. This monitoring can be done at the patients bed-side, and avoids the need for radiation while generating image data.[33] The information obtained from EIT can be used to visualizes local ventilation and arguably the lung perfusion distribution. While the soft tissues in the thorax allow the passage of current with little resistance, the lung containing air can have a resistivity that is up to five times larger. In addition, there is a two-fold difference in lung resistivity between inspiration and expiration.[22] This property makes lung monitoring the current most promising clinical application for EIT.

Typically, an electrode belt with 16 or 32 electrodes is placed around the thorax in the 5th to 6th intercostal spaces at the parasternal line for lower lobes of the left and right lungs and the heart.[34] This placement is important as it avoids having the diaphragm enter the measurement plane. An alternating current with low intensity (5-10 mA) and a high frequency (50-80 kHz) is applied to the electrodes and the resulting surface voltages are recorded by the remaining pairs of electrodes (Fig. 1.9). With the 16-electrode setup, the spatial resolution is 12% of the thoracic diameter in the peripheral region and 20% in the central region. The resolution can be improved by up to 10% by doubling the number of electrodes.[26] While the spatial resolution is less compared to a CT, EIT has the advantage in temporal resolution, which can offer a maximum scan rate of 50 frames per second. This is ideal for monitoring the activity of the lungs under dynamic conditions. The reconstruction is typically done through a time difference EIT (td-EIT), where the relative impedance changes of the lungs ventilation over time is resolved.[35]

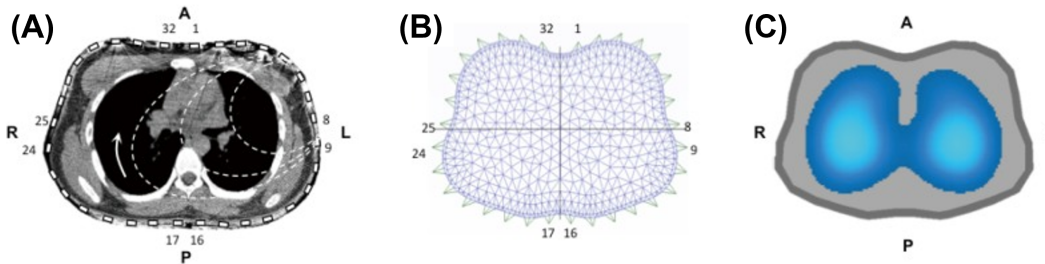


Figure 1.9: Illustration showing (A) electrodes distribution with respect to the thorax, (B) the reconstruction mesh, and (C) image obtained during ventilation. Adapted from reference [22].

An important topic for clinical application is the assessment of the alveolar recruitment. This is typically studied with a pressure-volume (P-V) curve. While the P-V curve may provide global characteristics, it is lacking in regional information. EIT methods could potentially assess the dependent silent spaces (DSSs), which are the poorly ventilated regions in the lungs, thus providing a dynamic bed-side measurement for recruitment. In Fig. 1.10, different levels of positive end-expiratory pressure (PEEP) were applied to intubated patients, and impedance maps were reconstructed using EIT. Regions with less than 10% impedance changes were determined to be silent spaces. The variation of DSSs dynamically measured by EIT correlates well with lung recruitment measured using P-V curves.[21]

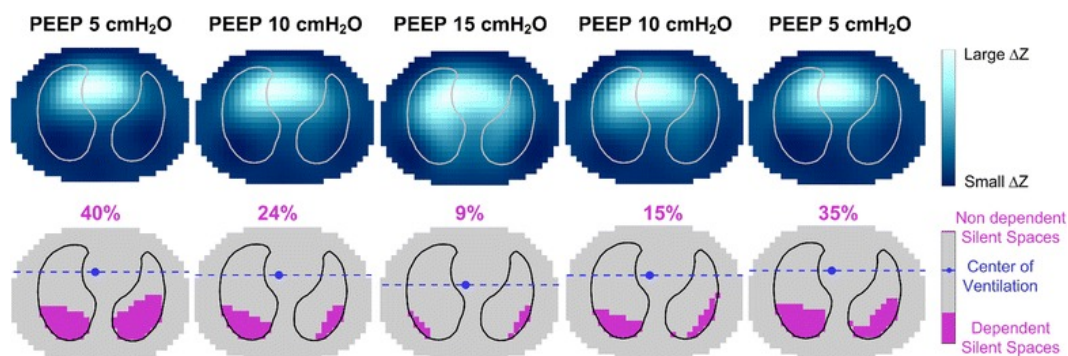


Figure 1.10: Impedance maps from EIT and “silent spaces” values at different levels of positive end-expiratory pressure. Adapted from reference [21].

1.3 Summary

In this chapter, we covered the essential fundamentals needed to understand electrical impedance of tissues, and two methodologies based on impedance: EIS and EIT. They are both noninvasive methods that are capable of differentiating tissues due

to their distinct electrical properties. While the EIS approach provides impedance values of the tissue with relatively simple electrode setups, EIT has the advantage of visualizing the conductivity distribution by solving the ill-posed inverse problem with a more complicated electrode array. In Chapters 2 and 3, we will present an application using traditional EIT to quantify the fat content in the human liver. Then in Chapter 4, we discuss an application using “outward” EIT for plaque detection. In Chapter 5, we propose a new method to create a similar conductivity distribution map by forward simulation of the conductivity based on measured impedance via EIS. Finally, applications of this new method are explored via detecting plaque in pig carotid arteries in Chapters 6 and 7. Future work stemming from these projects is then outlined in Chapter 8.

Chapter 2

EIT FOR FATTY LIVER DETECTION

This chapter discusses the application of electrical impedance tomography to detect fatty liver. Nineteen subjects diagnosed to be either overweight or obese were examined using a liver MRI scan and EIT measurements. With the *a priori* knowledge of the liver boundary from the MRI, we were able to apply an EIT algorithm to reconstruct the conductivity distribution. The proton-density fat fraction (PDFF%) obtained from the multi-echo MRI was then used to compare fat content with the EIT liver conductivity. A Pearson's correlation analysis between the EIT conductivity and the MRI PDFF was performed, accounting for demographics data of the subjects including body mass index (BMI), age, waist circumference, height, and weight. The correlation between liver EIT conductivity and MRI PDFF with demographics was shown to be statistically insignificant, whereas the liver EIT conductivity was demonstrated to inversely correlate with MRI PDFF ($R = -0.69$, $p = 0.003$, $n = 16$). This pilot study suggests that EIT conductivity can act as a portable method for operator-independent and cost-effective detection of hepatic steatosis.

2.1 Fatty Liver

Nonalcoholic fatty liver disease (NAFLD) refers to a wide spectrum of liver conditions. These can range from simple steatosis to steatohepatitis, advanced fibrosis, and cirrhosis due to the abnormal accumulation in liver cells which affects people who drink little to no alcohol.[36] During simple steatosis, the large build-up of macrovesicular fat in the liver cells usually does not result in symptoms, and can be reversed with weight loss and medical support.[37] However, simple steatosis or non-alcoholic fatty liver (NAFL) can progress to non-alcoholic steatohepatitis (NASH, hepatic inflammation), which can be characterized by steatosis with lobular inflammation and cellular ballooning.[38] NASH can even lead to more severe complications such as fibrosis (liver scarring due to persistent inflammation), cirrhosis (permanent damage that can lead to requiring a liver transplant), liver cancer, liver failure, or cardiovascular diseases.[39] The progression of NAFLD is shown in Fig. 2.1.

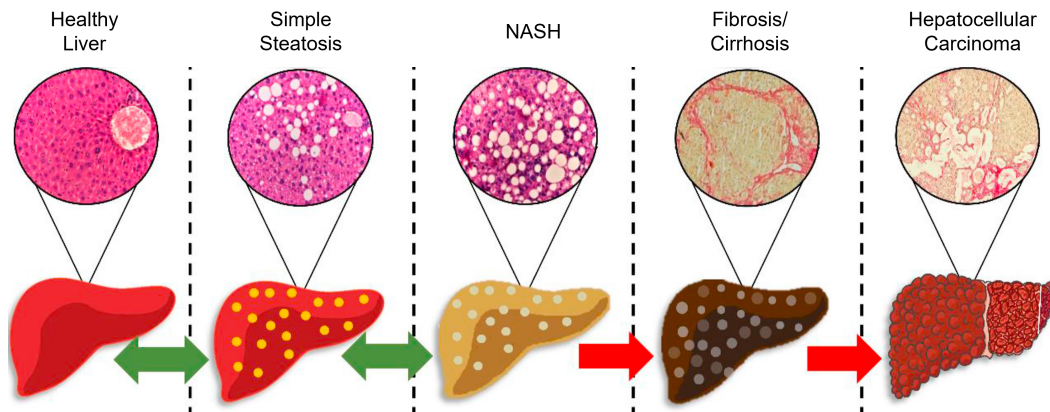


Figure 2.1: Schematic diagram and liver biopsy images of different stages in NAFLD progression including simple steatosis, NASH, fibrosis/cirrhosis, and hepatocellular carcinoma. Adapted from reference [40].

Obesity and type 2 diabetes are strong risk factors associated with the development of NAFLD.[41] In the United States more than a third of the adults are categorized as obese, and severe obesity (BMI > 35 kg/m²) is continuing to rise nationwide.[42] NAFLD is now one of the most common causes of cirrhosis in the developed world and can require a liver transplantation to be treated.[43], [44] A clinical challenge for the management of NAFLD is the non-invasive detection of fatty liver (i.e., simple hepatic steatosis) at an early stage when intervention is possible and its progression can be monitored.[45], [46]

Diagnostic Methods

The gold standard for diagnosing NAFLD is a liver biopsy (tissue examination). It allows physicians to diagnose and distinguish NAFLD from other liver diseases and can evaluate the severity of the inflammation and fibrosis.[47] However, as an invasive diagnosis method, it carries substantial risk. It is also very likely a patient may just be asymptomatic, therefore patients tend to refuse the biopsy. There are other disadvantages to this approach, namely sampling bias and inter-observer variability.[48]

Other noninvasive methods such as blood tests, ultrasonography, or liver MRI have their own issues regarding the diagnosis of NAFLD. Routine blood tests include liver functional tests and liver enzyme tests, but they are not sensitive enough to detect NAFLD.[49] However, they are used to distinguish the fatty liver associated with inflammatory injury from viral hepatitis.[50] Moreover, studies have shown

that there are some circulating serum biomarkers that are related to liver fibrosis and can be used to estimate the progression of liver fibrosis and cirrhosis.[51], [52] Non-invasive image methods such as ultrasonography and liver MRI have been used to diagnose stenosis [53] and NAFLD screening. Liver MRI proton-density fat fraction (PDFF) is the current non-invasive reference standard for validating liver fat infiltrate.[54], [55] These imaging modalities are known to be cost-prohibitive for underserved communities and require access to a scanner. Moreover, they have not been accepted as a replacement for a liver biopsy in clinical trials.[41] Ultrasound elastography, a medical imaging modality that maps the elastic properties and stiffness of soft tissue, is also non-invasive, however, it is operator-dependent and resolution is limited.[56], [57] A cost-effective and portable non-invasive method for early and operator-independent detection of fatty liver disease remains an unmet clinical need.

2.2 Previous EIT Studies for Fatty Liver Detection

Electrical impedance tomography has been used in the clinical setting for over two decades. Diagnostic EIT was developed for pulmonary function and lung capacity.[58] For instance, transthoracic impedance pneumography has been demonstrated to assess lung capacity [59], [60], and EIT has been used to measure myocardial motion and blood volume for cardiac output (CO) [61]–[63]. EIT can also assess the conductivity of breast and brain tissues.[64] By virtue of tissue-specific electrical conductivity, fatty infiltrate in the liver is characterized by its frequency-dependent electrical impedance (Z) in response to an applied alternating current (AC). At low frequencies, the lipid-bilayers impedes the current flow, resulting in high conductivity. At high frequencies the bilayer is analogous to an imperfect capacitor, resulting in tissue and fluid-dependent impedance. This impedimetric property is the basis for applying a multi-electrode array to measure tissue-specific conductivity, morphology, and volume.[65]–[68]

Due to the varying free ion content, muscle and blood are more conductive than fat, bone, or lung tissue.[65], [69]. Fat-free tissue such as skeletal muscle has a high water content ($\sim 73\%$) and a high ion and protein content allowing for efficient electrical conductivity. Fat-infiltrated tissues such as fatty liver are anhydrous (steatosis), resulting in a reduction in the conductivity. This impedimetric property is the basis for applying liver EIT to the identification of fatty liver infiltrate.[29]

Previously, [29], an EIT reconstruction algorithm was established and validated with benchtop tests. An *ex vivo* porcine liver in a non-conductive tank with 32 circumferentially-embedded electrodes demonstrated high-resolution reconstruction images given *a priori* information on the location and geometry. EIT measurements were also performed on New Zealand White rabbits with a high-fat diet, resulting in significantly distinct liver conductivity values compared to the control population. Histopathological results also showed the existence of hepatic fat accumulation in the rabbits with the high-fat diet protocol. The EIT measurements were then conducted on human subjects and the liver fat content was quantified by the MRI fat volume fraction (FVF). The results showed that a lower body-mass index subject, the average liver conductivity was higher while the FVF was lower. This study, however, only reported two human subjects. To better verify the feasibility of EIT's application on fatty liver quantification, a pilot study with 19 overweight or obese subjects was conducted. Fig. 2.2 provides the overall workflow of the study.

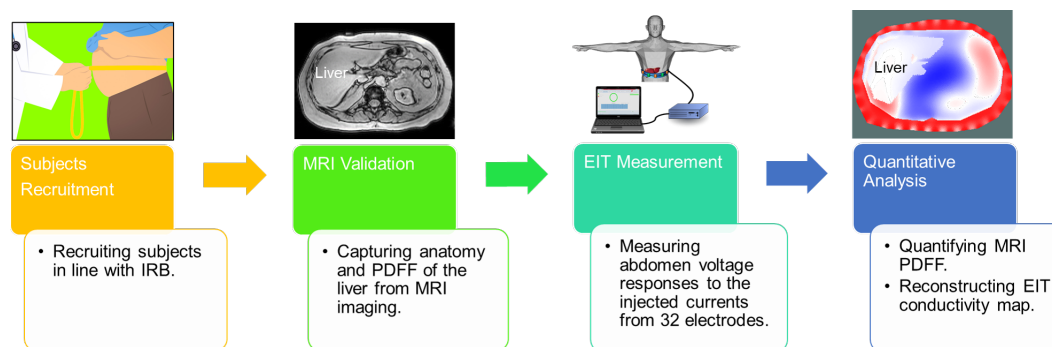


Figure 2.2: Schematic workflow of the comparison and validation of the MRI and EIT studies. Volunteers were recruited according to the UCLA Institutional Human Subjects Protection Committee. Multi-echo MRI scans were performed to provide the liver anatomy and proton density fat fraction, and were followed by EIT measurements. Finally, EIT conductivity maps were reconstructed and the MRI PDFF was used to quantify fatty liver infiltrate, and to compare with EIT liver conductivity. Adapted from reference [28].

2.3 Human Study Recruitment

The recruitment of human subjects was conducted at the UCLA Center for Human Nutrition in compliance with the UCLA Human Subjects Protection Committee. The study protocol (#15-001756) was approved by the UCLA Internal Review Board. All subjects provided a written informed consent form before participating

in the research procedures. All experiments were performed in accordance with relevant name guidelines and regulations.

A total of 19 volunteers were enrolled comprised of 15 females and 4 males. Their ages ranged from 27 to 74 years old, and the waist circumference spanned 91cm to 141.5cm. The body mass index, defined as body mass divided by the square of the body height, ranged from 25.5 to 46.8Kg/m².

The subjects' inclusion criteria outlined the following: the ability to travel for phlebotomy (whole blood collection), no prescription or over-the-counter medications for weight loss, absence of alcohol consumption, no weight change > 5 pounds in the previous 3 months, and to be clinically overweight with a BMI > 25, and waist circumference > 40" for men or > 35" for women.

The exclusion criteria included coronary artery disease on medications, claustrophobia, previous liver cancer, liver surgery, alcoholism (DSM-5 criteria: alcohol abuse or dependence), metallic implants or other factors hazardous to the MRI scanner as per the MRI safety guidelines, and body weight > 300 pounds (weight and size restrictions for undergoing MRI) (Fig. 2.3). Note that an MRI scan was performed to establish the PDFF for quantifying fatty infiltrates in the liver. The clinical demographic and physical characteristics were collected in terms of sex, BMI (Kg/m²), age (years), waist circumference (cm), height (cm), and weight (kg) (see Table. 2.2).

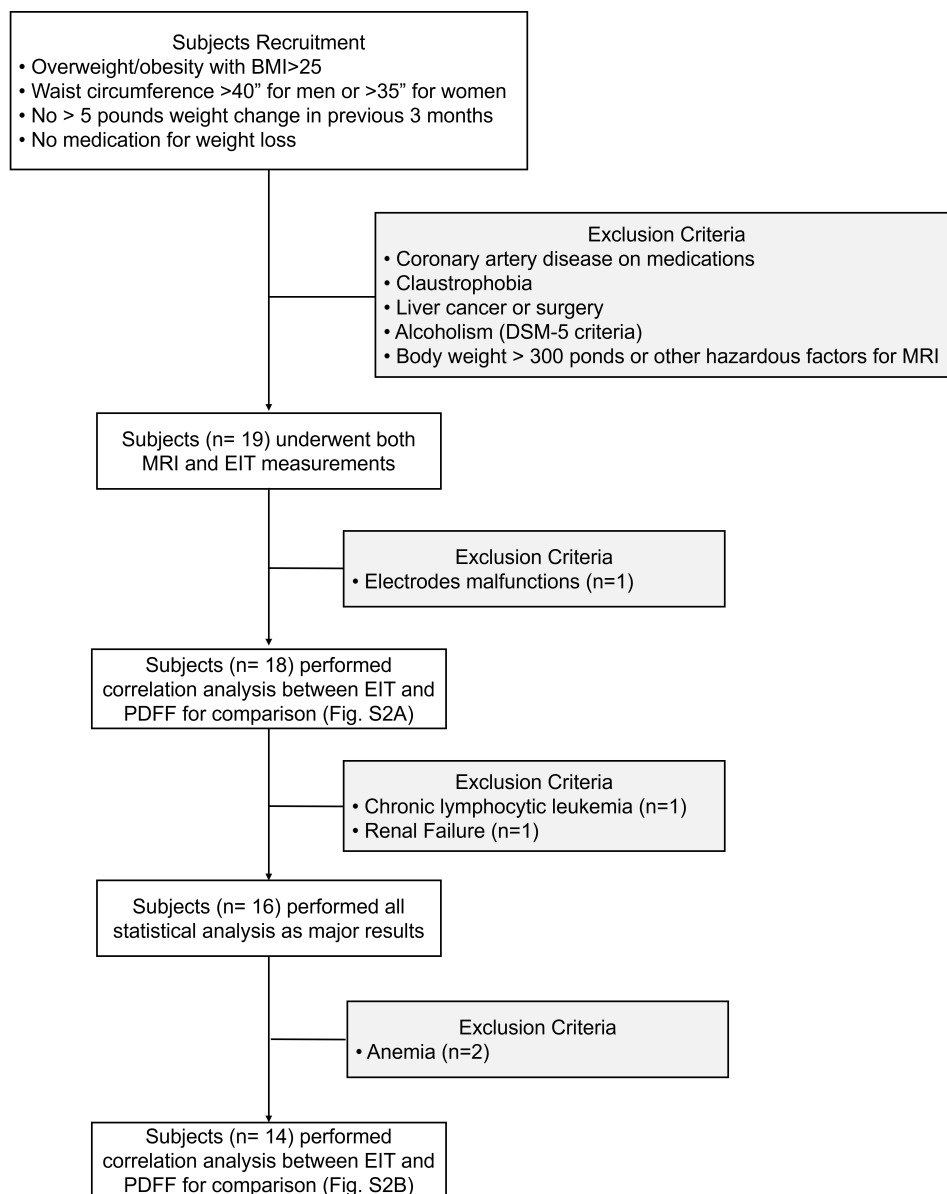


Figure 2.3: Human subject recruitment flow chart.

2.4 MRI Scan and PDFF

Following enrollment and consent, the subjects underwent a 30-minute liver MRI scan, including multi-echo imaging for mapping the proton density fat fraction. Non-contrast-enhanced abdominal MRI scans were performed on a 3-Tesla system (Skyra, Prisma, Siemens, Erlangen, Germany) using a body array and spine array coils. The protocol included breath-held anatomical scouts, a breath-held T2-weighted 2D multi-slice half-Fourier single-shot turbo spin-echo (HASTE) sequence, and a breath-held 3D multi-echo gradient-echo sequence (TE = 1.23, 2.46, 3.69, 4.92, 6.15,

7.38 ms; TR = 8.94 ms, flip angle = 4 deg, typical field of view = $400 \times 350 \times 256 \text{mm}^3$, typical matrix size = $192 \times 168 \times 64$, parallel imaging factor = 4, typical scan time = 19 sec) to quantify the PDFF. The scanner software (LiverLab, Siemens, Erlangen, Germany) utilized a multi-peak fat spectral model with a single $R2^*$ for multi-step signal fitting.[70] The MRI images and PDFF maps were saved in the DICOM format and downloaded from the scanner for analysis.

To ensure alignment of the EIT slice position and the corresponding mid-liver MRI slice, 2-3 MRI-visible fiducial markers (MR-SPOT 122, Beekley Medical, Bristol, CT) were affixed to the patient's skin above the expected mid-liver region prior to the MRI scan (Fig. 1.7). The positioning of the fiducial markers was then examined on the anatomical scouts. If needed, the MRI technologist would re-position the fiducial markers on the subject's abdomen and re-acquire the scouts. At least one adjustment would be required, and the entire alignment took less than 3 minutes.

The echo 1 (TE = 1.23) magnitude images from the 3D multi-echo gradient-echo sequence were used for contouring the body and the liver, to create a 3D anatomy model. An axial slice in the MRI PDFF maps containing MRI-visible fiducial markers was selected for analysis. Five circular regions of interest (ROIs) with an area of 5mm^2 were delineated in the slice with fiducial markers by a trained researcher to avoid blood vessels, bile ducts, and imaging artifacts. These slices were at least 1-2cm away from the liver capsule (Fig. 2.4). The mean PDFF from the ROIs (0-100%) was reported for each subject (see Table. 2.1).

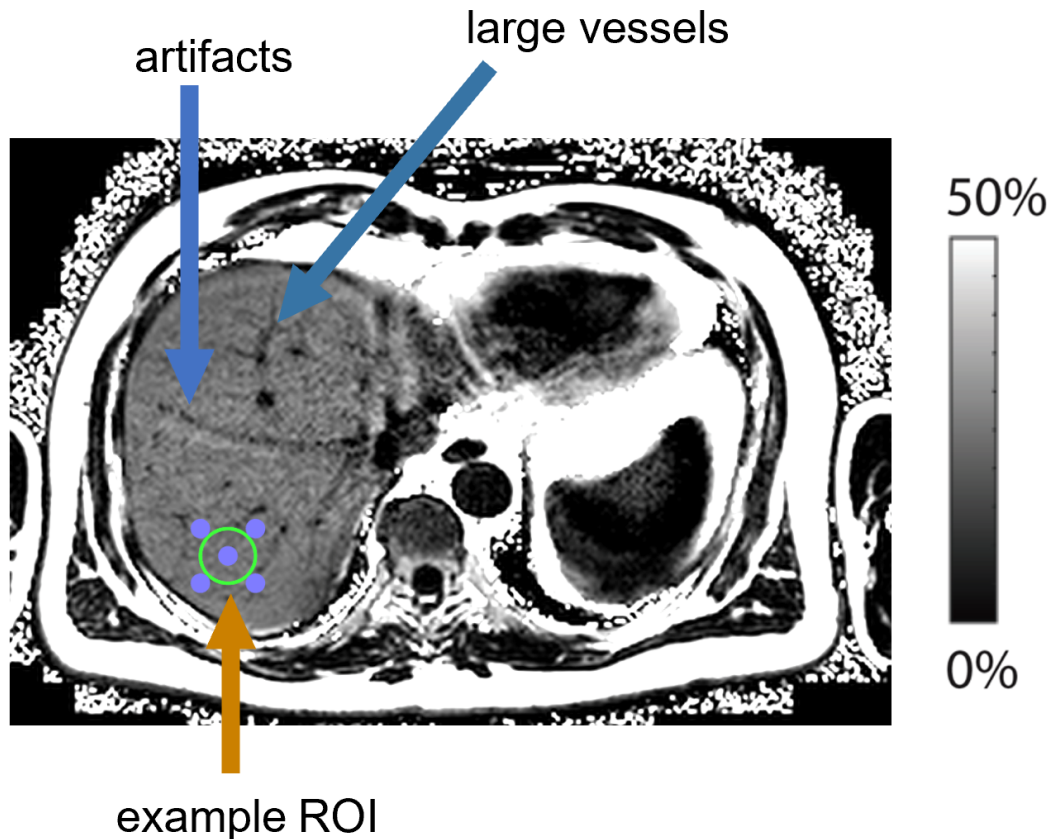


Figure 2.4: Example ROI on one slice of the PDFF image, avoiding blood vessels and imaging artifacts.

2.5 EIT Experiments

EIT Equipment Setup

EIT measurements were performed with 32 electrodes attached to the upper abdominal region. All of the electrical measurements and data acquisition for liver EIT imaging were conducted using the SenTec EIT Pioneer set (SenTec AG, Switzerland), which was composed of an interface module, sync connector, and a sensor belt. The interface module provides up to 4kV galvanic isolation of sync connector, manages the power supply for the sync connector and electrodes, and synchronizes the input and output signal. The sync connector is able to provide a programmable injection current with a peak ranging from 1-7mA and a frequency range of 50-250kHz. It can also achieve high resolution and high speed data acquisition (1-80 data frames per second). The sensor belt has 32 data acquisition channels which can be connected to disposable surface electrocardiogram electrodes (Covidien, Ireland) using alligator clips (Fig. 2.5).

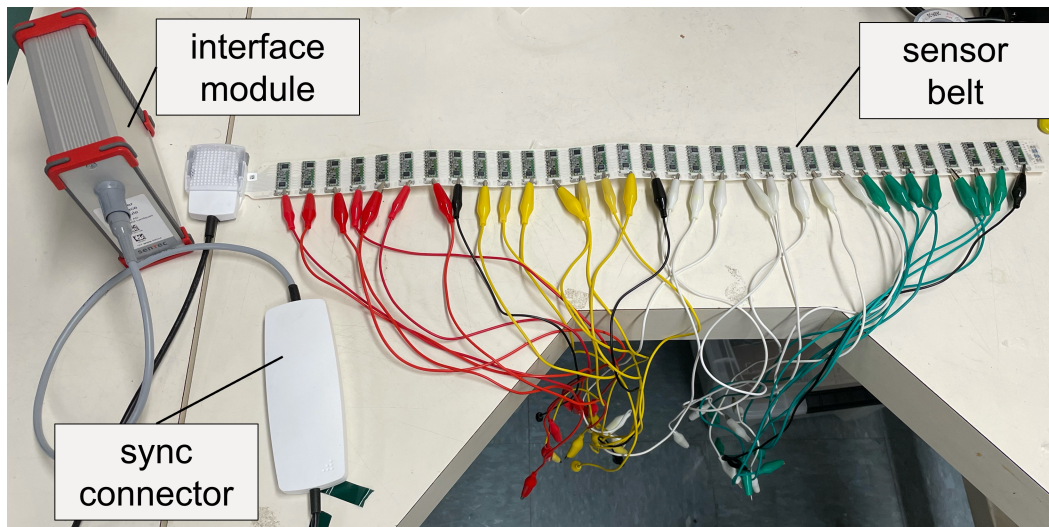


Figure 2.5: Photo of the SenTec EIT Pioneer set used for EIT measurements.

Measurement Protocol

Following the MRI scans, subjects underwent the EIT measurements. The MRI-visible fiducial markers on the abdomen facilitated the circumferential positioning of the EIT electrodes. The 32 ECG electrodes were attached to the subjects skin around the upper abdomen. To make sure there was an even distribution of the 32 electrodes, the bisection method was used. Two electrodes were attached in the middle of the front abdomen and then the back, then 1 electrode was added at the mid-point between each pair of existing electrodes. This was repeated until all 32 electrodes were attached.

Next the connection quality was checked by examining the impedance values. As Fig. 2.6 shows, the impedance values from the 32 channels should be uniformly distributed around 500-1500 Ohm. If an impedance value was significantly higher, the ECG electrode was pressed firmly onto the skin, ensuring no hair or other obstructions were present. If all the impedance values were within the 500-1500 Ohm range, one electrode was then disconnect and the remaining electrodes impedance values were monitored to ensure no significant increase occurred. This was repeated for at least 2 different electrodes.

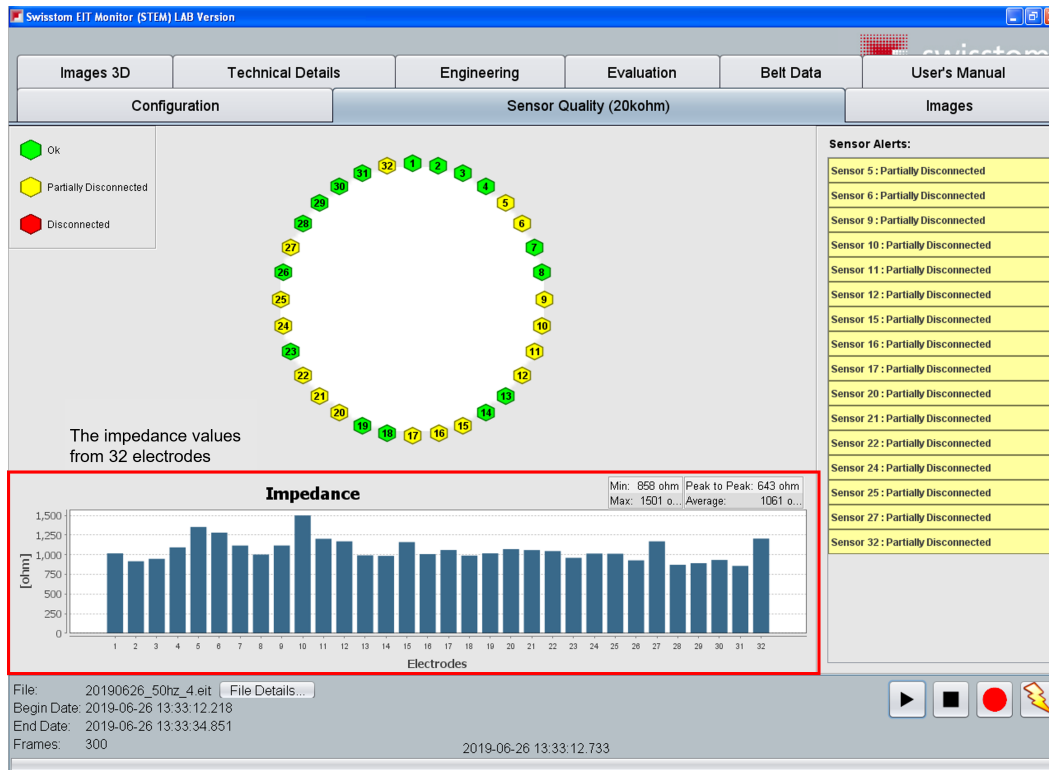


Figure 2.6: Software interface showing the impedance values of the 32 electrodes.

A few variables can be set as shown in Fig. 2.7. The excitation frequency was set at 50kHz and 250kHz, and the injection pattern was set at 0, 1, 2, 4, 8, and 14. The AC current was injected to the upper abdomen through a selected pair of electrodes, and the resulting voltage responses were recorded by the rest of the electrode pairs, resulting in a total of 1024 data points. The injection pattern describes how many electrodes are idle between the working electrode pairs. In this study, the “skipping 4” pattern was used to reconstruct the EIT images [71] (Fig. 2.8), where four electrodes were left idle between the selected pairs for either current injection or voltage acquisition.

Swisston EIT Monitor (STEM) LAB Version

Technical Details | Engineering | Evaluation | Belt Data | SBC Comm. | User's Manual

Configuration | Sensor Quality | Images | Images 3D

Parameter	Current Setting	Next Setting	Range
Calculated Image Rate	14.96	14.96	1.0...100.0 per second
Injection current	3.0	3.0	0.0...10.0 mA (peak)
Excitation Frequency	45	45	50...250 kHz (10kHz step)
Injection pattern	4	4	0...14 skipped electrodes
Switch-settling time	2.0	2.0	Adjust the frequency and injection pattern 0.0...10.0 skipped periods
Number of electrodes	32	32	32 (fixed)
PGA 0 Gain	1	1	0...3
PGA 1 Gain	1	1	0...9

Configuration File: Save Settings to File... Simple

Image Conversion Model:
 Round Basin
 Choose File (press Apply first)

Default Settings Current Settings Apply

SensorBeltConnector Connected Manage Files ...

Freeze SBC ERROR: 0 SBC Status: Belt on [0x01000000]

v 2.3.2 PIONEER rev 818 2014-12-05 CB Hardware: 3 CB Nios Firmware: 02.01.01-r288 MB Hardware: 5 MB Firmware: 1.02-r63 Not Recording

Figure 2.7: Software interface and the programmable current setting.

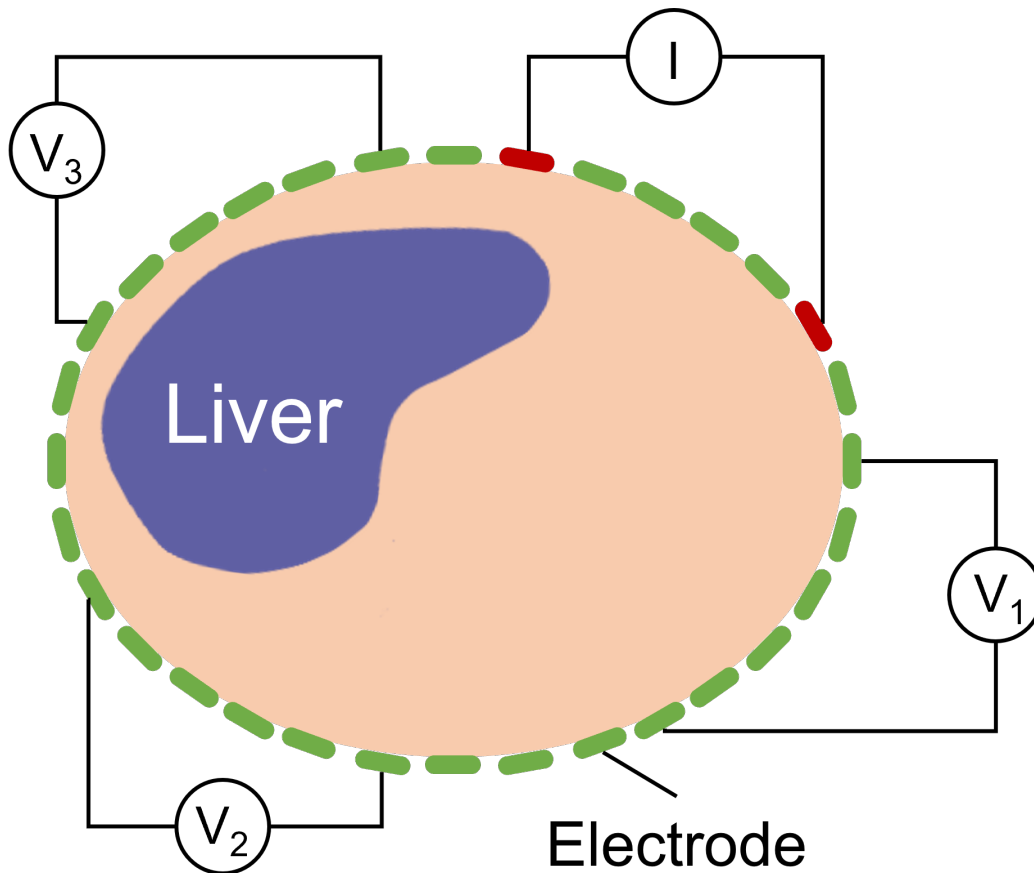


Figure 2.8: Schematic of the EIT current injection and voltage recording. The “Skipping 4” pattern was used for both current injection and voltage acquisition. 4 electrodes separated each pair of stimulating and detecting electrodes.

Other parameters under the configuration such as the injection current, PGA 0 gain and PGA 1 gain are also adjustable (default: 3 mA/2/2). These parameters could affect the IQ plot found in the Engineering tab (Fig. 2.9). The injection current should range from 1-10mA, a PGA 0 gain from 0-3, and a PGA 1 gain from 0-9, all with increments/decrements of 1. These parameters must be adjusted such that the IQ plot shows a linear relation, and the data points are mostly within the green eclipse.

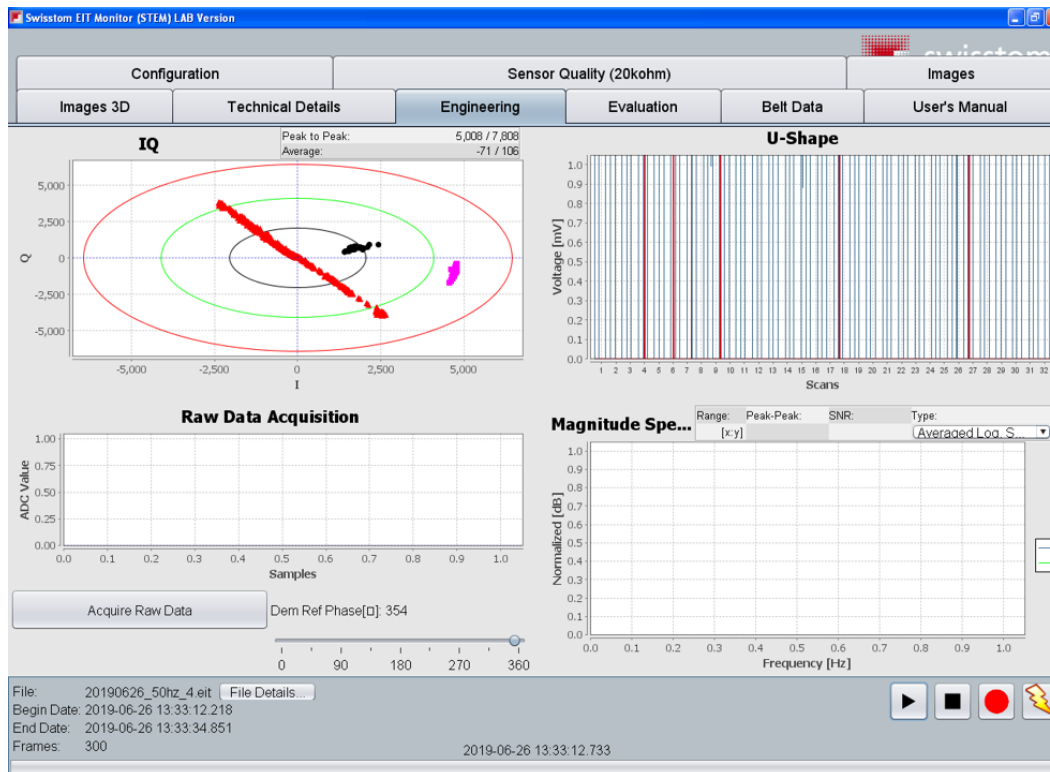


Figure 2.9: Software interface showing the IQ plot (upper left).

Once all the settings were established and the electrodes were attached, the subjects were instructed to take the supine position, and to perform breath-holds (e.g., end inspiration) as they did for the MRI scan. This protocol ensured that the EIT slice matched with the level of the mid-liver MRI slice. The data was recorded for 15-20 seconds for each combination of the frequency and injection pattern.

2.6 Reconstruction of the EIT Images

Reconstruction Algorithm

To reconstruct the EIT conductivity map, we utilized the EIDORS software package and implemented the reconstruction algorithm (see Chapter 1) in MATLAB. For details on the implementation, refer to the Appendix.

In the first section of the code, we define the necessary parameters such as the skipping pattern, injection current, regularization parameter. Then the EIT data is loaded using the function `get_v_data`. Note, the EIT files must be extracted into a `.txt` file in advanced. Next, the finite element model (FEM) is generated using the mesh generator (Netgen). Making the FEM model requires the electrode number, electrode array positioning, electrode shape, the height of the model, the contours,

and the mesh size. The specific contours required are the abdominal cross-section, and the peripheral tissues consisting of the skin, subcutaneous fat, and the ribs (Fig. 2.10). The liver boundary is also required as an input for the solver. We use the `@inv_solve_abs_GN_constrain` solver from the EIDORS package. The regularization parameter is set 5 times larger in the liver region to mitigate any conductivity spikes in the final solution. The Jacobian background value was set to 0.32 which is the average conductivity value of a healthy liver tissue. The average liver conductivity is then calculated and the conductivity map is generated. As mentioned previously, *a priori* geometric parameters are required to reconstruct the 2D EIT images. These values were acquired from the liver MRI images, and a liver segmentation was performed to provide an accurate boundary.

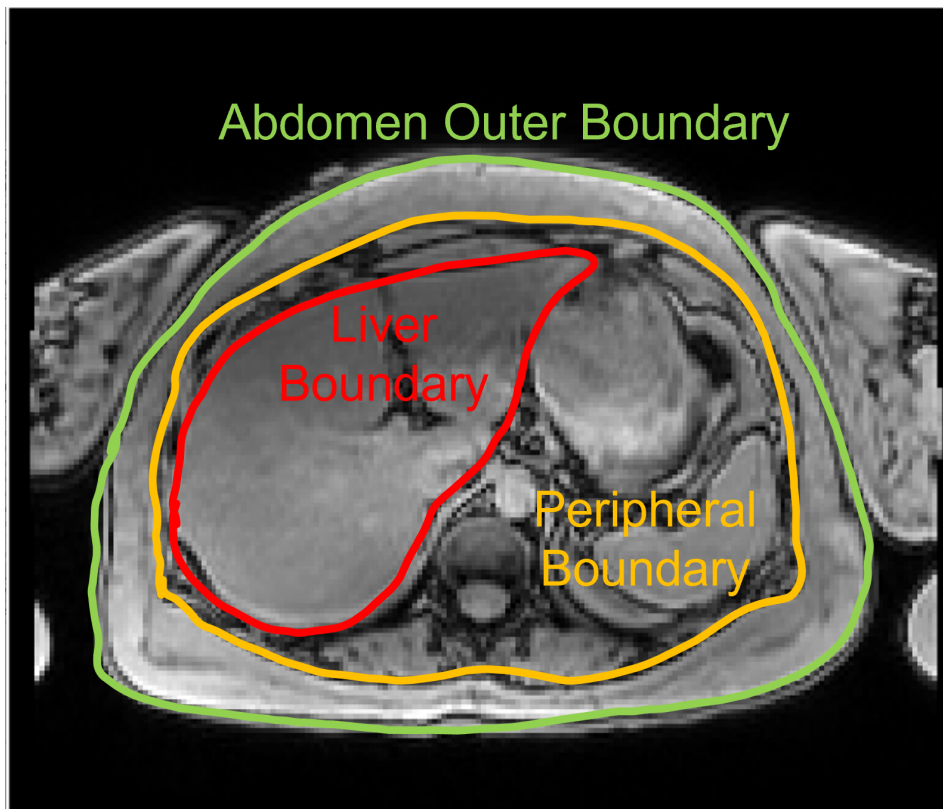


Figure 2.10: The required *a priori* knowledge needed for EIT reconstruction. The geometric information obtained from MRI images is incorporated to stabilize the ill-posed inverse problem. This includes the abdomen outer boundary, the peripheral boundary, and the liver boundary.

The Reconstructed EIT Images

The abdomen MRI images of the liver anatomy and PDFFF, liver segmentation (annotation), and liver EIT conductivity distribution map are shown in Fig. 2.11, Fig. 2.12, Fig. 2.13, Fig. 2.14, and Fig. 2.15. The BMI, PDFFF value, and the average EIT liver conductivity are also provided. The correlation between the liver conductivity and fat content, and other demographics parameters is discussed in the next section.

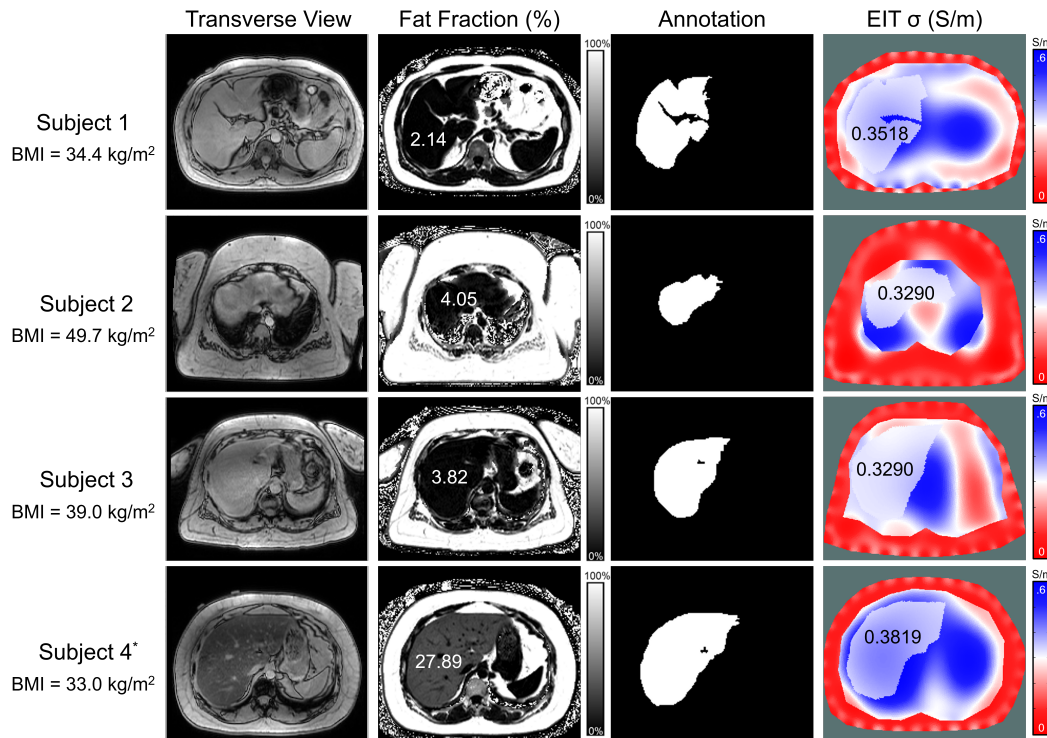


Figure 2.11: MRI multi-echo and EIT images for subjects 1-4. The transverse MRI images show the liver anatomy, the fat fractions provide the corresponding MRI PDFFF, annotation reveals the liver boundary condition following image segmentation, and 2D EIT images unveil the abdomen conductivity distribution and average liver conductivity.

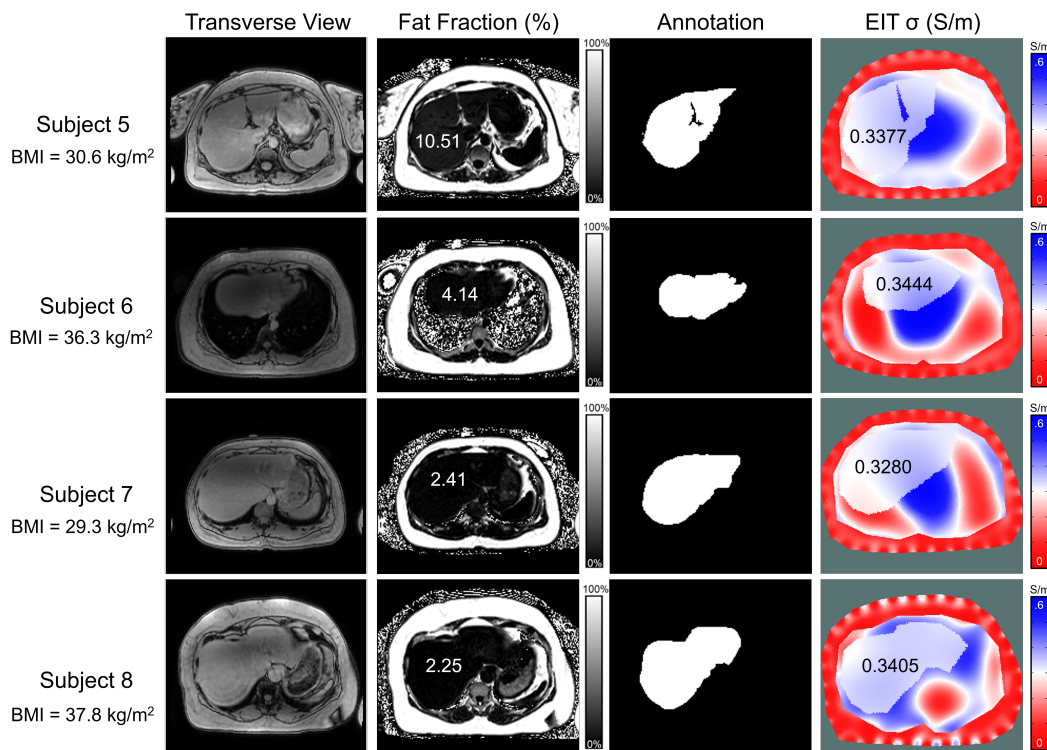


Figure 2.12: MRI multi-echo and EIT images for subjects 5-8.

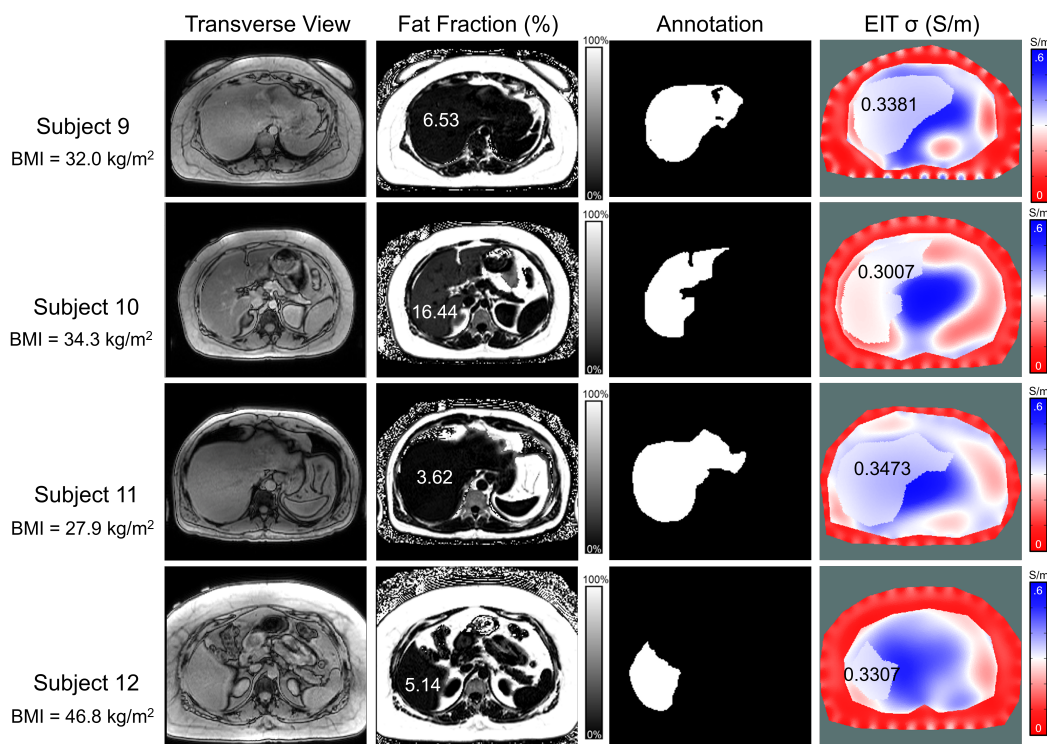


Figure 2.13: MRI multi-echo and EIT images for subjects 9-12.

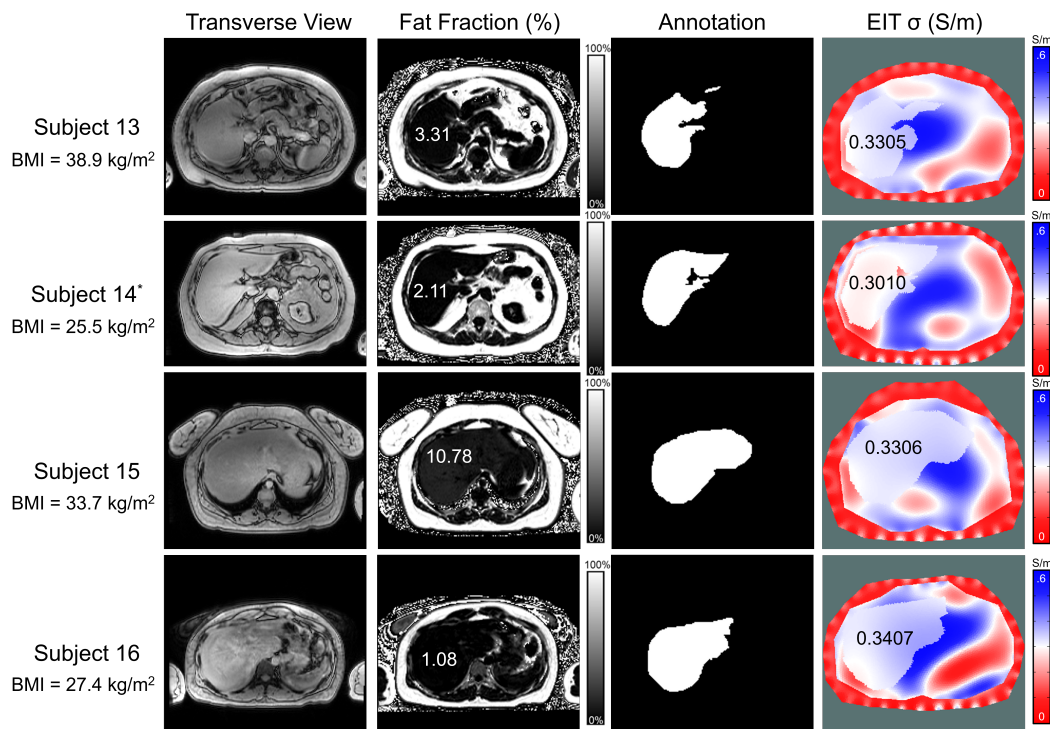


Figure 2.14: MRI multi-echo and EIT images for subjects 13-16.

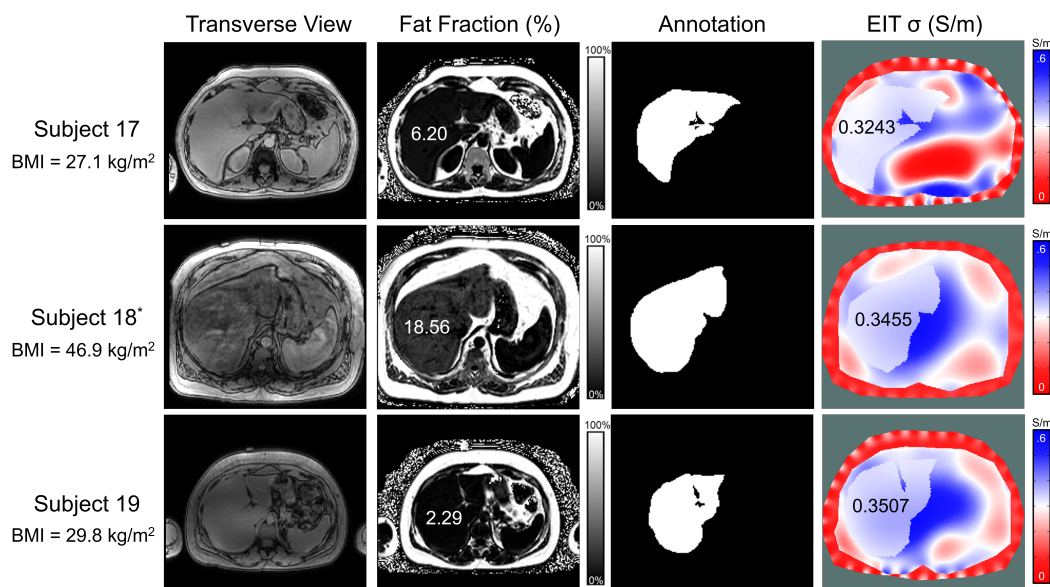


Figure 2.15: MRI multi-echo and EIT images for subjects 17-19.

2.7 EIT and PDFF Correlation

For each subject, the EIT average liver conductivity and MRI PDFF were compared with their corresponding BMI values (Table. 2.1). The injected current for each subject was also recorded.

Subjects	BMI (Kg/m ⁻²)	EIT σ (S/m)	MRI PDFF (%)	Injection current (mA)
1	34.4	0.3518 \pm 0.0192	2.14	1
2	49.7	0.3290 \pm 0.0122	4.05	1
3	39.0	0.3296 \pm 0.0130	3.82	2
4*	33.0	0.3819 \pm 0.0224	27.89	3
5	30.6	0.3377 \pm 0.0211	10.51	2
6	36.3	0.3444 \pm 0.0322	4.14	2
7	29.3	0.3280 \pm 0.0288	2.41	3
8	37.8	0.3405 \pm 0.0134	2.25	2
9	32.0	0.3381 \pm 0.0170	6.53	2
10	34.3	0.3007 \pm 0.0167	16.44	2
11	27.9	0.3473 \pm 0.0168	3.62	2
12	46.8	0.3307 \pm 0.0113	5.14	2
13	38.9	0.3305 \pm 0.0160	3.31	3
14*	25.5	0.3010 \pm 0.0160	2.11	2
15	33.7	0.3306 \pm 0.0127	10.78	2
16	27.4	0.3407 \pm 0.0267	1.08	3
17	27.1	0.3243 \pm 0.0125	6.20	3
18*	46.9	0.3455 \pm 0.0149	18.56	2
19	29.8	0.3507 \pm 0.0189	2.29	2

Table 2.1: BMI (Kg/m²), MRI PDFF (%), EIT liver conductivity (S/m) and injection current (mA) for all subjects. (*: Subject 4; electrode malfunction, Subject 14; renal failure, Subject 18; leukemia)

No significant correlation was found between the MRI PDFF and BMI or liver EIT and BMI results. For example; Subject 17 with a relatively low BMI (BMI = 27.1 Kg/m², PDFF = 6.2%, EIT = 0.3243 S/m) had a higher MRI PDFF than Subject 3 who had a much higher BMI (BMI = 39.0 Kg/m², PDFF = 3.82%, EIT = 0.3296 S/m). However, Subject 11 with a low BMI value (BMI = 27.9 Kg/m², MRI PDFF = 3.62%, EIT = 0.3473 S/m) had a lower MRI PDFF than that of Subject 10 with a higher BMI (BMI = 34.3 Kg/m², MRI PDFF = 16.44%, EIT = 0.3007 S/m).

Furthermore, despite the similar BMI (27.1 Kg/m² vs. 27.9 Kg/m²), the MRI PDFF of Subject 17 was around two times higher than that of Subject 11 (6.20 vs. 3.62 %). Notably, the MRI PDFF for Subject 10 (BMI = 34.3 Kg/m²) was 4 times higher

than that of Subject 3 ($\text{BMI} = 39.0 \text{ Kg/m}^2$). These inconsistent relations suggest that BMI is an inaccurate index to predict the levels of fatty liver infiltrate in an overweight individual.

This insignificant correlation between BMI and EIT conductivity, or BMI and PDFF can be quantified by a Pearson's correlation analysis. We observed that the correlation between BMI and MRI PDFF ($R = -0.037$, $p = 0.89$, $n = 16$) or between BMI and EIT ($R = -0.19$, $p = 0.47$, $n = 16$) was statistically insignificant (Fig. 2.16).

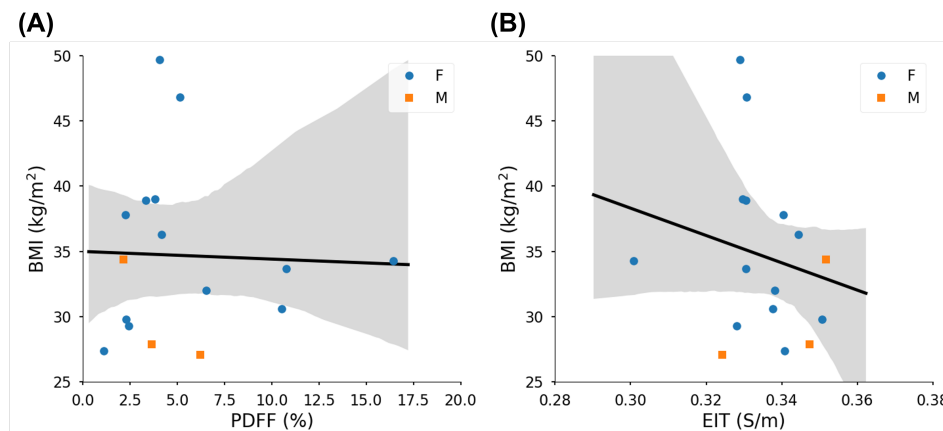


Figure 2.16: Statistical analyses of BMI vs. MRI PDFF and vs. EIT liver conductivity. **(A)** BMI values are not significantly correlated with MRI PDFF. (Pearson correlation coefficient $R = -0.037$, $p = 0.89$, $n = 16$.) **(B)** BMI values are also not significantly correlated with EIT liver conductivity values ($R = -0.19$, $p = 0.47$, $n = 16$.)

The same correlation analysis was conducted for the EIT liver conductivity and MRI PDFF (Fig. 2.17). The correlation plot suggests an inverse correlation between the EIT data and the MRI PDFF ($R = -0.69$, $p = 0.003$, $n = 16$). This finding supports the use of EIT conductivity as an index for non-invasive detection of liver fatty infiltrate.

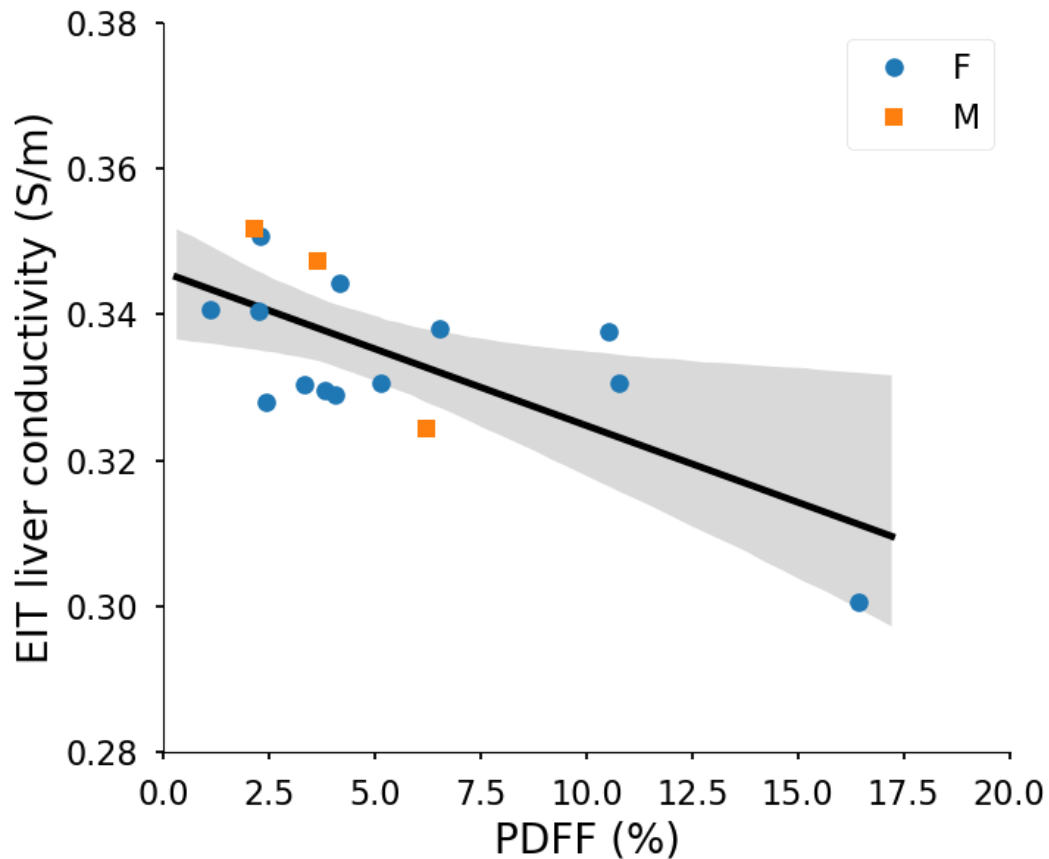


Figure 2.17: Statistical analysis of BMI vs. MRI PDFF and vs. EIT liver conductivity. EIT liver conductivity values were negatively correlated with MRI PDFF ($R = -0.69$, $p = 0,003$, $n = 16$). The shaded region reflects the 95% confidence intervals of the linear slopes.

Modified Exclusion Criteria

In the correlation plots (Fig. 2.17), we excluded the results for three of the Subjects (Subject 4, 14, and 18 which are marked by an asterisk in the Table. 2.1). There was a mechanical issue with the electrode used to study Subject 4, resulting in all voltages being zero. Subjects 14 and 18 were both found to have disorders which are expected to impact the conductivity of blood (chronic lymphocytic leukemia and renal failure). After these exclusions, a sample size of $n = 16$ patients was used for demographic comparisons.

The impact of preexisting medical conditions on the correlation between EIT and MRI-PDFF was further analyzed. The same correlation analysis was performed with $n = 18$ (the entire population) and without individuals with pre-existing medical conditions ($n = 14$).

In Fig. 2.18 (A), the correlation value between the EIT and MRI PDFF decreased from $R = -0.69$ ($p = 0.003$, $n = 16$) to $R = -0.21$ ($p = 0.4$, $n = 18$), if we included the two subjects with electrolyte abnormalities (leukemia and renal failure). If we further excluded the two subjects with anemia, the correlation improved from $R = -0.69$ ($p = 0.003$, $n = 16$) to $R = -0.70$ ($p = 0.0049$, $n = 14$) (Fig. 2.18 (B)). These pre-existing medical conditions are expected to disrupt the impedimetric property of the liver, resulting in an altered EIT conductivity. Future studies should be careful to screen for pre-existing medical conditions that would impact conductivity properties. This sensitivity does however suggest that EIT has the potential to detect abnormal tissue conductivity as these points would fall outside of the linear correlation curve.

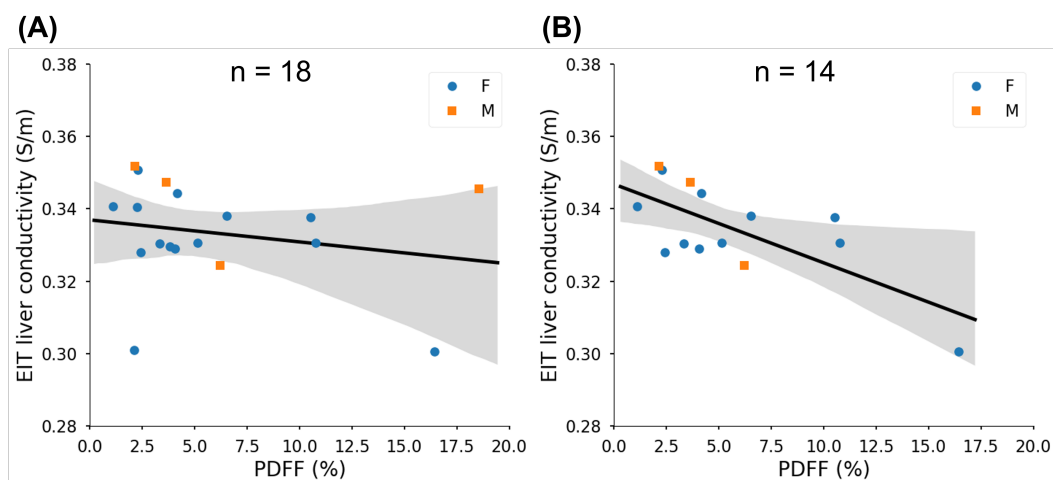


Figure 2.18: Analysis of EIT liver conductivity vs. MRI PDFF for all subjects and results excluding anemic subjects. (A) The negative correlation between EIT conductivity and MRI PDFF was reduced to $R=-0.21$ in the presence of preexisting medical conditions ($p = 0.4$, $n = 18$). (B) The correlation between EIT liver vs. MRI PDFF was increased to $R = -0.70$ in the absence of anemia subjects ($p = 0.0049$, $n = 14$). The shaded areas reflect the 95% confidence intervals of the linear slopes.

2.8 Correlation Analyses with the Demographics Data

To identify fatty liver infiltrate in the enrolled subjects ($BMI > 25$), we performed individual correlation analyses with the waist circumference, height, and weight (Table. 2.2). We compared the correlation coefficients between the MRI PDFF and demographics, as well as anthropometric parameters in the 16 subjects (Fig. 2.19). Following a Bonferroni correction for multi-testing, the correlations with age ($R = -0.13$, $p = 0.64$, $n = 16$), waist circumference ($R = -0.23$, $p = 0.4$, $n = 16$), height ($R = -0.59$, $p = 0.016$, $n = 16$), and weight ($R = -0.41$, $p = 0.12$, $n = 16$) were found to

be statistically insignificant. Of note, height was significant at the nominal cut off of 0.05.

We further compared the correlation coefficients between the liver EIT and demographics, and anthropometric parameters in the 16 subjects (Fig. 2.20). The correlation with age ($R = -0.1$, $p = 0.71$, $n = 16$), waist circumference ($R = -0.05$, $p = 0.85$, $n = 16$), height ($R = -0.63$, $p = 0.0092$, $n = 16$), and weight ($R = -0.19$, $p = 0.47$, $n = 16$) were statistically insignificant when multiple testing was considered. Height was again found to be nominally significant. Thus, these analyses corroborate that BMI and other parameters were not correlated with liver fat infiltrate in overweight subjects.

Subjects	Sex	BMI (Kg/m ⁻²)	Age (year)	Waist Circumference (cm)	Height (cm)	Weight (kg)
1	M	34.4	41	116	175	105.2
2	F	49.7	67	131	158.5	124.7
3	F	39.0	63	123.5	160	99.8
4*	F	33.0	35	116.5	168.9	94.1
5	F	30.6	61	92.5	155.5	73.9
6	F	36.3	27	103.5	163.5	97.2
7	F	29.3	42	91	155	70.3
8	F	37.8	60	115.5	174	114.5
9	F	32.0	36	113	170	92.5
10	F	34.3	36	101.5	152	79.2
11	M	27.9	47	95	178	88.5
12	F	46.8	39	130	160	119.8
13	F	38.9	48	114	168	109.9
14*	F	25.5	74	96	163.5	68.2
15	F	33.7	26	95	153	78.9
16	F	27.4	33	93.5	170.5	79.8
17	M	27.1	47	103	178	85.7
18*	M	46.9	57	141.5	177.5	147.7
19	F	29.8	30	102	180.3	96.9

Table 2.2: Demographics for the 19 overweight subjects including sex, BMI, age, waist circumference, height, and weight. (*: Subject 4; electrode malfunction, Subject 14; renal failure, Subject 18; leukemia.)

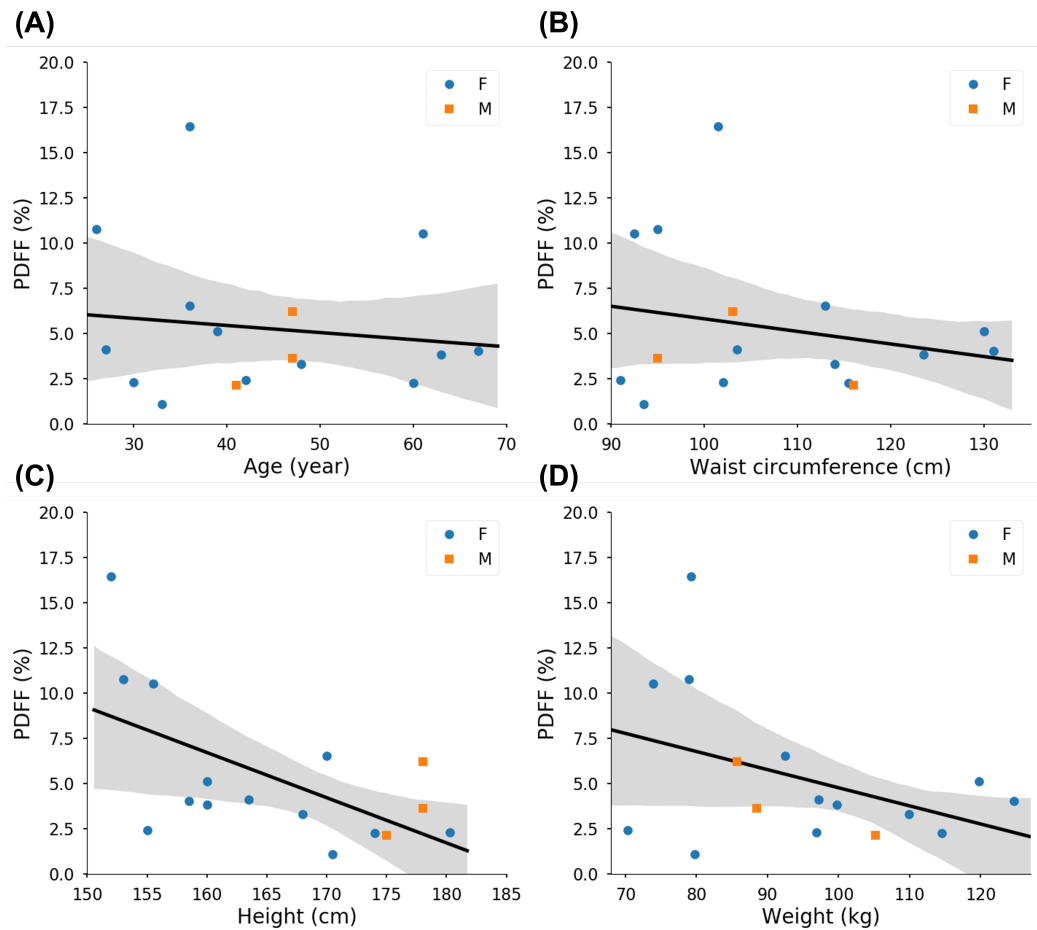


Figure 2.19: MRI PDFF vs. age, waist, height, and weight. The Pearson's correlation coefficients (R) and p values were analyzed for **(A)** age, **(B)** waist circumference, **(C)** height, and **(D)** weight. The circles denote female subjects and the triangles denote male subjects. The 95% confidence intervals of the linear slopes are illustrated as the shaded area. R values are -0.13 for age ($p = 0.64$, $n = 16$), -0.23 for waist circumference ($p = 0.4$, $n = 16$), 0.59 for height ($p = 0.016$, $n = 16$), and -0.41 for weight ($p = 0.12$, $n = 16$), demonstrating low to intermediate correlation with MRI PDFF.

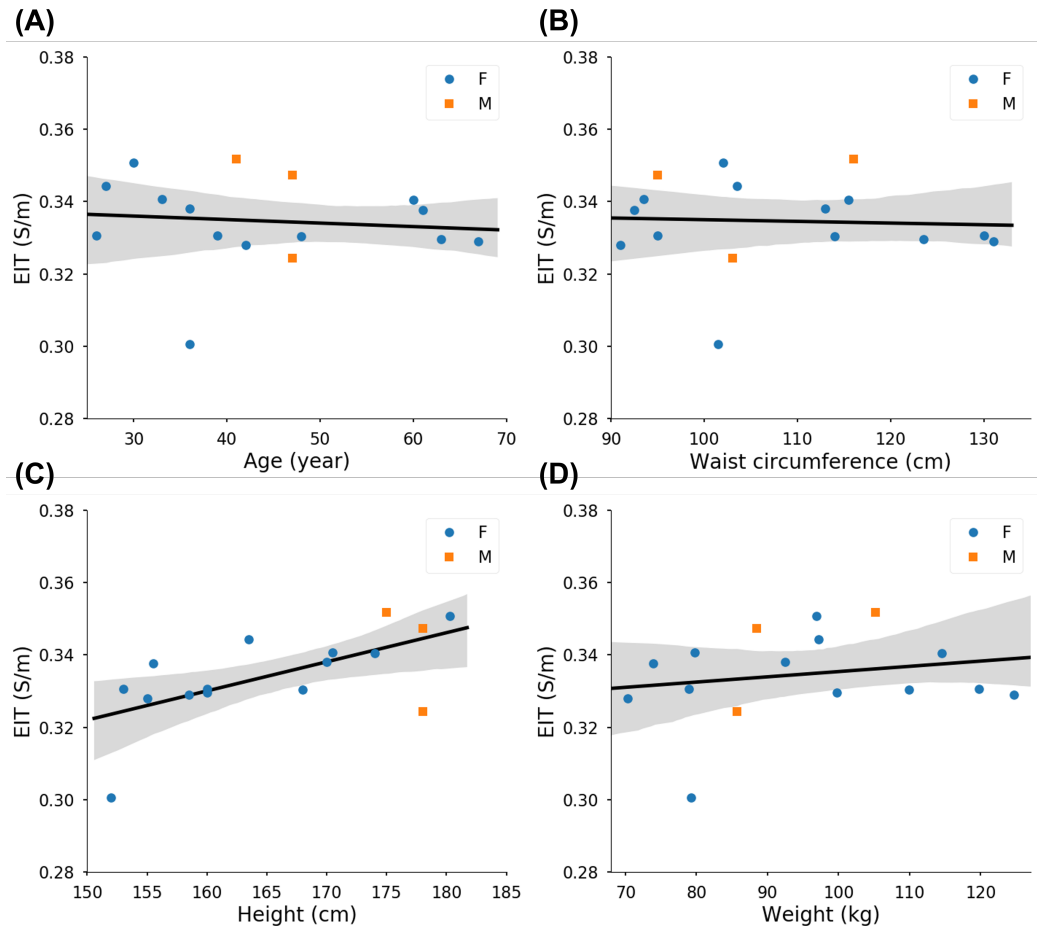


Figure 2.20: EIT liver conductivity vs. age, waist, height, and weight. The R values for age ($R = -0.1$, $p = 0.71$, $n = 16$), waist circumference ($R = -0.05$, $p = 0.85$, $n = 16$), height ($R = -0.63$, $p = 0.0092$, $n = 16$), and weight ($R = -0.19$, $p = 0.47$, $n = 16$) demonstrate low to intermediate correlation with EIT conductivity.

2.9 Discussion

Non-invasive and cost-effective monitoring of fatty liver disease remains to be an unmet clinical need, required for early identification of cardiometabolic disorders. While liver biopsies have been performed to diagnose non-alcoholic fatty liver disease (NAFLD), the risk of bleeding and sampling errors limit their broader application. While a liver MRI is considered the standard non-invasive procedure, it is costly and particularly inaccessible for underserved populations. We have demonstrated that a liver EIT measurement can act as a non-invasive and portable detection method for operator-independent and cost-effective detection of liver content.

Our pilot study recruited 19 adults with $BMI > 25 \text{ Kg/m}^2$ to undergo liver MRI scans. We performed the individual liver EIT measurements with the portable

multi-electrode array, and we used the MRI-acquired *a priori* knowledge of the liver anatomy to solve the inverse problem for EIT reconstruction. We performed correlation analyses on the liver EIT versus MRI PDFF in relation to the individuals' demographics. We have subsequently established a statistically significant correlation between the liver EIT and MRI PDFF.

Although EIT methods have been applied in the medical field for decades, the image reconstruction algorithm is still non-trivial as one must solve a nonlinear forward and inverse model.[72]–[74] These problems are often ill-posed resulting in numerical issues regarding the solution existence, uniqueness, and stability.[75] The non-linear inverse model for EIT reconstruction requires *a priori* knowledge of the anatomic boundaries. This enhances the spatial resolution allowing us to establish an absolute conductivity value.[76] To further improve the EIT reconstruction, investigators have integrated EIT with other imaging modalities, including co-registration with MRI [77] and the introduction of ultrasonic vibrations to the target tissue. This strategy could generate inductive currents within the liver to enhance spatial resolution, thus removing the need for *a priori* knowledge of the liver geometry and position in the abdomen for EIT reconstruction.[78] Alternative approaches have been utilized to address the ill-posed inverse problem for EIT reconstruction. For instance, particle swarm optimization (PSO) was used to solve the EIT equations, an important deviation from the conventional Gauss-Newton methods.[79], [80] Recently, convolutional neural networks (CNN) have also been shown to solve nonlinear inverse problems for EIT reconstruction.[81], [82] Hamilton *et al.* obtained absolute EIT images by combining the D-bar method with subsequent processing using a CNN approach to sharpen the EIT reconstruction.[81] Likewise Li *et al.* utilized deep neural networks (DNNs) to directly obtain a nonlinear relationship between the one-dimensional boundary voltage and the internal conductivity.[82]

The accuracy of EIT reconstruction may be improved by employing multiple levels of the electrode arrays to circumferentially wrap around the upper abdomen. This multi-level electrode array would enable current injection and voltage recordings over the entire liver for a 3D EIT reconstruction. Preliminary results for a 3D reconstruction are presented in Chapter 3. The 3D EIT conductivity distribution is supported by the 3D MRI PDFF rendering image revealing an inhomogeneous fat distribution.

While MRI images provided the *a priori* knowledge to solve the ill-posed inverse problem, alternative methods to generate the boundary conditions would allow for

low-cost liver EIT screening. We propose to apply frequency-differential EIT to obtain the subcutaneous fat layer boundary and utilize strain sensor to acquire the abdomen boundary. More details including some preliminary results are included in Chapter 3.

2.10 Summary

In summary, we enrolled 19 overweight/obese subjects to undergo MRI scans and liver EIT measurements to reconstruct the EIT conductivity distribution. We demonstrated that the increase in liver EIT conductivity is correlated with a decrease in MRI PDFF. No significant correlation between EIT conductivity or MRI PDFF with BMI and demographics data was found. Our correlation analyses support the claim that subject-specific EIT offers a non-invasive and portable method for the operator-independent and cost-effective detection of hepatic fat infiltrate in overweight populations.

*Chapter 3***AN IMPROVED EIT ALGORITHM FOR 3D RECONSTRUCTION
AND DIFFERENTIAL EIT**

Previously we demonstrated an application of EIT to fatty liver detection. In this chapter, we discuss preliminary results improving upon the EIT algorithm itself.

3.1 3D Reconstruction of EIT

Even though we used a 3D model for the EIT reconstruction, the cross-section was the same along the craniocaudal direction. It therefore did not capture the changes in the abdomen geometry along the spine. Instead, the previous reconstruction only captured the plane along which the electrodes were placed. We were unable to recognize the inhomogeneous fat distribution in three dimensional space.

One strategy to address this issue would be the development of a multi-level electrode array. Without this type of array sensor, we instead reconstructed the 3D EIT conductivity similar to the approach discussed in Chapter 2, however, instead of using a uniform cross-section finite element model, we acquired the liver annotation from all the MRI slices to build the FEM.

The 3D rendering of the liver anatomy was established following segmentation of the MRI multi-echo imaging (Fig. 3.1 (A)). The 3D MRI PDFF rendering was generated in a similar way using the PDFF images. In Fig. 3.1 (B), a high fat-fraction area is highlighted in red, showing the heterogeneous distribution of the fat in 3D space. This result was not evident in the previous 2D approach. The 3D EIT conductivity map also shows the heterogeneous gradient of the conductivity (Fig. 3.1 (C)). The dashed red box is consistent with that of the MRI PDFF mapping. Thus, the 3D comparison between MRI multi-echo imaging and EIT image further supports the correlation between MRI fat fraction and EIT conductivity.

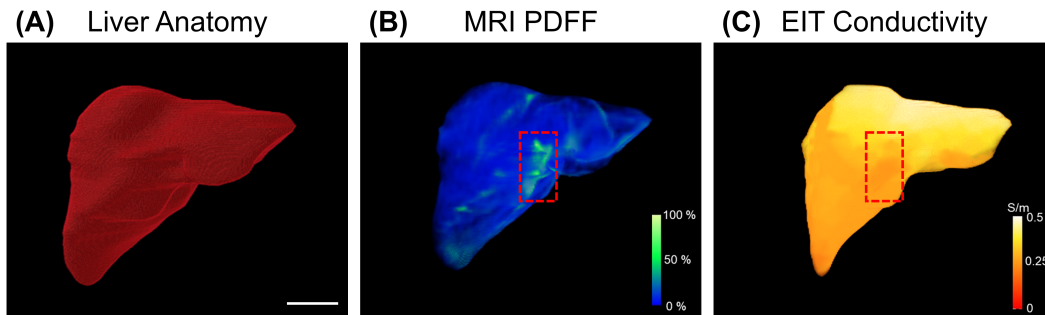


Figure 3.1: 3D rendering images of (A) liver anatomy, (B) MRI PDFF, and (C) EIT liver conductivity. Scale bar: 5 cm.

3.2 EIT Reconstruction without MRI

The *a priori* geometry information derived from an MRI severely limits the accessibility of our previous EIT reconstruction algorithm. An optimal solution to this problem will surely be an important research topic in the future. In this chapter, we investigate the use of strain sensors to acquire the abdomen boundary combined with frequency-differential EIT to obtain the subcutaneous fat boundary.

Abdomen Boundary

Previous studies have proposed integrating the EIT sensors signals with stretch or acceleration to reconstruct the anatomical contour of the upper abdomen.[83]–[86] Khor *et al.* have monitored neonatal lung functions using wearable sensors with a strain gauge and EIT electrodes.[84] de Gelidi *et al.* integrated an accelerometer to detect the dorsal shape using EIT sensors, improving lung-function monitoring.[85] Moreover, Darma *et al.* combined EIT sensors with flexible stretch sensors to measure the contour of the arm for EIT reconstruction.[86] These proposed sensors have the capacity to acquire the change in resistance and to extract the curvature from each sensor based on the pre-established curvature-resistance relation. These examples provide a potential strategy for simultaneously acquiring both abdominal contours and voltage signals in the context of EIT measurements.

Subcutaneous Fat Boundary

A potential alternative method to acquire the peripheral boundary is frequency-differential electrical impedance tomography (fdEIT). Some have proposed that fdEIT can address the technical issues resulting from an unknown boundary geometry and/or uncertainty in the electrode positions.[87] fdEIT allows for reconstructing various tissue conductivities by injecting current at two distinct frequencies to the

abdomen, followed by acquiring the resulting surface-voltage. Sun *et al.* have applied fdEIT to reconstruct the conductivity distribution of calf muscles in response to stimulation. Their reconstruction images illustrated the potential feasibility of distinguishing the boundary between the muscle and subcutaneous fat in a human calf.[88] In addition, Menden *et al.* have recently proposed a reconstruction algorithm for fdEIT using absolute values.[89] These results demonstrated the potential for differentiating between organ and spine boundaries. Accurately selecting the two applied frequencies would have the potential to acquire the peripheral boundary and differentiate the fatty tissues from non-fatty tissues. As a result, the peripheral layer can be used as *a priori* knowledge to solve the inverse problem for EIT reconstruction, thus, obviating the need for an MRI. Furthermore, establishing an atlas of external liver MRI images and an anthropometric database would help calibrate the boundary conditions of the liver to improve EIT reconstruction.

3.3 Preliminary Results for fdEIT

The fdEIT reconstruction is similar to the previously discussed EIT reconstruction. The main difference is that fdEIT requires two sets of voltages recorded at two different frequencies. As a feasibility demonstration, we used the previously acquired data at 50 kHz and 250 kHz, however, more studies would be required to find the optimal range. The representative 2D differential EIT images are presented in Fig. 3.2. The peripheral layer including the skin, subcutaneous fat, and the ribs can be identified and are shown in different colors. One could therefore use this information to define the peripheral boundary and solve the EIT problem. Further algorithm development would be needed to increase the accuracy of this type of peripheral boundary.

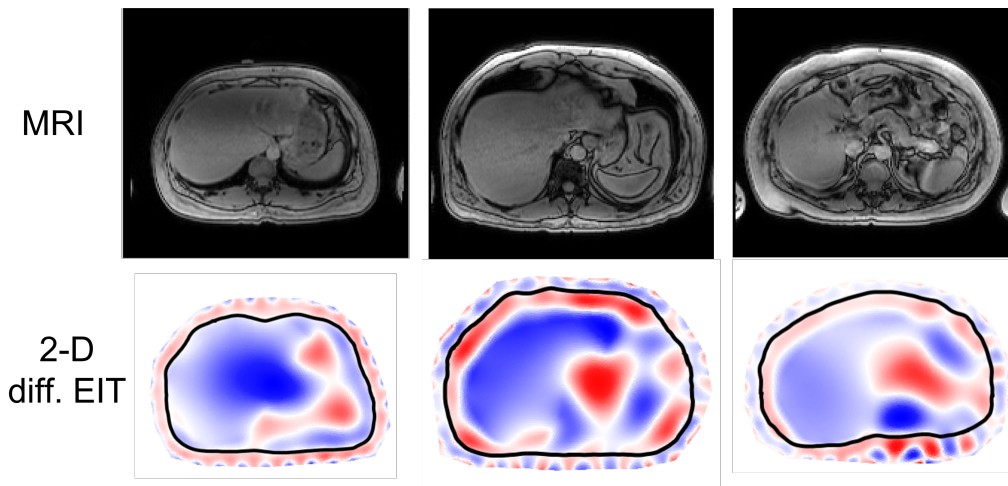


Figure 3.2: Representative 2D differential EIT images compared with MRI images. The voltage data was acquired at 50 kHz and 250 kHz for 2D differential EIT reconstruction. The peripheral boundary is marked in black.

With the peripheral boundary information acquired from the differential EIT, we reconstructed the EIT images with only abdomen boundary information obtained from the MRI images. A form for the topology of the liver was assigned to the upper left region of the abdomen as the liver boundary for all subjects. In this way, only the abdomen boundary information is needed from the MRI. And as discussed previously, this can also be replaced through the use of positional sensors. The representative abdomen MRI images and the liver EIT conductivity maps were compared as shown in Fig. 3.3. Instead of calculating the average liver conductivity over the assumed region, we chose to calculate the average conductivity in the regions that are closer to the electrodes (precision decreases with distance from the electrodes), see Fig. 3.4 (A). We performed a Pearson's correlation analysis and demonstrated that the MRI PDFF and EIT conductivity is correlated ($R = -0.54$, $p = 0.05$, $n = 13$) (Fig. 3.4 (B)). However, the presumed region of the liver and the selection of region for average conductivity calculation would need to be further optimized.

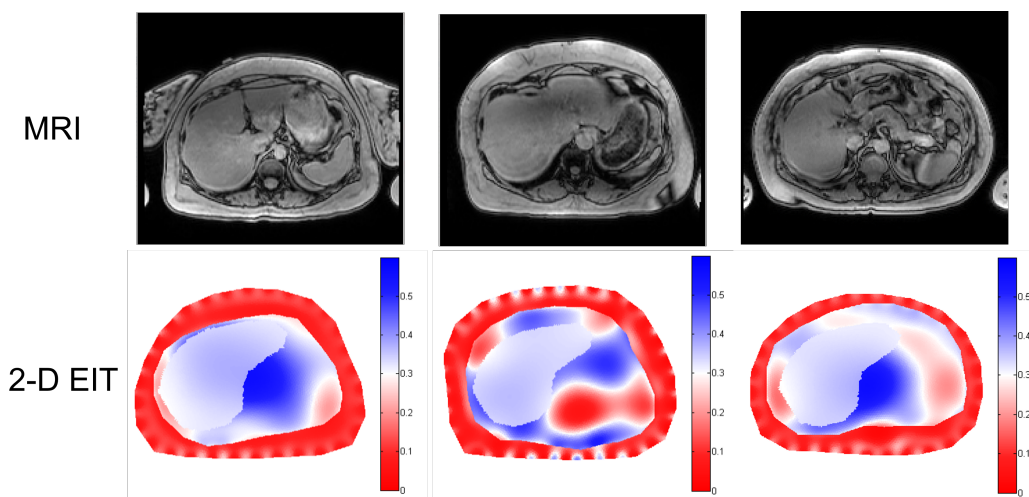


Figure 3.3: Representative MRI and EIT images. Only the abdomen boundary information was acquired using an MRI. The peripheral boundary information was reconstructed by differential EIT and the liver boundary was assumed.

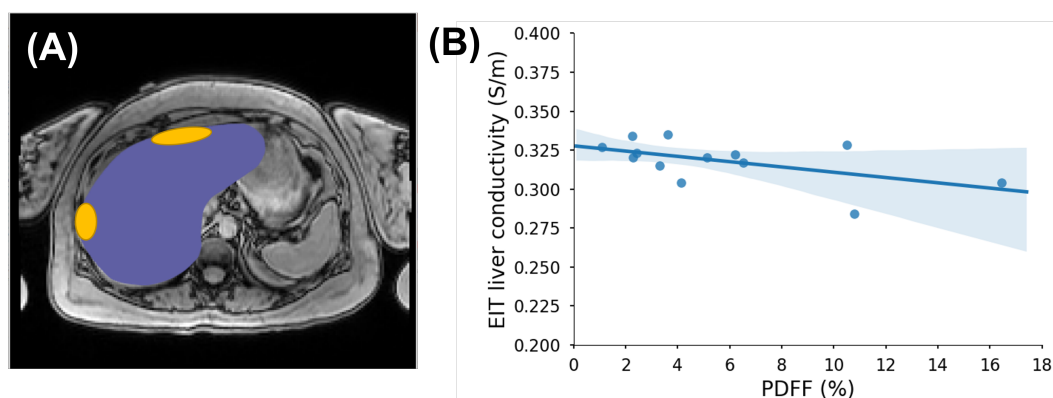


Figure 3.4: Correlation between MRI PDFF (%) and EIT liver conductivity (S/m). **(A)** The liver conductivity distribution was reconstructed within the abdomen including the liver (in purple). But the two regions (in yellow) closer to the electrodes were selected by average conductivity calculations. **(B)** EIT liver conductivity values were negatively correlated with MRI PDFF ($R = -0.54$, $p = 0.05$, $n = 13$). The shaded area reflects the 95 % confidence intervals of the linear slope.

3.4 Summary

In this chapter, we have discussed some improvements to the traditional EIT on fatty liver detection procedure. A 3D liver boundary was used to reconstruct the EIT image and was compared with 3D PDFF rendering. We demonstrated a heterogeneous distribution for the fat in both 3D EIT and 3D PDFF images. Furthermore, the subcutaneous fat boundary obtained by the frequency-differential EIT was uti-

lized in the liver EIT reconstruction. However, the correlation between the MRI PDFF and EIT conductivity can be further explored. Real 3D reconstruction and frequency-differential EIT to assess the boundary are challenges for going forward with an EIT project. Finally, better statistics (i.e. large subject population) would be necessary to further characterize the method.

Chapter 4

OUTWARD EIT FOR INTRAVASCULAR IMAGING

Typical EIT uses an electrode array attached to the outer surface of an object and reconstructs the conductivity distribution of the object by sending electrical current and measuring a response. From an engineering perspective, the construction of the electrode array is an active area of research and development. As outlined in the previous chapters, liver EIT utilizes an electrode array on the surface of the torso. However, an adjustment to the electrode configuration is necessary for different targets, for example a tubular structure would require measurements from the lumen.

This chapter discusses “outward” EIT (OEIT) for intravascular imaging. The importance of intravascular imaging, atherosclerosis detection and monitoring, is discussed in Chapter 6. Due to the low conductivity of lipids, a plaque with a lipid core will innately have a higher impedance. EIT should therefore be able to distinguish the location of plaque from other tissues. This chapter will focus on the electrode configurations and *ex vivo* detection of fatty tissue inside an artery. Details about proximity sensing and conductivity differentiation can be found in [90].

4.1 Outward EIT Device and Experimental Setup

The electrode arrays were designed and fabricated on a polyimide flexible PCB with a polyimide-copper-polyimide sandwich structure (FPCexpress, Ontario, Canada). Each individual electrode was $200\ \mu\text{m}$ wide and 1 mm in length, and the separation between electrodes was $200\ \mu\text{m}$. The entire flexible PCB structure was then rolled onto a 3D-printed PLA cylindrical rod with 5 mm diameter and fixated by silicon adhesive (Fig. 4.1 (A)). Contact pads, 5 mm in width and length were placed at the distal end of the flexible PCB to allow for copper wire connectors to attach to the data acquisition equipment.

The data acquisition equipment was the same as the setup used for the fatty liver detection. The 32 electrodes were connected to the SenTec EIT Pioneer set (SenTec AG, Switzerland). The excitation current was set to be 3 mA at 250 kHz. The “skip 4” pattern was used for both current injection and voltage measurement, where four

idle electrodes were between the selected pair for either current injection or voltage acquisition.

For the *ex vivo* experiments, porcine aorta and fresh whole blood with heparin were used to mimic the intravascular environment. They were purchased from a local animal tissue provider with same day delivery (Sierra Medical, CA). The aorta was cut into a short segment of 10 cm to meet the experimental needs and the diameter was measured around 13.5 mm. Pig fat was purchased from a local supermarket and cut into small pieces to mimic the fatty content in the plaque. The length of the fat was on the order of 6 mm with the cross-sectional dimension measured to $15 \times 3 \text{ mm}^2$, $9 \times 3 \text{ mm}^2$, $5 \times 3 \text{ mm}^2$, $3 \times 3 \text{ mm}^2$, respectively. A sodium chloride solution was dissolved in deionized (DI) water to 0.225 wt % to match the general conductivity value of connective tissue [91] and filled the container space outside the aorta as shown in Fig. 4.1 (B) and (C). The actual conductivity of the solution was confirmed using a benchtop conductivity meter (Mettler-Toledo, OH). The device and the vessel were concentric and the relative position was maintained unchanged during the experiments.

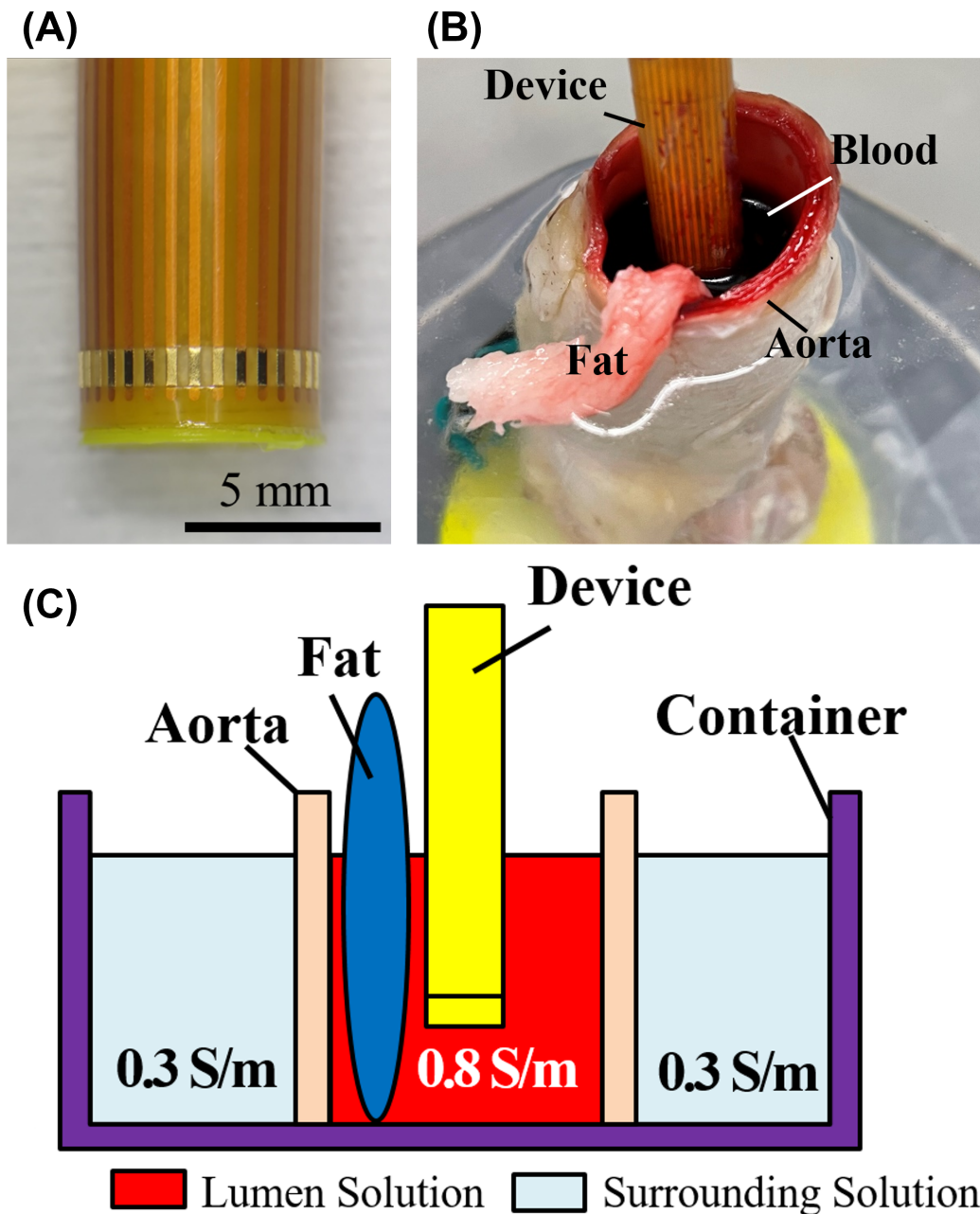


Figure 4.1: Schematics of the outward EIT device and experimental setup. (A) The OEIT device with 32 electrodes wrapped around the cylindrical rod as a catheter. (B) A close-up view of the fat tissue placement inside the aorta filled with real blood. (C) A side view of the setup configuration.

Reconstruction Model

The EIT reconstruction was described in Chapter 1. The implementation again uses the open source library EIDORS, however, slight modifications were made compared to the fatty liver EIT reconstruction described in Chapter 2. Unlike the

liver reconstruction where the electrode array was placed on the outer surface of the model, here a doughnut-shaped finite element model was created and the electrode array was placed on the inner wall as shown in Fig. 4.2. The inner cylinder space was occupied by the OEIT device and was therefore excluded from the domain of interest (DOI). Because our goal was to detect the existence of lipid-rich tissue surrounded by the conductive solution inside the vessel, we chose to ignore the space outside the vessel and any associated electrical impact derived from that region. The inner diameter and outer diameter of the doughnut-shape were set to the diameter of the device (5 mm) and the diameter of the vessel (13.5 mm), respectively.

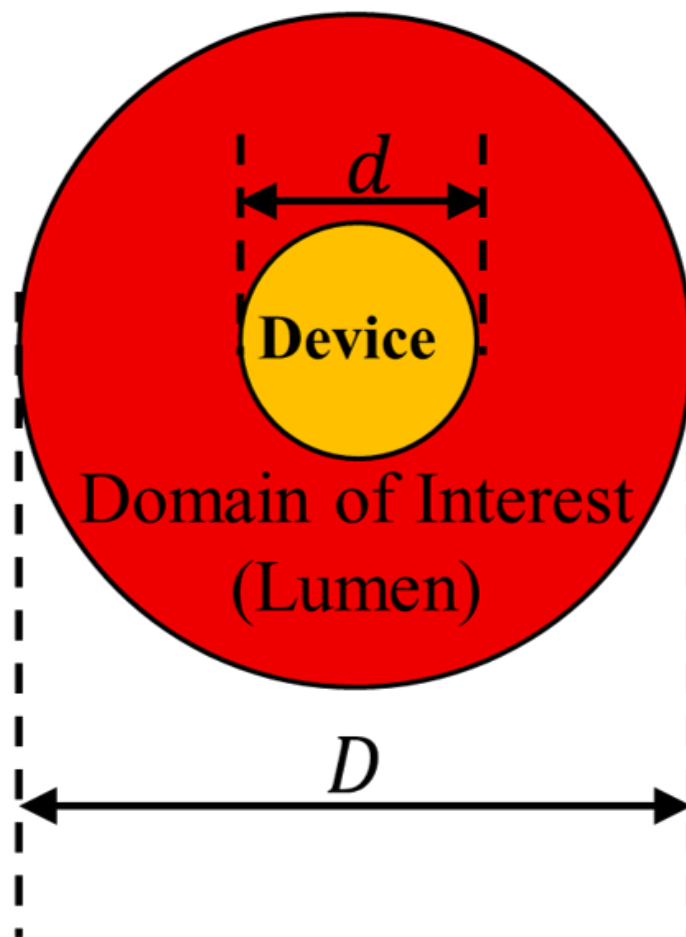


Figure 4.2: Schematic for the reconstruction model.

4.2 *ex vivo* Experimental Results

To demonstrate the ability to assess atherosclerotic lesions within the vessel, we simulated the scenario by placing fatty tissue inside the aorta. The bench-top setup is shown in Fig. 4.1 (B).

Position Detection

The fat tissue was placed inside the aorta at four locations marked by the electrodes numbered: #1, #10, #18, and #25. We then conducted the EIT measurements and subsequently imaged the fatty tissue. This was repeated for four different sizes of fatty tissue ($15 \times 3\text{mm}^2$, $9 \times 3\text{mm}^2$, $5 \times 3\text{mm}^2$, and $3 \times 3\text{mm}^2$). In Fig. 4.3, the lower conductivity region is presented in blue, which is corresponding to fatty tissue. The two larger fatty tissues ($15 \times 3\text{mm}^2$, $9 \times 3\text{mm}^2$) were easily detected compared to the smaller sizes ($3 \times 3\text{mm}^2$). The average conductivity obtained for the fatty tissue was 0.101S/m , which is consistent with the literature, see reference [91].

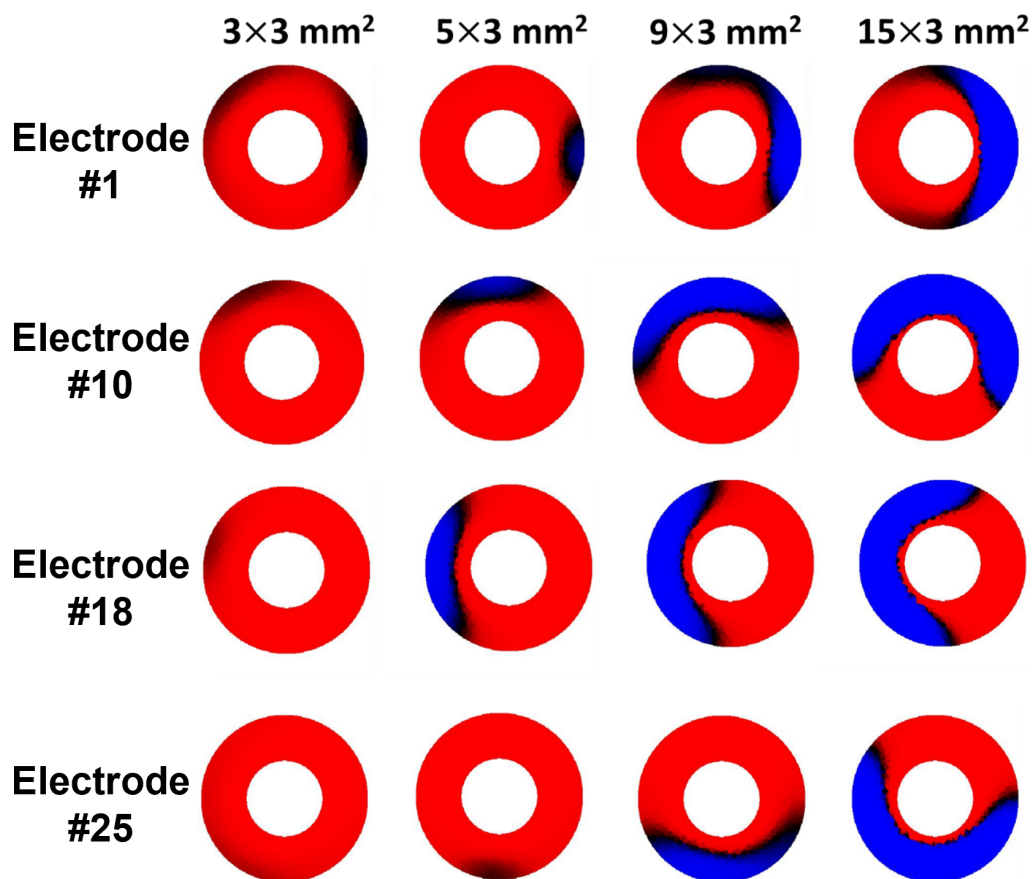


Figure 4.3: Reconstruction images of the 4 different fat tissue sizes immersed in real blood inside an aorta lumen.

Area Analysis

Based on the reconstruction images, we extracted the region of interest, the fatty tissue, and calculated the effective area of stenosis as shown in Fig. 4.4. The effective area is defined as the percentage of cross-sectional area occupied by the fatty tissue within the aorta. The cross-section area of the aorta lumen was found to be $(\frac{13.5}{2})^2\pi = 143.14\text{mm}^2$. For each sample, the actual area of stenosis was calculated to be 31.4%, 18.9%, 10.5%, and 6.3%. In Fig. 4.5, the actual area of stenosis was compared with the values obtained from the extracted images.

While the OEIT device has the ability to detect the location of the fatty tissue for all test sizes, the area analysis for smaller size was noticeably less accurate. The deviation in area stenosis values from the extracted tomographic images is within 35%, except for the smallest fatty tissue size. For this tissue, the area stenosis percentage from the tomographic images was 6 times lower than the actual area. These results indicated the resolution limit for the current device design and experimental set-up with a 6.3% area stenosis. However, it is reasonable to believe that our OEIT has the resolution to identify features as small as 10% of the total luminal area.

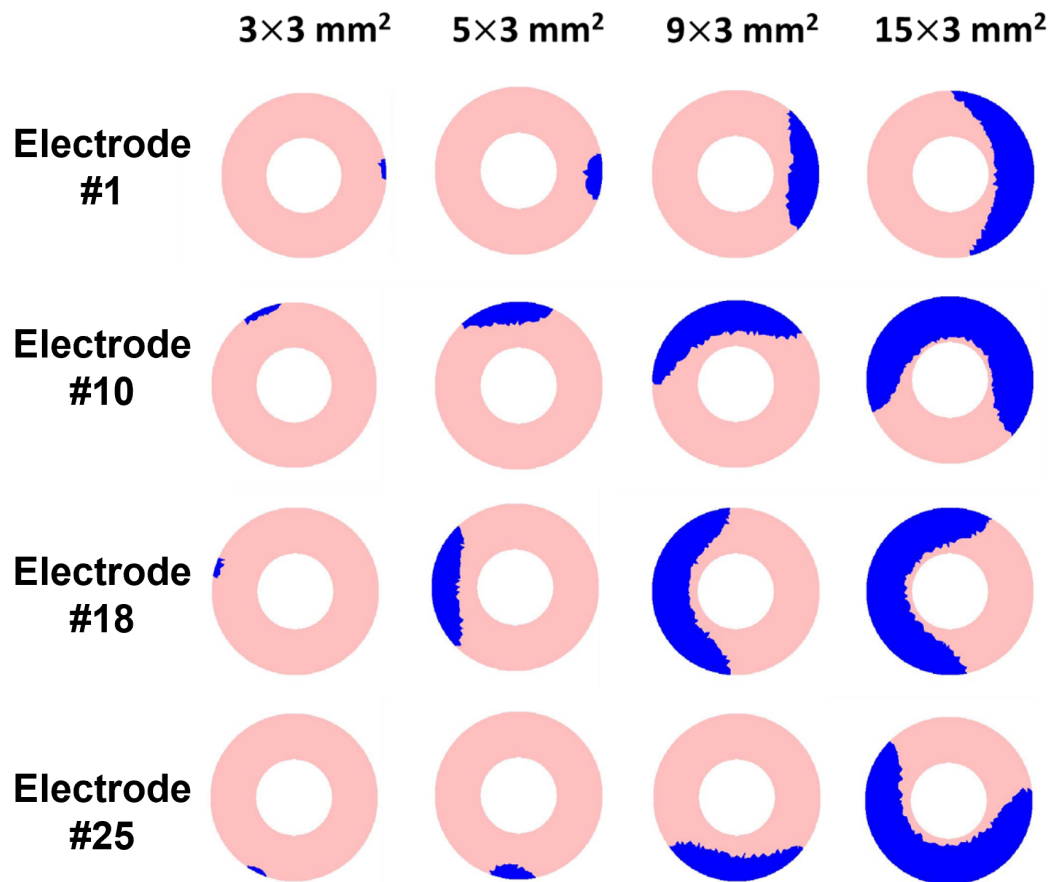


Figure 4.4: The regions of interest identified from the tomographic imaging for all conditions. The area stenosis percentage is the ratio of the area in blue to the overall area.

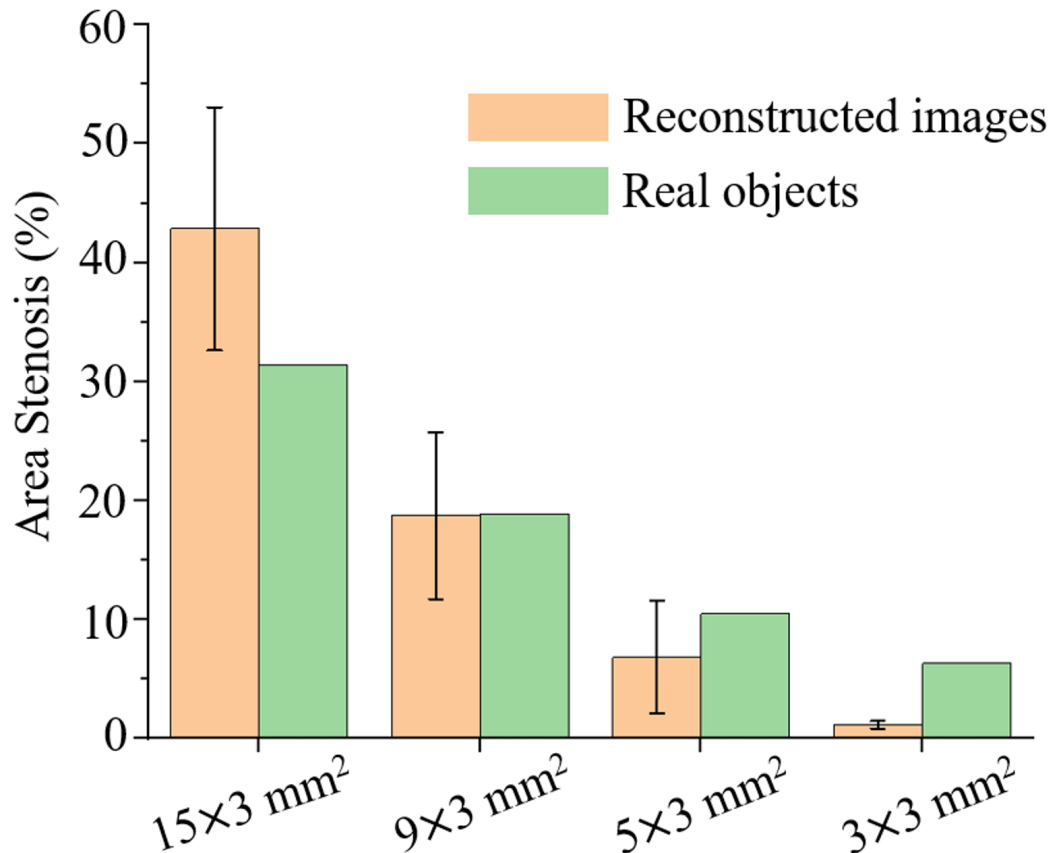


Figure 4.5: Comparison of area stenosis between real samples and tomographic imaging extracted results.

4.3 Discussion

To perform *in vivo* live animal testing using an OEIT device, it will be essential to downsize the current catheter device. In our previous work, a catheter device equipped with impedance sensing electrodes with 1.3 mm overall diameter was fabricated and has been successfully inserted into a rabbit aorta through a 4-French sheath.[92] A larger number of electrodes must be assembled on the surface of an inflatable balloon, such that the impedance data is sufficient to enable EIT reconstruction with high resolution. Kim *et al.* have demonstrated a balloon catheter with more than 32 electrodes for cardiac electrophysiological mapping and ablation which suggests that our method is realistic.[93] Current fabrication techniques allow that the pitch between individual electrodes can be < 0.1 mm through standard microfabrication processes, which translates to an overall diameter of 1 mm with 32 electrodes. However the fabrication and assembly of the small flexible balloon catheter with a 32 electrode array will still require further investigation.

Besides the improvement of the hardware, there is still plenty of room for improving the algorithm for higher resolution and tissue specificity. Currently, we presume a concentric configuration between the device and the aorta, however, the distance between the electrodes and the lesions could affect the measurements and overall performance. Therefore, *a priori* information of the geometry can further improve the precision. As previously mentioned in Chapter 2, we utilized the MRI images for the fatty liver EIT reconstruction. Other intravascular imaging modalities such as IVUS or OCT could be combined with the OEIT to provide further geometry details for reconstruction.

4.4 Summary

In this chapter, the “outward” electrode configuration for EIT reconstruction is described. This outward EIT can be used to image inside a lumen. *Ex vivo* experiments demonstrated the capability of OEIT to detect the location of fatty tissue inside the aorta, and can estimate the degree of stenosis. However, to implement this in live animal testing, one must downsize the balloon catheter while maintaining enough electrodes for an accurate EIT reconstruction. Also, *a priori* information could potentially be needed for higher precision reconstruction.

EIS-DERIVED ELECTRICAL IMPEDANCE TOMOGRAPHY

The previous study has showed that outward EIT is capable of detecting fatty tissue in *ex vivo* arteries. However, the need for numerous electrodes is a major bottleneck for the approach when considering deployment to small arteries for vulnerable plaque detection. It is a major challenge to fabricate small enough electrodes on biocompatible and flexible substrates that can subsequently be combined on a balloon. Parylene-based electronics are a promising direction with potentially micron sized electrode arrays attached to balloon catheters.[94], [95]

In this chapter, we proposed a new reconstruction method for the conductivity distribution via impedance measurements. The impedance values are measured using electrical impedance spectroscopy. Using multiple pairs of electrodes, one can cover the entire 3D space surrounding the tissue of interest. This reconstruction method utilizes the impedance magnitude at a fixed frequency. At the constant frequency, the impedance represents the electrical properties of the tissues, allowing us to reconstruct the 3D conductivity mapping. Compared to EIT approaches, this method can generate the conductivity distribution using less electrodes, and avoid the ill-posed problem. Likewise, this method has an important advantage when compared to traditional EIS: it is easier to visualize the conductivity allowing for a better understanding of the electrical properties of the tissue.

5.1 Theoretical Framework for EIS-derived EIT

The overall work flow of the EIS-derived EIT reconstruction method is illustrated in Fig. 5.1. We can divide the tissue of interest, i.e. a vessel in this case, into multiple rough elements and assume that each element has a uniform conductivity. Using multiple pairs of electrodes, one can acquire multiple impedance spectra. Treating the impedance magnitude as the resistance, it is possible to approximate a conductivity distribution using the rough elements model. Using the conductivity distribution, the impedance magnitude for each pair of electrodes can be computed and compared with experimental impedance measurements. If the simulation error is large, a new conductivity distribution can be generated using a minimization algorithm (the genetic algorithm in this work) and the simulated impedances can be

recomputed. This approach can then be iterated upon until a desired error threshold is achieved.

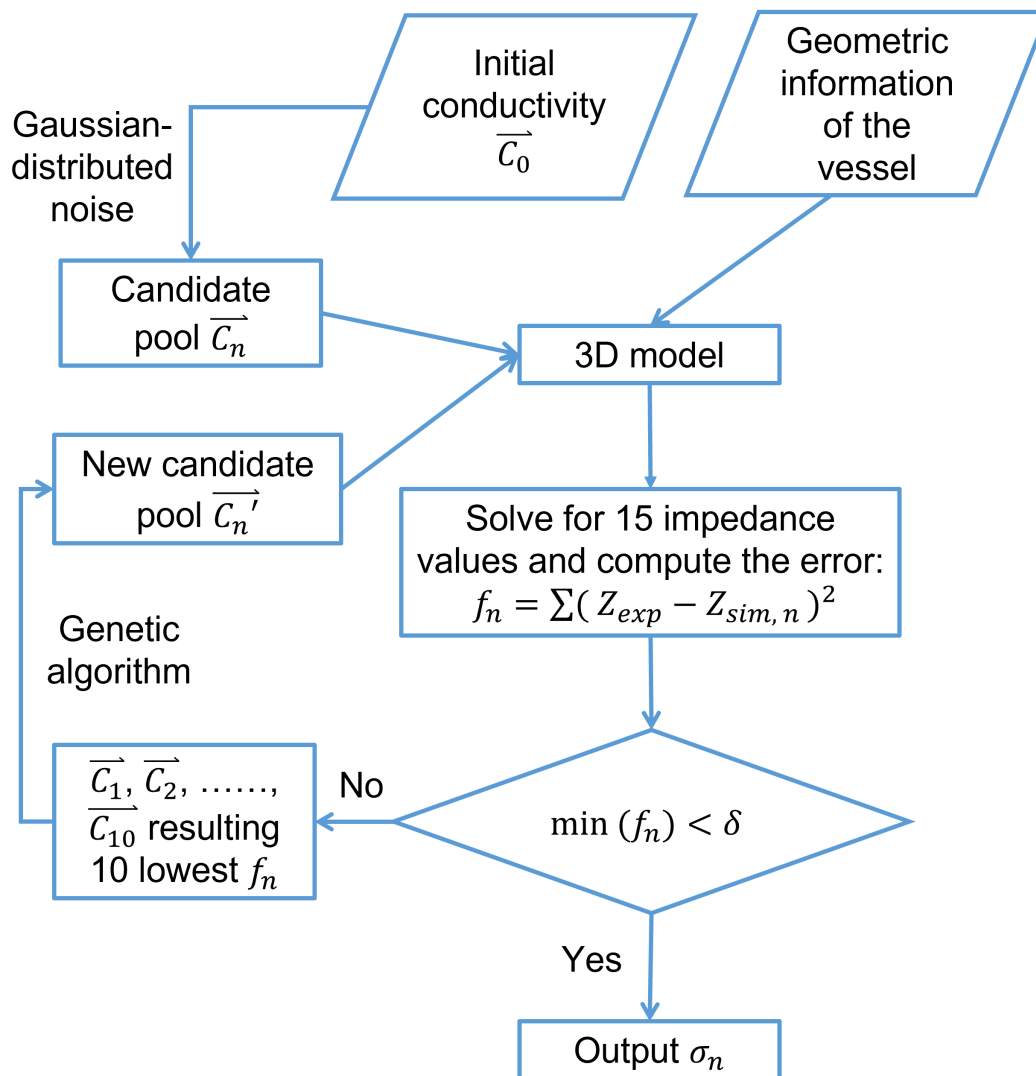


Figure 5.1: Schematic for the EIS-derived EIT.

5.2 3D Model of the Reconstruction

This section will define the 3D element model that was implemented for the work discussed in Chapter 6. An impedance computation was performed at 10 kHz based on the fading of the electrode contact impedance beyond 1 kHz (Fig. 5.2). This frequency captures the resistance resulting from the collagen, lipids, and smooth muscle within the arterial wall, while the reactance contribution is negligible.

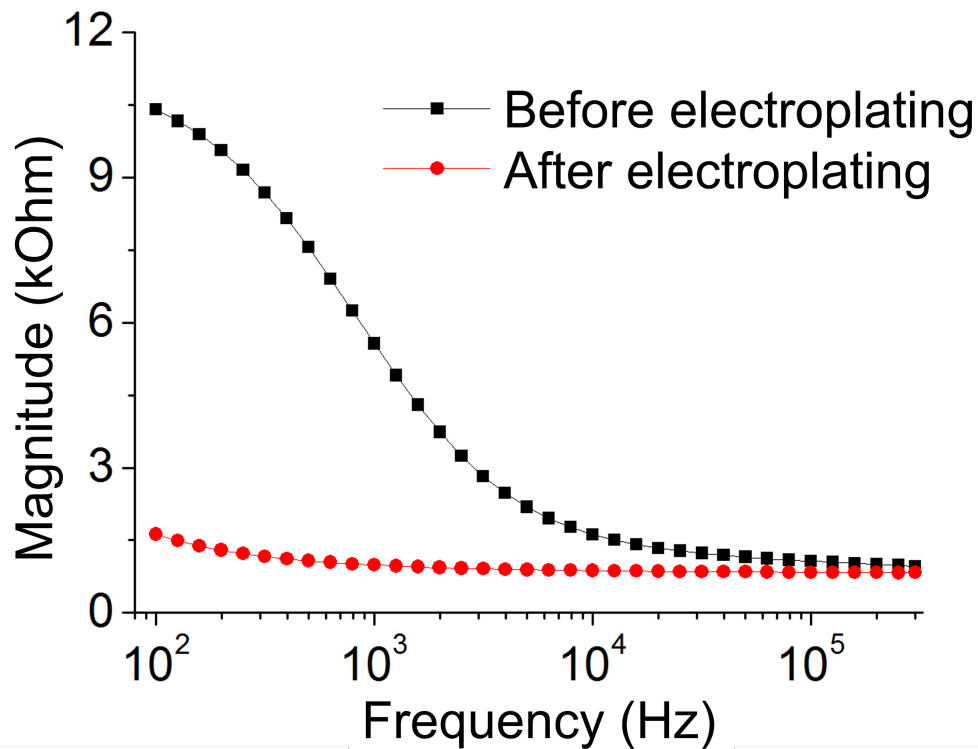


Figure 5.2: A comparison between before and after Pt-black electroplating which demonstrates a significant decrease in contact impedance.

To reconstruct the 3D EIS-derived EIT mapping, we utilized the EIDORS (version 3.8) [96] package to reconstruct 3D models of the arterial segments (composed of 864 elements). The z axis contained 8 layers, each of which was 0.5 mm thick. The center of each row of electrodes was fixed at $z = 1$ and $z = -1$, respectively. In each layer, the arterial wall was decomposed into 3 rings: inner ring, outer ring, and collagen ring, where the inner and outer rings were used to represent the smooth muscle cell layer. Each ring was then divided into 36 elements with each element separated by 10 degrees (Fig. 5.3).

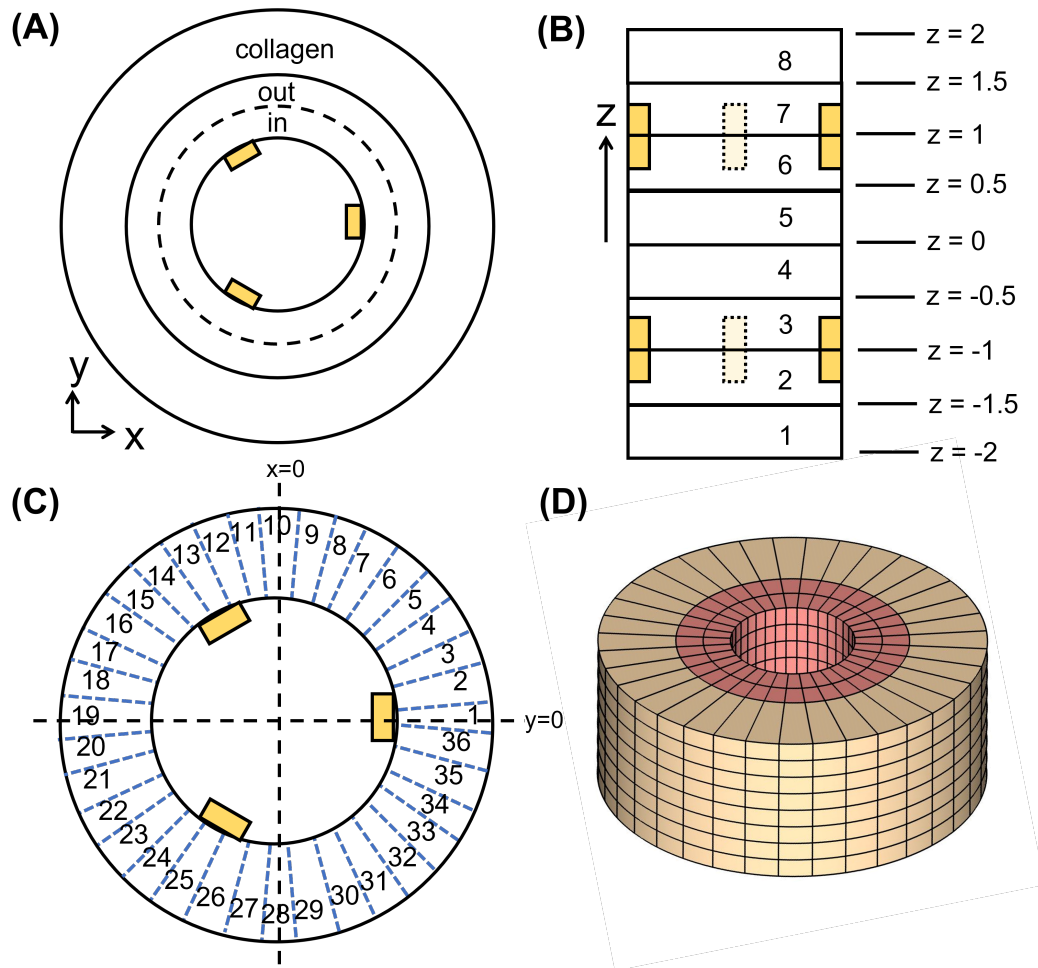


Figure 5.3: Schematics for the model. **(A)** The arterial wall was comprised of three rings: inner and outer define the smooth muscle while the third ring represents collagen. **(B)** The vessel wall was divided into 8 layers in the z dimension. **(C)** Each ring contains 36 elements separated by 10 degrees. **(D)** The 3D model of the arterial wall (864 elements), where yellow regions represent collagen, and red regions represent smooth muscle.

The three parameters: lumen radius, vessel wall radius, and the collagen radius are defined for the reconstruction model. Fig. 5.4 visualizes each parameter. The values of these parameters for the three reconstruction cases in Chapter 6: the left carotid, right carotid #1, right carotid #2 are listed in the Table. 5.1. The numerical value used represents the average value taken from every slice of the Movat histology images (Fig. 6.13, Fig. 6.14, Fig. 6.15).

(mm)	Left Carotid	Right Carotid #1	Right Carotid #2
Lumen radius	2.35	1.3	1.6
Vessel wall radius	4.22	2.72	3
Collagen radius	5.65	5.9	5

Table 5.1: Dimensions of the artery models.

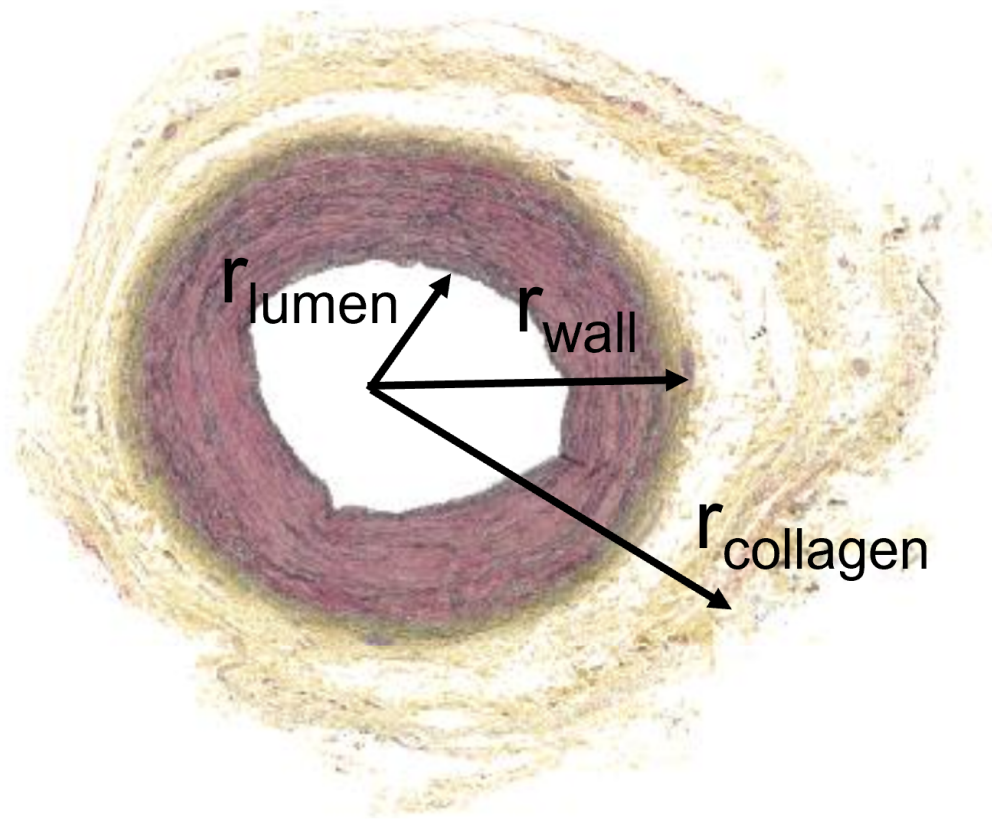


Figure 5.4: The lumen radius, vessel wall radius, and the collagen radius illustrated using a Movat histology slice.

5.3 Initial Conductivity

Assuming each element is uniform, we derived the initial impedance/conductivity for the smooth muscle layer from the EIS measurements at 10 kHz. This was done by modeling the artery as a impedance network and establishing a corresponding circuit diagram (Fig. 5.5).

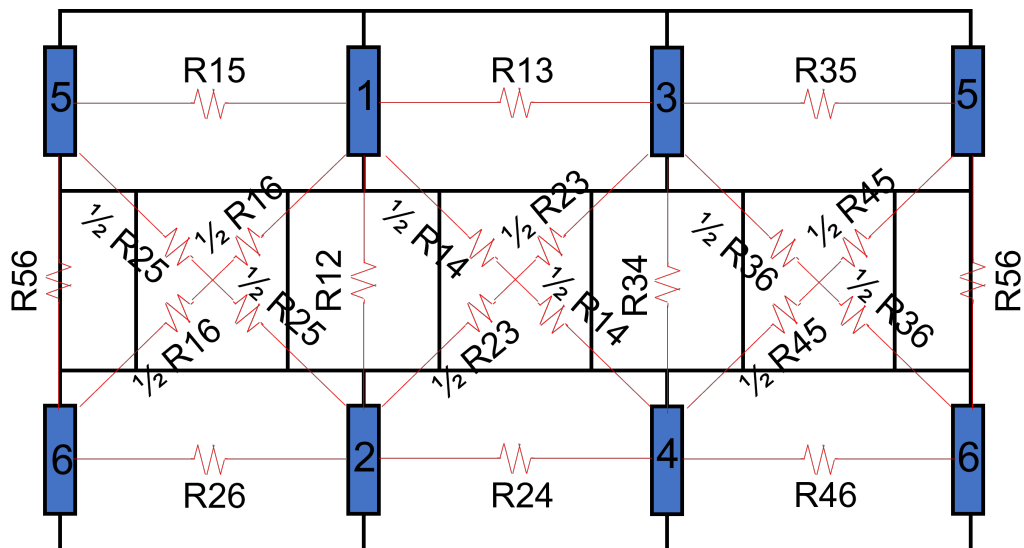


Figure 5.5: The circuit diagram for the 6-electrode network. The region between sets of electrodes is represented as a resistance value, R_{ij} .

The measured impedance value from each pair of electrodes can be modeled using the following equations:

$$\begin{aligned}
\frac{1}{Z_{1,3} \text{ measured}} &= \frac{1}{Z_{13}} + \frac{1}{Z_{15} + Z_{35}} + \frac{2}{Z_{14} + Z_{23}} \\
\frac{1}{Z_{3,5} \text{ measured}} &= \frac{1}{Z_{35}} + \frac{1}{Z_{13} + Z_{15}} + \frac{2}{Z_{36} + Z_{45}} \\
\frac{1}{Z_{1,5} \text{ measured}} &= \frac{1}{Z_{15}} + \frac{1}{Z_{13} + Z_{35}} + \frac{2}{Z_{16} + Z_{25}} \\
\frac{1}{Z_{2,4} \text{ measured}} &= \frac{1}{Z_{24}} + \frac{1}{Z_{26} + Z_{46}} + \frac{2}{Z_{23} + Z_{14}} \\
\frac{1}{Z_{4,6} \text{ measured}} &= \frac{1}{Z_{46}} + \frac{1}{Z_{24} + Z_{26}} + \frac{2}{Z_{45} + Z_{36}} \\
\frac{1}{Z_{2,6} \text{ measured}} &= \frac{1}{Z_{26}} + \frac{1}{Z_{24} + Z_{46}} + \frac{2}{Z_{25} + Z_{16}} \\
\frac{1}{Z_{1,4} \text{ measured}} &= \frac{1}{Z_{14}} + \frac{1}{Z_{12} + Z_{24}} + \frac{1}{Z_{13} + Z_{34}} \\
\frac{1}{Z_{2,3} \text{ measured}} &= \frac{1}{Z_{23}} + \frac{1}{Z_{12} + Z_{13}} + \frac{1}{Z_{24} + Z_{34}} \\
\frac{1}{Z_{1,6} \text{ measured}} &= \frac{1}{Z_{16}} + \frac{1}{Z_{15} + Z_{56}} + \frac{1}{Z_{12} + Z_{26}} \\
\frac{1}{Z_{2,5} \text{ measured}} &= \frac{1}{Z_{25}} + \frac{1}{Z_{26} + Z_{56}} + \frac{1}{Z_{12} + Z_{15}} \\
\frac{1}{Z_{3,6} \text{ measured}} &= \frac{1}{Z_{36}} + \frac{1}{Z_{34} + Z_{46}} + \frac{1}{Z_{35} + Z_{56}} \\
\frac{1}{Z_{4,5} \text{ measured}} &= \frac{1}{Z_{45}} + \frac{1}{Z_{34} + Z_{35}} + \frac{1}{Z_{46} + Z_{56}} \\
\frac{1}{Z_{1,2} \text{ measured}} &= \frac{1}{Z_{12}} + \frac{2}{Z_{25} + Z_{15}} + \frac{2}{Z_{14} + Z_{23}} \\
\frac{1}{Z_{3,4} \text{ measured}} &= \frac{1}{Z_{34}} + \frac{2}{Z_{23} + Z_{14}} + \frac{2}{Z_{36} + Z_{45}} \\
\frac{1}{Z_{5,6} \text{ measured}} &= \frac{1}{Z_{56}} + \frac{2}{Z_{25} + Z_{16}} + \frac{2}{Z_{36} + Z_{45}}
\end{aligned} \tag{5.1}$$

where $Z_{ij, \text{measured}}$ is the impedance value measured during the experiments across electrode i and j , and Z_{ij} is the impedance of the block between electrodes i and j (Fig. 5.6). Note that the impedance of the region in-between two pairs of electrodes is the average of the impedance of the region between the two diagonal electrodes. The value of each Z_{ij} can be obtained by solving the above 15 equations.

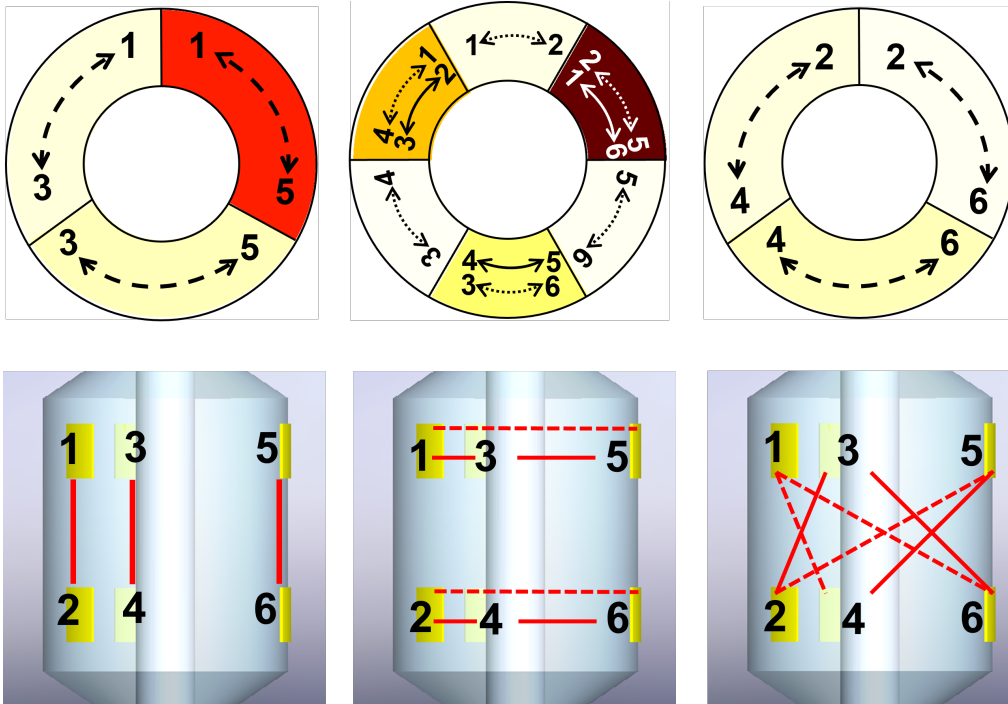


Figure 5.6: Configuration of the 6-point electrodes on the EIS sensor. Results in 15 permutations which are represented by segmented impedance heat maps.

With the calculated Z_{ij} values corresponding to a coarse 12-element (Fig. 5.7 (A)) mapping scheme, we sought to further refine the mapping by dividing the model into a total of 576 elements to represent the smooth muscle (Fig. 5.7 (B)). The conductivity value for each element was obtained by using the impedance value divided by a geometry factor (the element sizes are small enough to be approximated as equal). There appeared to be multiple elements sharing the same conductivity, we therefore added another annular layer (Fig. 5.7 (C)) to represent the collagen layer observed in the histology. Larger elements with uniform conductivity value were used to present the collagen resulting in a final model with 864 elements.

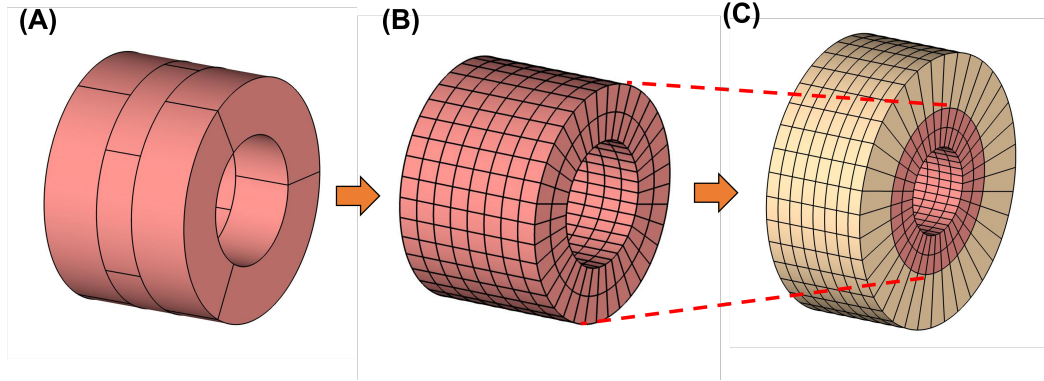


Figure 5.7: The finite element 3D model. (A) 12-element mapping scheme for the initial conductivity calculations. (B) 576-element mapping scheme representing the inner smooth muscle cell. (C) 864-element mapping scheme including the collagen layer.

5.4 Optimization of the Conductivity Distribution

We varied the conductivity distribution such that it optimally reproduced the 15 permutations for the impedance measurements. The so-called “genetic algorithm” was used to “evolve” the elements to reach the final mapping results.[97], [98] The implementation was as follows: the conductivity value from each of the 864 elements was considered as an 864×1 vector. We generated a solution candidate pool (100) by adding Gaussian-distributed noise to this initial 864×1 vector, $\vec{C}_1, \vec{C}_2, \dots, \vec{C}_{100}$. For each candidate we then calculated the 15 impedance values ($Z_{12, \text{sim}}, Z_{13, \text{sim}}, \dots, Z_{56, \text{sim}}$) by solving the Laplace equation.

We defined our fitness function as follows:

$$f = \sqrt{\sum_{i,j=1, i \neq j}^{15} (Z_{ij, \text{measured}} - Z_{ij, \text{sim}})^2}. \quad (5.2)$$

The “genetic algorithm” was implemented with the following steps:

1. Calculate the fitness function for all of the solution candidates within the pool.
2. Rank the candidates according to their fitness function from small to large.
3. Identify the top ten candidates from the pool: $\vec{C}_1^*, \vec{C}_2^*, \dots, \vec{C}_{10}^*$
4. Generate a new pool of 90 candidates as follows:

$$\vec{C}_i^* = \sum_{k=1}^{10} \left(\sigma \lambda_k \vec{C}_k^* + (1 - \sigma) \lambda_k \frac{\sum_{l=1}^{10} \vec{C}_l^*}{10} \right), i = 11, 12, \dots, 100 \quad (5.3)$$

where $\sigma = 1.3$ is a factor to control the boundaries of the candidate space obtained from the above equation, and $\sum_1^{10} \lambda_k = 1$. [98]

Steps 1-4 were repeated until the minimum fitness function reaches a predefined target. The solution candidate $C_1^{\vec{\text{final}}}$ was then used to assign the conductivity distribution resulting in the final conductivity mapping. We excluded the outermost layer as the calculated conductivity distribution was fairly homogeneous, i.e. the heterogeneity resided within the inner layer (576 elements).

5.5 Matlab Implementation

To reconstruct the EIS-derived EIT conductivity map, we utilized EIDORS and implemented the algorithm described previously in MATLAB. The code can be found in the Appendix.

The first section of the code calculates the impedance values for a given conductivity distribution. Similar to the EIT algorithm, we define various parameters such as the number of electrodes, the dimensions of the artery model, the injection current, and the regularization parameter. Next, the finite element model (FEM) is created using the mesh generator (Netgen). To make the FEM model we need to define the electrodes positions, electrodes shape, and the mesh size. Unlike the EIT algorithm, the skip pattern is a fixed parameter that is dependent on the measurement settings, in this appendix we iterate over the skip pattern from 0 to electrode number - 2. For the 15 permutations (based on the 6-points EIS device), the number of electrodes in between the working and counter electrode ranges from 0 to 4.

Next, we divide the FEM into 864 elements by defining each element using the mesh coordinates and assign the conductivity values. This is the major difference between the EIT algorithm and EIS-derived EIT algorithm as the EIS-derived EIT algorithm is solving a forward problem. The solver we use here is `fwd_solve`, which calculates the resulting voltage of each pair of electrodes. To obtain the impedance, we simply divide the voltage by the injection current.

The second part of the code is the implementation of the genetic algorithm. Using the initial conductivity, a random value is added as noise to generate a new set of conductivities and the impedance values are computed to obtain a fitness value. This process iterated another 99 times to create the candidate pool. Next the candidates resulting in the 10 lowest fitness values are used to create a new candidate pool. Mutations in the conductivity are added by randomly changing the conductivity of

several elements. This process is repeated until the fitness value reaches a defined target.

5.6 Summary

In this chapter, we proposed a new algorithm for reconstructing the conductivity distribution from impedance measurements. Unlike traditional EIT which solves an ill-posed inverse problem, this method tackles the reconstruction problem in a forward manner by iterating the conductivity distribution to meet the targeted impedance values. This approach is guided by measurements and requires less electrodes. This method could be more time-consuming and the initial conditions (initial conductivity) plays an important role as the optimization problem must overcome numerous local minima. The local minima optimization problem is well-known and future research may consider more advanced algorithms compared to the simplistic genetic algorithm. In the next chapter, this reconstruction method is applied to atherosclerosis detection.

EIS APPLICATION FOR ATHEROSCLEROSIS DETECTION

6.1 Atherosclerosis

Cardiometabolic syndromes, including hyperlipidemia, obesity, and diabetes constitute a rising epidemic in the United States. These often “silent” disorders are associated with chronic diseases including atherosclerosis.[99] Atherosclerosis is a disease in which the artery wall develops a buildup of fats, cholesterol, and other substances. These plaques (aka lesions) can lead to the narrowing of the blood vessels, blocking of blood flow, or even blood clots when they burst.[100] These types of plaques are prone to rupture (vulnerable plaques), which can lead to myocardial infarction and stroke.[101], [102] While the rupture can cause acute coronary syndromes, the vulnerable plaque is usually asymptomatic and makes it difficult to manage.

The three main characteristics define a vulnerable plaque compared to a “stable plaque” are: a thin fibrous cap, a large oxidized lipid-rich necrotic core, and infiltration with macrophages and inflammatory cells as shown in Fig. 6.1. The thin fibrous cap is usually less than $65 \mu\text{m}$ [103] and percentage of infiltration by the macrophages is $14 \pm 10 \%$ [104]. Likewise, the large necrotic core can occupy up to a quarter of the plaque.[105] Other standard features include a positive vascular remodeling, increased vasa-vasorum neovascularization, and intra-plaque hemorrhage.[106]–[110] A plaque rupture occurs when the fibrous cap is biomechanically disrupted in the presence of shear stress due to the usual hemodynamic pulsating expansion that occurs during systole and elastic recoil contraction during diastole. Thus thrombogenic subendothelial factors are exposed to the bloodstream, resulting in platelet adhesion, activation, and aggregation.[101]

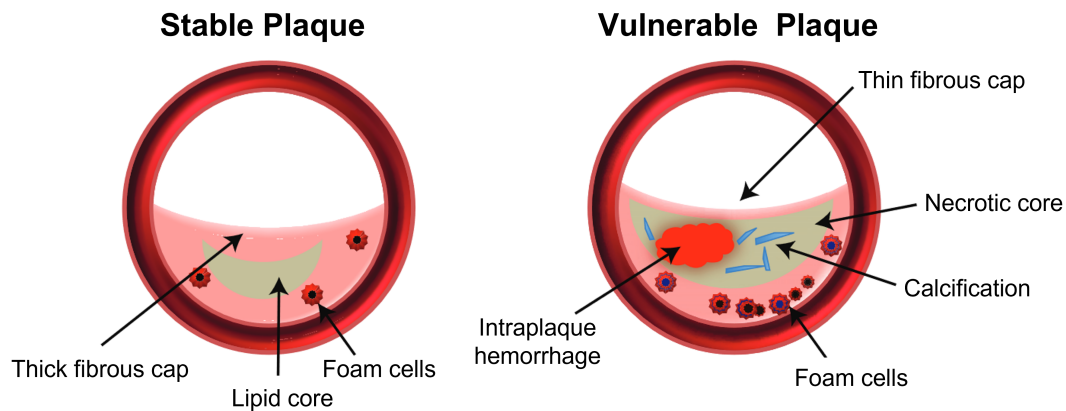


Figure 6.1: Illustrations of a stable (left) and a vulnerable plaque (right). Adapted from reference [111].

Diagnostic Methods

Numerous techniques have previously been developed to detect high-risk plaques before rupture. Angiography has been the gold standard for assessing the severity of obstructive luminal narrowing by visualizing the radio-opaque contrast agent injected into the blood vessel via X-ray techniques. While it can be used to assess the lumen boundaries, it is unable to detect plaque composition or vulnerability to spontaneous rupture. Fractional-flow reserve (FFR) measurements [112], defined as the ratio of pressure across the stenotic lesions ($P_{\text{downstream}}/P_{\text{upstream}}$) during coronary catheterization [113]–[115], are often deployed to assess hemodynamically significant lesions with intermediate severity.[116]–[118] However, the predictors for metabolically active, albeit non-obstructive, lesions prone to rupture remain undefined by FFR, resulting in a false negative rate of over 20%. [119] A sensor that could identify the composition of plaque would be very beneficial to add to the angiography procedure with an FFR sensor.

Other imaging modalities that utilize catheter-based sensors have also been developed for plaque diagnosis. The standard-of-care technique for detecting intravascular thrombus is angiography, which visualizes the endoluminal surface via a flexible fibre bundle in an endoscope catheter.[120] While it can be used to identify vulnerable plaques (as the color is different angiographically for thick and thin fibrous caps [121]), a blood-free field must be created by total occlusion of the vessel which can lead to ischemia. Also, no information about the depth of the plaque can be provided.[122]

Intra-vascular ultrasound (IVUS) provides real-time high-resolution images of the cross-sectional images of the vessel wall by detecting the reflected or scattered ultrasound signal.[123] It can provide anatomical characteristics of the plaque, however, the conventional IVUS is limited by its ability to characterize the plaque components to determine the vulnerability.[124] To overcome these limitation, some IVUS-based methods have been developed via post-processing methods such as virtual-histology IVUS (VH-IVUS), integrated backscatter IVUS (IB-IVUS), and iMAP. The distinct plaque characteristics can be represented by superimposing a color scheme on the ultrasound images.[125]

Optical coherence tomography (OCT) can acquire cross-sectional images of vessels by measuring the intensity of back-reflected light via an optical fiber probe.[126] Even though OCT has a very high resolution which could potentially identify and detect normal arterial wall structures, it suffers from limited tissue penetration.[120] The main drawback of OCT is the need for saline flushes. The removal of blood between the sensor and arterial wall is essential to obtain clear images and is usually done through balloon occlusion with saline purging.[127]

6.2 Previous Study of EIS on Plaque Detection

Previous work used electrical impedance on human arteries to categorize them into five groups via histology: lesion free, fatty streaks, thin cap with oxidized LDL (oxLDL)-rich lesions, thick cap with oxLDL-absent lesions, and thin cap with calcification lesions.[128] In Fig. 6.2, the normalized biological component resistances (R_B) of the oxLDL-absent lesion were similar to that of lesion-free sites ($p > 0.05$). However, there is a statistically significant difference between the R_B of oxLDL-rich and oxLDL-absent lesions ($p < 0.001$). This study provides the fundamental principle behind using electrical impedance to characterize lesions and verifies the sensitivity and specificity of EIS.

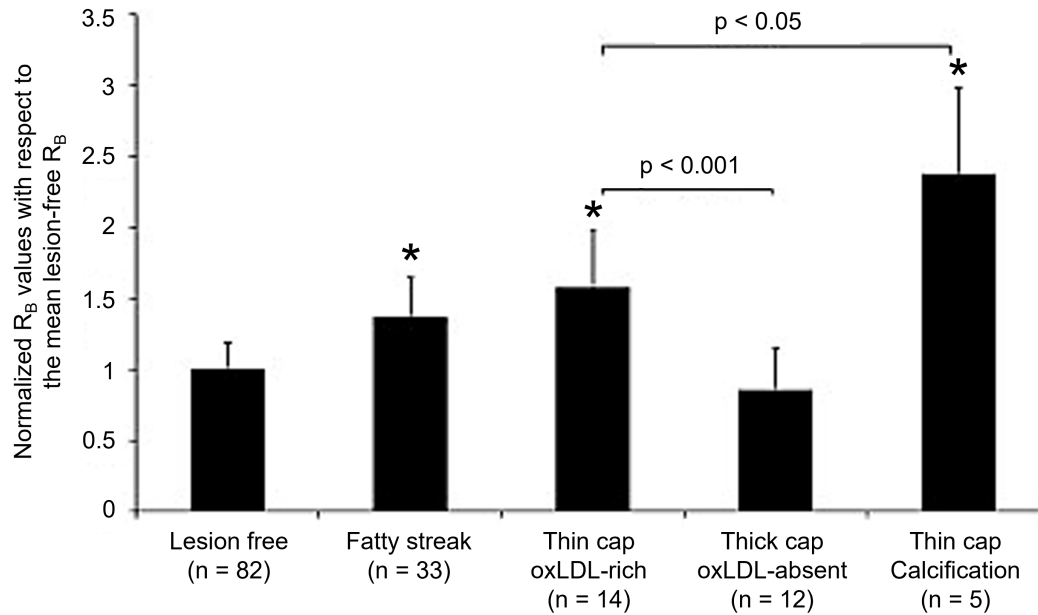


Figure 6.2: The normalized biological component resistance of different types of lesions with and without oxLDL. Adapted from reference [128].

The EIS microelectrode array has also been integrated into balloon catheters to detect oxLDL-rich lesions in rabbit models of atherosclerosis.[92], [129] In Fig. 6.3, the EIS profiles indicated an increase in impedance magnitude with an increase in fat content in the arterial walls characterised by hematoxylin & eosin (H & E) staining (for arterial wall) and oil-Red-O (for lipid).

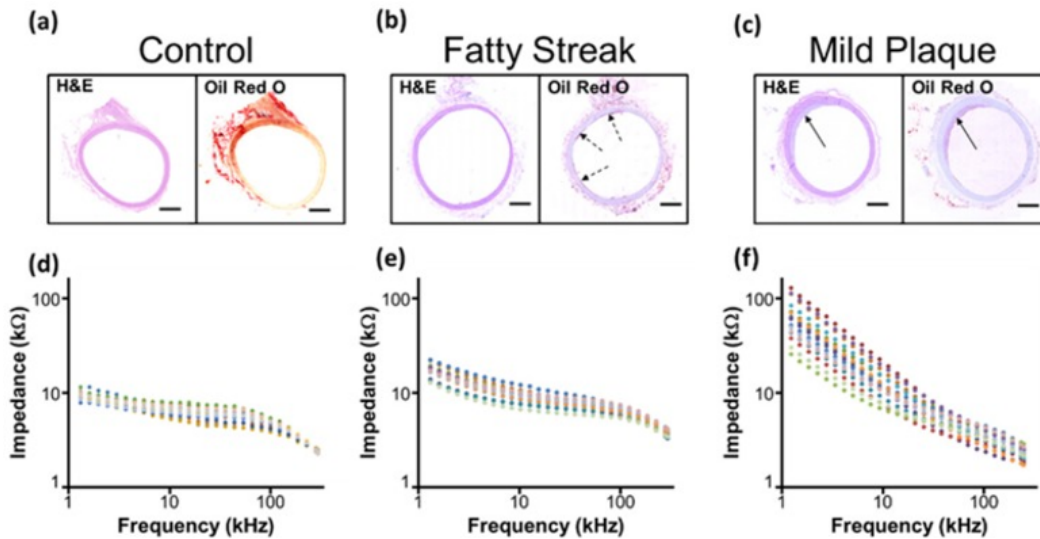


Figure 6.3: Histology images and EIS profiles of a control aorta (left panel), an aorta with fatty streaks (middle panel) and an aorta with mild plaque (right panel). Adapted from reference [128].

Unfortunately the impedance profiles only provided overall information for the vessel. A detailed distribution and location of the plaque or fatty streaks cannot be easily obtained from an impedance spectrum. To further assist diagnosis in the clinical setting, a visualization of the impedance data would be beneficial. We introduced an EIS-derived EIT method described in Chapter 5 to reconstruct the conductivity distribution in the vessel. In this chapter, we will discuss conductivity maps of the arterial walls reconstructed by impedance measurements obtained from an EIS balloon catheter.

6.3 EIS Balloon Catheter

Electrode Design

Flexible polyimide electrodes were used for the EIS measurements. The electrodes layout is shown in Fig. 6.4. The 2 x 3 electrode array was composed of 6 electrodes with a width of 200 μm and a length of 600 μm . The separation between the two rows was 1.4 mm.

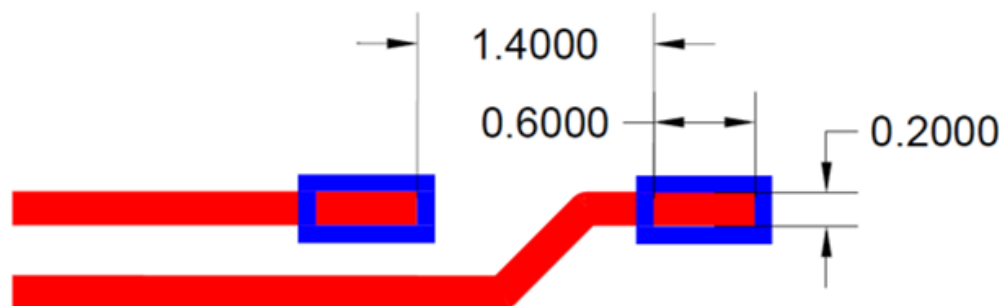


Figure 6.4: Polyimide PCB layout for 6-point EIS. Unit: mm.

The electrodes were pre-constructed (FPCexpress, Ontario, CA) by first depositing a copper layer of $12\ \mu\text{m}$ on the polyimide substrate ($12\ \mu\text{m}$), followed by chemical etching to create the electrode patterns. To insulate the wiring, a second layer of polyimide ($12\ \mu\text{m}$) was laminated to cover the copper, exposing only the electrodes and the contact pads. Then, the exposed electrode surface was plated with a layer of Au/Ni (50 nm/2000 nm) by electroless-nickel-immersion-gold (ENIG) process (Fig. 6.5).

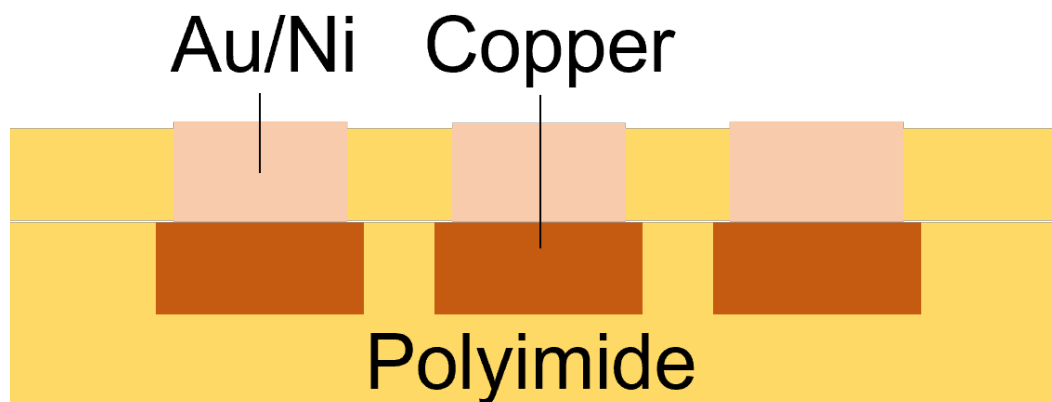


Figure 6.5: Sideview of the polyimide flexible PCB.

To further reduce the interface impedance, the electrodes were electroplated with platinum black (Sigma-Aldrich). 0.3 g sodium dihydrogen phosphate (NaH_2PO_4) and 6.03 g disodium hydrogen phosphate (Na_2HPO_4) were dissolved in 100 ml deionized water to make a buffer solution. Then 0.5 g of platinum chloride (PtCl_4) was added to the phosphate solution to make an electroplating solution. During

electroplating, an Ag/AgCl electrode was used as the reference electrode and a piece of platinum foil acted as the counter electrode. A voltage of -0.6 V was applied across the flexible PCB electrodes and reference electrode until the contact impedance reached 1 kOhm at 1 kHz (measured in saline). The electroplating of Pt Black resulted in a low contact impedance for the electrodes, as indicated by the significant flattening in the EIS curve beyond 1 kHz (Fig. 5.2).

Fabrication and Assembly of the Device

To assemble the 6-point electrode balloon catheter, miniaturized holes were first opened on a polyimide catheter (40 cm in length, Nordson Medical, NH) side wall using the sharp tip of some tweezers to enable balloon inflation. An inner supporting tube (silica, polyimide coated) was inserted inside the catheter to improve the mechanical strength (Fig. 6.6 (A)).

An inflatable balloon (9.5 mm in length, 2-10 mm diameter depending on inflation pressure, Nordson Medical, NH) was sleeved onto the distal end of the catheter and secured with biocompatible epoxy. Then the catheter was encapsulated with a heat-shrink tube (Nordson Medical, NH) to prevent any leakage from the catheter. A 27 gauge syringe tip connector was attached to the other end of the catheter for inflation using syringe pump (Fig. 6.6 (B)). After the epoxy was cured, the balloon was inflated under water to check for leakage. If any bubbles appear during inflation, more epoxy can be applied to help with sealing. Also, a pair of tantalum foils (Advanced Research Materials, UK) to act as radiopaque markers for visualization during the angiogram were secured at both ends of the balloon using a short section of heat-shrink tube (Fig. 6.6 (C)).

Finally the front end of the flexible electrodes was attached onto the balloon using a silicone adhesive while the balloon was inflated. The rest of the electrodes together with the catheter were encapsulated with another heat-shrink tube (Nordson Medical, NH) for insulating the device from outside environment (Fig. 6.6 (C)). The electrical connection to the impedance analyzer was made by soldering copper wires (26 AWG) to the exposed contact pads at the terminal end of the flexible electrodes.

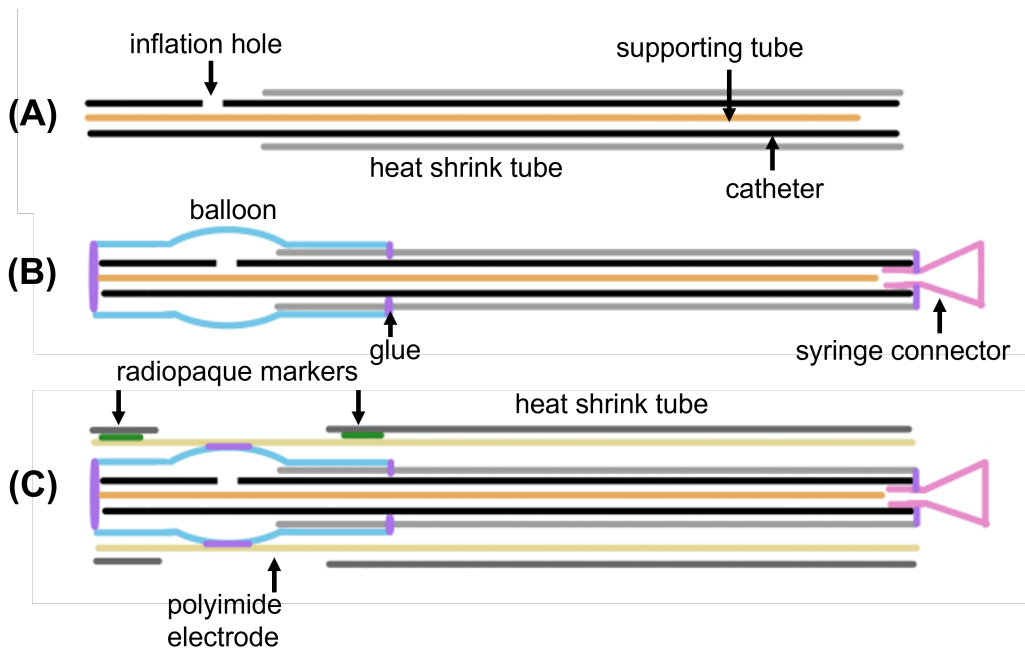


Figure 6.6: Detailed schematics of the cross section of the catheter assembling procedure. **(A)** Miniaturized holes were created using tweezers on the catheter before encapsulation with a heat shrink tube. A supporting tubing was used to increase the mechanical robustness of the catheter. **(B)** The balloon and the syringe connector were fixated at both ends of the catheter with epoxy glue. **(C)** A pair of radiopaque markers was secured using a heat shrink tube and the remainder of the catheter was encapsulated.

The above description is the basic device assembly procedure, and it can easily be adapted for a 12-point electrode setup (discussed in Chapter 7). These experiments integrated an EIS device with a FFR sensor probe, by inserting the probe into the main catheter and securing it with heat shrink tubing. As Fig. 6.7 shows, the device is placed inside the artery with the electrodes in contact with the wall to measure the impedance of the plaque. An FFR sensor was placed up-stream from the balloon to measure the pressure.

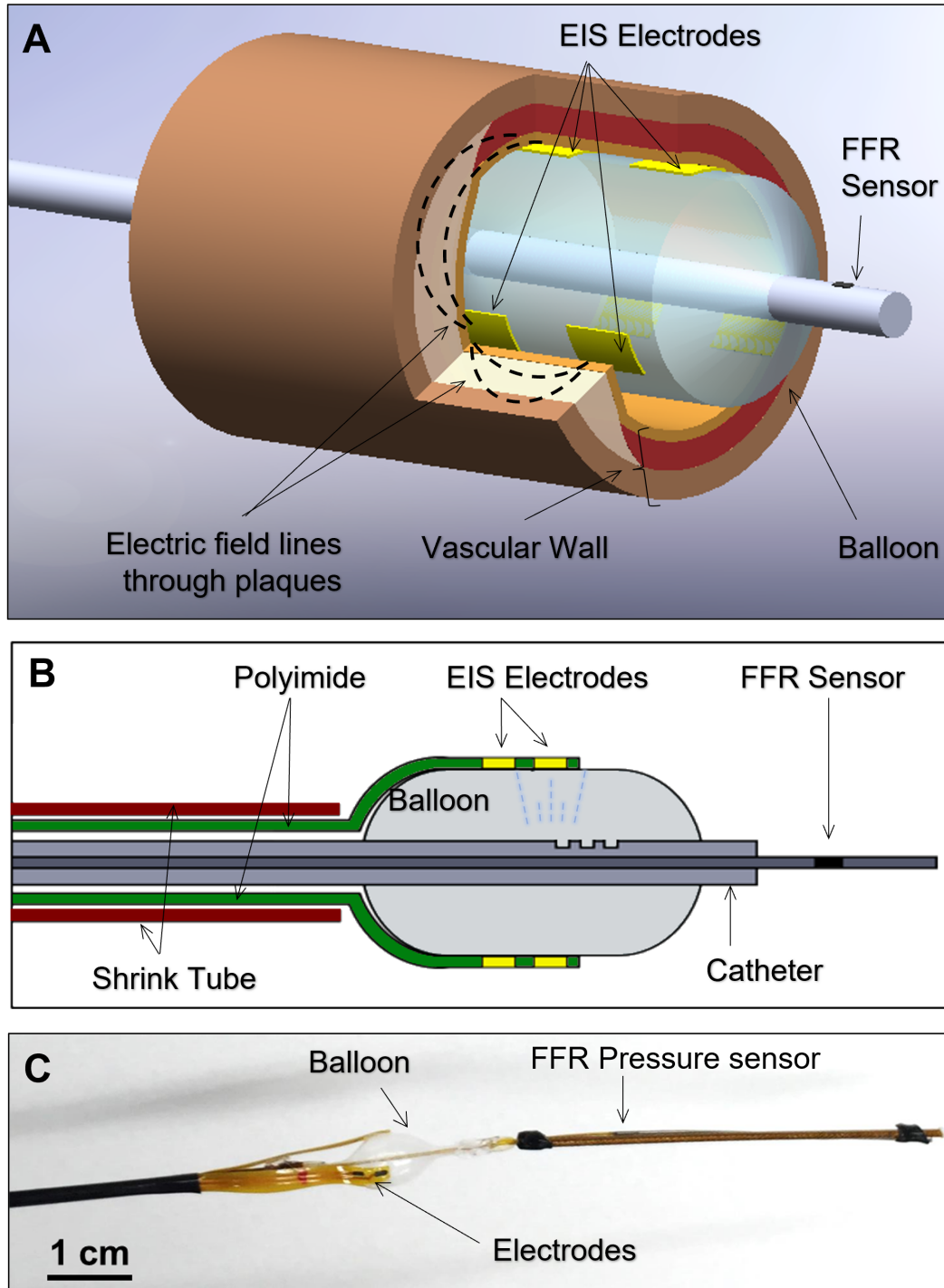


Figure 6.7: Device Schematic. (A) Schematic of the dual EIS-FFR sensor deployed in the artery. (B) Cross-sectional view of the device. (C) A photo of the dual-sensor catheter.

6.4 EIS Experiments

EIS Equipment Setup

Electrical impedance spectroscopy measurements were conducted using the Gamry system (Gamry Series G 300 potentiostat, USA) (Fig. 6.8) in which fifteen scans were performed with a 6-point electrode catheter. A peak-to-peak voltage of 50 mV was used to acquire the frequency-dependent impedance profiles ranging from 1–300 kHz. We acquired 10 data points per frequency decade.

To switch the electrode pairs for impedance measurements automatically, a multiplexer board was created (Fig. 6.8). Two 16-channel multiplexer chips were controlled by Arduino.

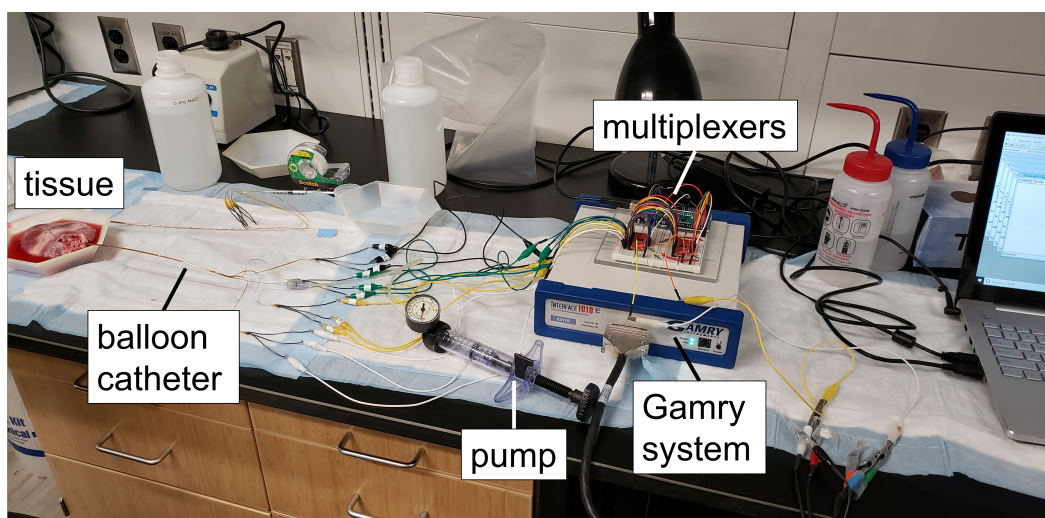


Figure 6.8: Experimental setup for the EIS measurements. The Gamry system applied voltage and recorded the impedance spectrum. A pump was used to inflate the balloon catheter.

Measurement Protocol

Before any measurement, the device must be tested in saline (0.9 w/v %) for calibration purposes. The working electrode and counter electrode from the Gamry system are connected to the electrodes using alligator clips. At least 3 tests should be done to ensure all 6 electrodes have a low contact impedance.

To run the EIS measurements, the “Gamry Instrument Framework” software option was selected with the “Potentiostatic EIS” protocol under “Experiment” tab (Fig. 6.9 (A)). The frequency range, sampling rate, AC voltage, and DC voltage can all be adjusted as needed. The frequency range we are interested in for this work is from

1-300 kHz (the maximum limit of Gamry system). The sampling rate was set to 10 points per decade and the AC voltage to 50 mV.

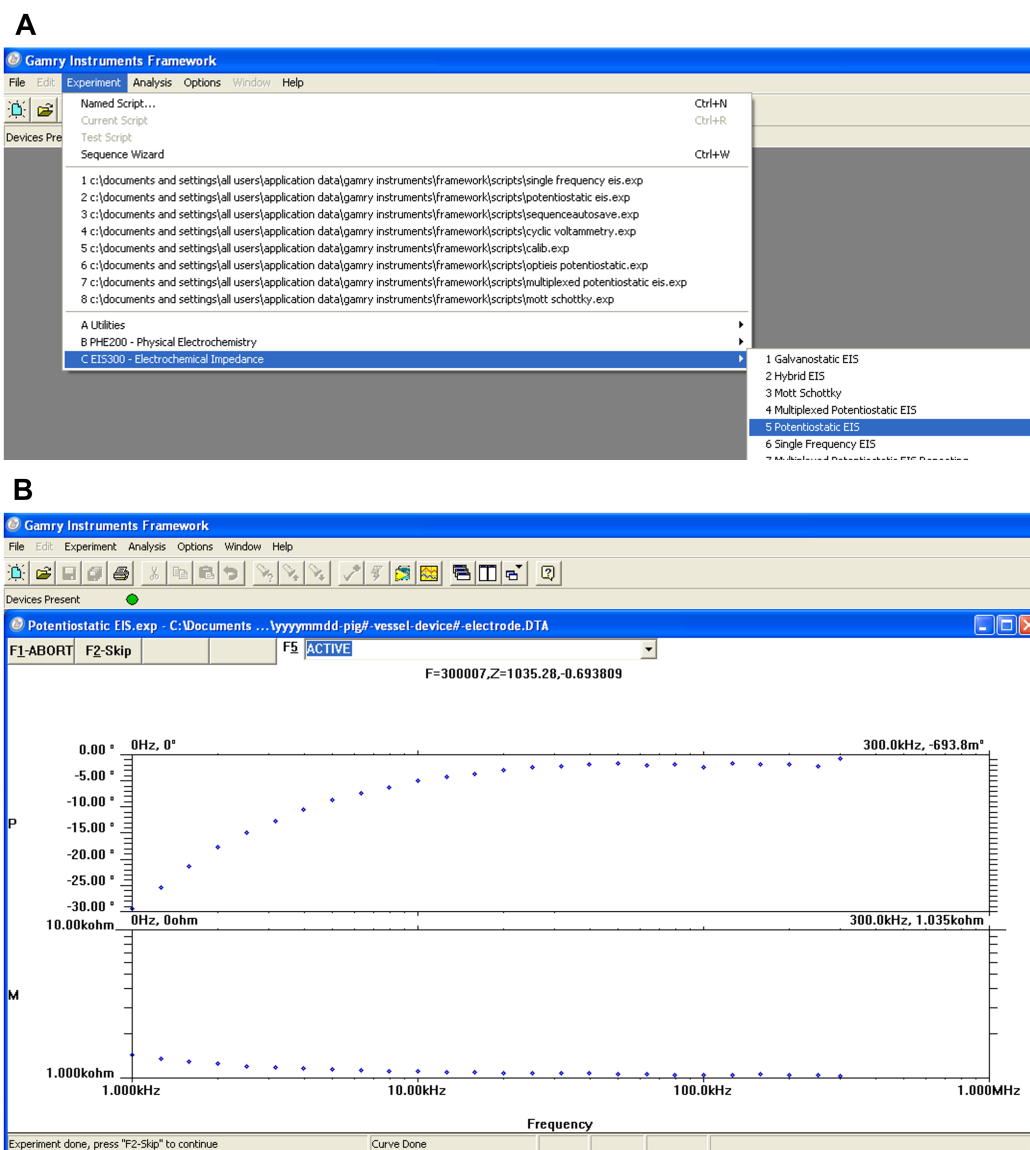


Figure 6.9: The software interface showing (A) the protocol and (B) the impedance spectrum for a good pair of Pt-black plated electrodes in saline.

The impedance magnitude for the Pt-black plated electrodes should be 1-1.3 kOhm at 1000 Hz measured in a 0.9 % saline solution (Fig. 6.9 (B)). If the impedance is high, it could be the connection or an issue with surface contamination. One should confirm the wiring is secured and use cotton swabs with acetone and IPA to gently clean the surface of the electrodes. When cleaning the electrode, one should wipe in

one direction, starting from the balloon end to the tip (do not wipe “back-and-forth” (Fig. 6.10)).

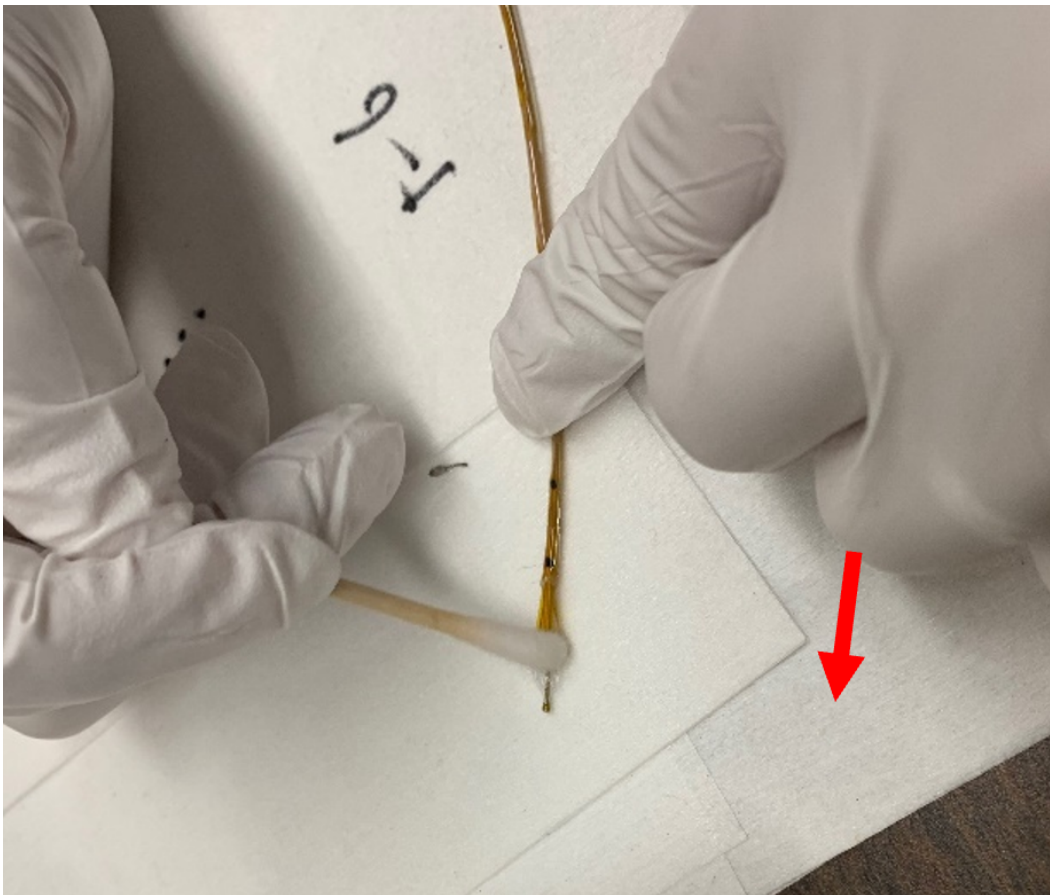


Figure 6.10: A cotton swab is used to clean the surface of the electrode from the balloon end to the tip.

After the catheter is deployed in the vessel, the balloon can be inflated using a syringe to about 14 psi, or to the desired size such that the electrodes are in contact with the wall. For the 6-point electrode device, a total of 15 measurements were completed. Reinflating of the balloon needs to be done after a few permutations to ensure a solid contact between the electrodes and the wall.

6.5 Animal Study Design

Recreation of Plaque in Swine Model

A combination of a high-fat diet and a partial carotid arterial ligation has previously been demonstrated to promote atherosclerotic plaques in swine models.[130] Yucatan miniature pigs were chosen as the model animal system for this work as the

diameter of the carotid arteries in these pigs is comparable to the human coronary arteries (3-5 mm).[131] All animals underwent partial ligation to the right carotid artery to facilitate plaque growth. The animal studies were approved by the UCLA Animal Research Committee in compliance with the institutional IACUC protocols. The surgical procedures and the postoperative care were performed by experienced veterinarians from the Division of Laboratory Animal Medicine at UCLA School of Medicine. The detailed surgical procedure is described as below.

The Yucatan miniature pigs (n = 6, 20-30 kg, S S Farms, Ranchita, CA) were fed a high-fat diet containing 4% cholesterol, 20% saturated fat, and 1.5% supplemental choline (Test Diet; Purina, St. Louis, MO) for 2 weeks before surgical ligation of the right carotid artery. The pigs were anesthetized with intramuscular tiletamine and zolazepam, isoflurane was given to maintain general anesthesia during the procedure. A 6F introducer sheath was inserted percutaneously via the Seldinger procedure into the right or left femoral artery to monitor blood pressure and to provide access for the angiography. Bupivacaine was subcutaneously injected into the ventral neck along the path of the incision site. A midline skin incision was placed at the neck. Both right and left common carotid arteries were dissected at approximately 5 cm in length, the right common carotid artery was tied off with a suture (Ethicon, Cornelia, Ga) around a spacer (approximately 1.3 mm in diameter) positioned on the external surface of the artery (Fig. 6.11 (A)). The spacer was subsequently removed, leaving a 50-70% stenosis (Fig. 6.11 (B)). Postoperative CT angiography was performed to monitor the degree of surgical stenosis (Fig. 6.11 (C)). The surgical wound was closed layer by layer to avoid manipulation of the adjacent tissues. The animals were allowed to recover after surgery and then were resumed to the high-fat diet for 16 weeks (Test Diet; Purina, St. Louis, MO). Serial aortic CT angiograms were performed to demonstrate the reduction in the diameters of the carotid arteries following iodinated contrast injection to the tail vein at the baseline, 8 weeks and 16 weeks.

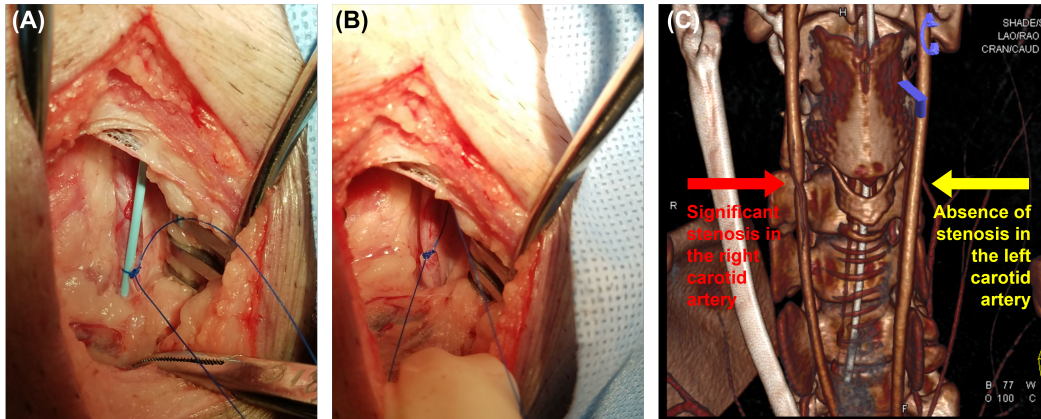


Figure 6.11: Partial ligation of the carotid artery. (A) A midline skin incision was placed at the neck and then the right common carotid artery was dissected and tied off along with a spacer, (B). The spacer was removed to create a 50-70% stenosis, (C) 3D image of the anatomy demonstrates the presence of stenosis in the right common carotid artery and the absence of stenosis in the left common carotid artery.

Stenosis after Ligation

Over the 16 weeks of the high fat diet, all animals were monitored via CT imaging for the progression of carotid stenosis. Baseline diameter measurements of the stenosed right carotid artery demonstrated atherosclerotic formation as compared to the left carotid artery (0 weeks, midpoint 8 weeks, and endpoint 16 weeks). At baseline, the diameters of the left and right carotid arteries were similar (Fig. 6.12 (A)). After 16 weeks, the average internal diameters in the stenosed right carotids were reduced by 33% (from 4.5 mm to 3 mm), whereas the diameter of left (control) carotid arteries increased from 4.6 mm to 5.0 mm, likely due to a compensatory response to the decreased flow in the right (Fig. 6.12 (B)). There was no significant difference between the diameter of the left and right carotid arteries at baseline ($p > 0.05$, $n=6$), but a significant difference was found at intermediate and terminal time points ($p < 0.05$, $n=6$) (Fig. 6.12 (C)).

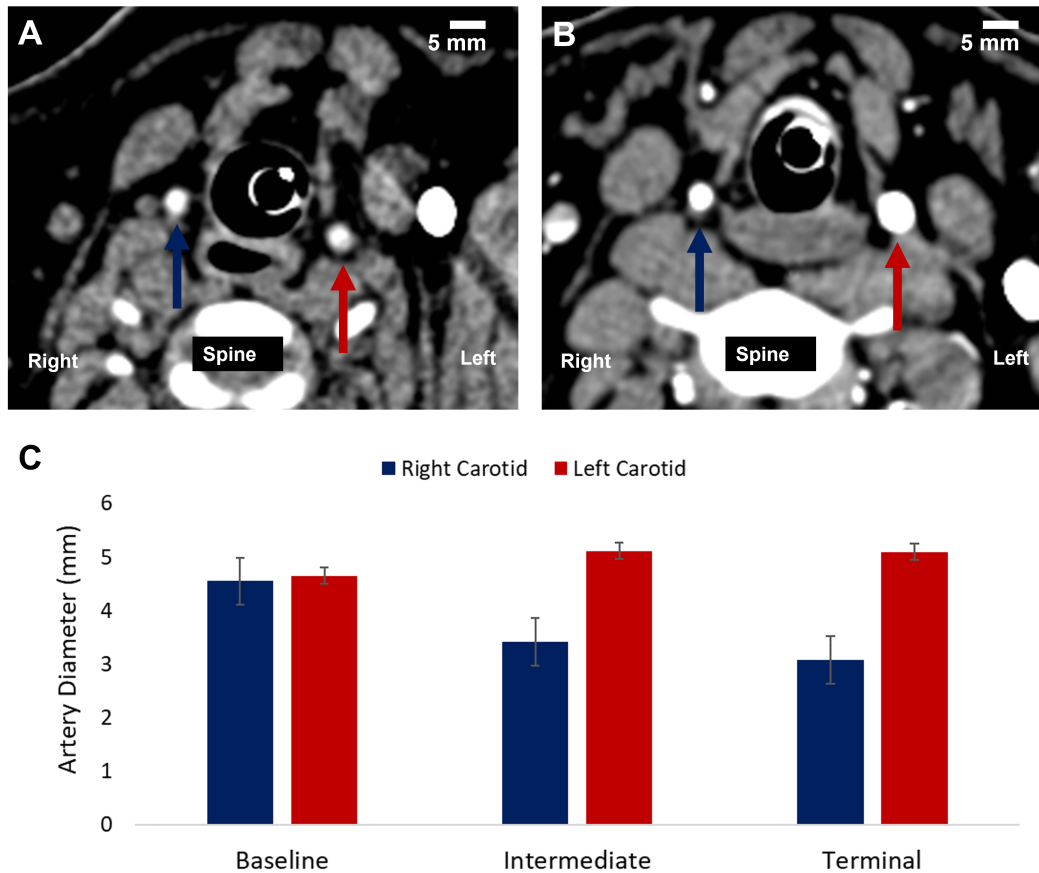


Figure 6.12: Carotid artery stenosis. ((A)) Baseline and ((B)) terminal axial CT of left (red arrow) and right (blue arrow) carotid arteries. ((C)) Comparison of the mean carotid artery diameters at 0 weeks (baseline), 8 weeks post-surgery (intermediate), and 16 weeks post-surgery (terminal).

Deployment of the EIS Catheter

The EIS measurements were conducted on the animals after the 16 weeks of the high fat diet. To deploy the balloon catheter for EIS measurements, the animals were anesthetized as described above. Bupivacaine was subcutaneously injected in the ventral neck along the path of the incision site. A midline skin incision was placed at the neck. The common carotid arteries were dissected and a surgical cut-down was performed to directly introduce the sheath and device into the carotid artery at the site of stenosis in the right carotid artery, and at the approximate mirror location in the left carotid artery. The 6-point electrode array was advanced to the level of the stenosis in the right carotid arteries, along with the radiopaque markers under fluoroscopic guidance (Siemens Artis Zeego with robotic arm), and iodinated contrast dye was injected into the vessel for visualization of the EIS sensor.

A mechanical pump was used to inflate the balloon to a constant pressure of ~14 psi so the electrodes were in contact with the endoluminal surface. Following the EIS measurements of the right (lipid-laden) vs. left (control) arteries, the catheter was removed, and the pigs were euthanized with an overdose of pentobarbital and phenytoin. Bilateral carotid arteries were collected for histology and immunostaining for lipid (oxLDL), collagen, and smooth muscle cells in the arterial walls.

6.6 Histology and Immunostaining

The carotid arteries with stenosis were dissected into segments of 10 mm in length. The samples were fixed in 10% formalin, dehydrated and embedded in paraffin. Transverse sections were collected from the center with 5 slices on each side at 0.4 mm apart. A total of 11 slices were sectioned and each slice was further sectioned into thinner sections at 5 μm in thickness for: (1) Movat staining of the connective tissue; including elastic fibers (black), collagen and reticular fibers (yellow), fibrin (bright red), and muscle (red); (2) Picrosirius Red staining to visualize collagen type I and III fibers (bright red); and (3) E06 immunostaining for oxLDL-laden lesions (brown) with hematoxylin counterstain (purple) (CV Path Institute, Inc. Gaithersburg, MD, USA).

As shown in Fig. 6.13, there is no oxLDL found in the left carotid (LCA) and the lumen size is relatively uniform throughout the specimen. On the other hand, both the right carotid #1 and #2 (RCA1, RCA2) have a positive E06 staining, indicating the existence of oxLDL. In RCA1, the semi-circumferential oxLDL is only distributed downstream of the specimen (Fig. 6.14). For RCA2, the oxLDL is located in the upper right quadrant of the carotid circumference and is less prominent compared with to RCA1 (Fig. 6.15).

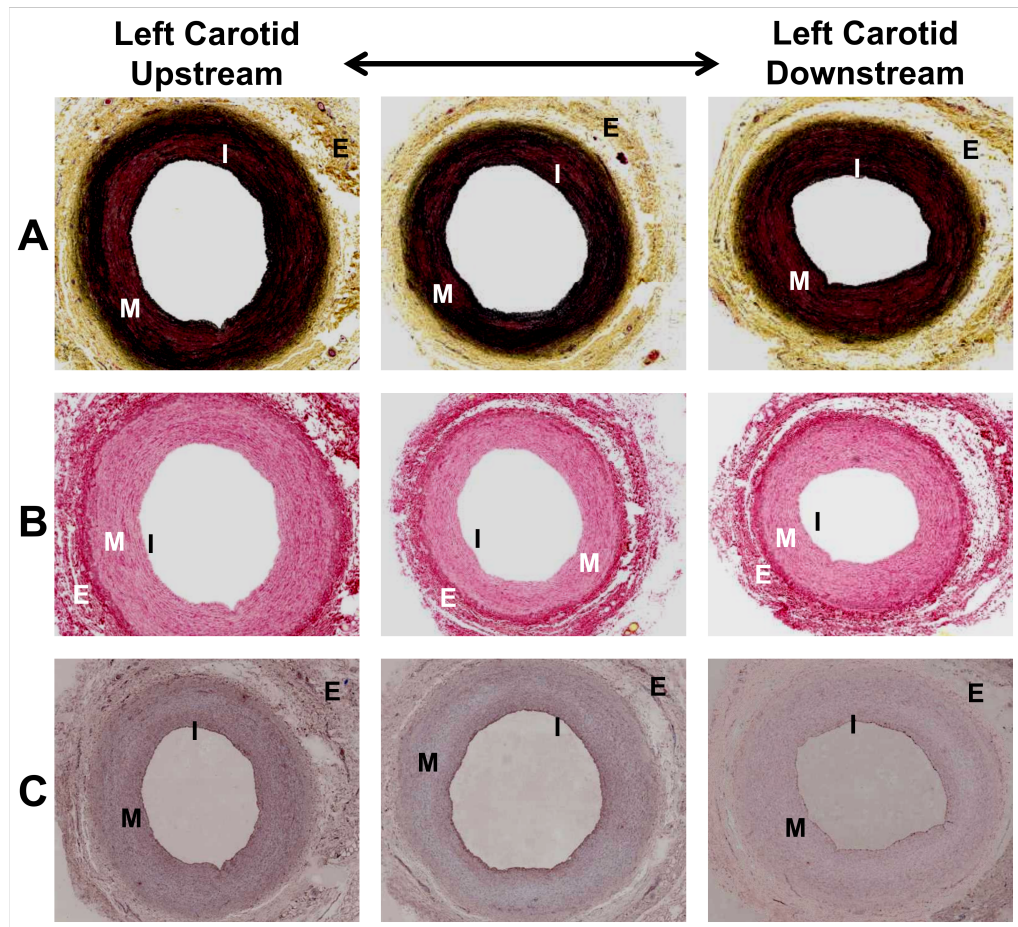


Figure 6.13: Cross-section of the left carotid artery (control) at upstream, middle, and downstream of the vessel with (A) Movat staining for the connective tissue, (B) Picrosirius Red staining for collagen type I and III fibers, (C) E06 immunostaining for oxidized-LDL. I: tunica intima; M: tunica media; E: tunica externa.

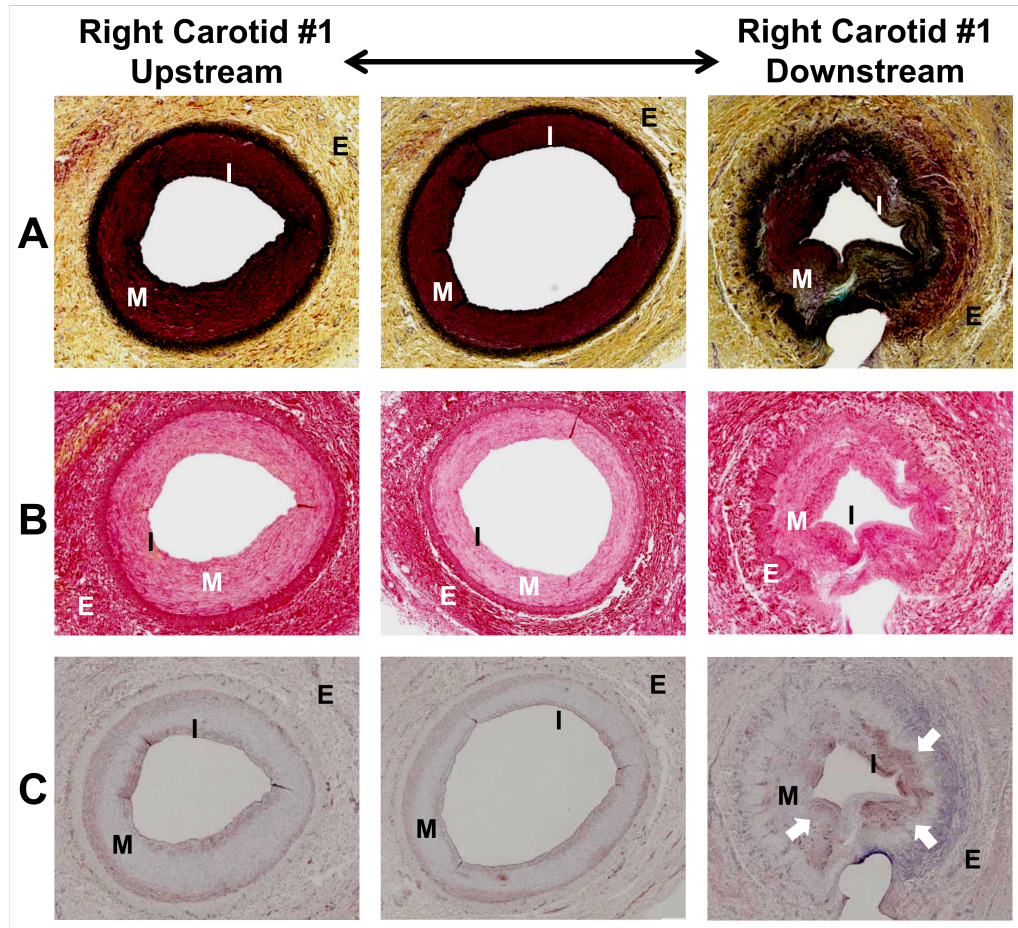


Figure 6.14: Cross-section of the right carotid artery #1 (RCA1) at upstream, middle and downstream of the vessel with (A) Movat staining for the connective tissue, (B) Picrosirius Red staining for collagen type I and III fibers, (C) E06 immunostaining for oxidized-LDL. I: tunica intima; M: tunica media; E: tunica externa.

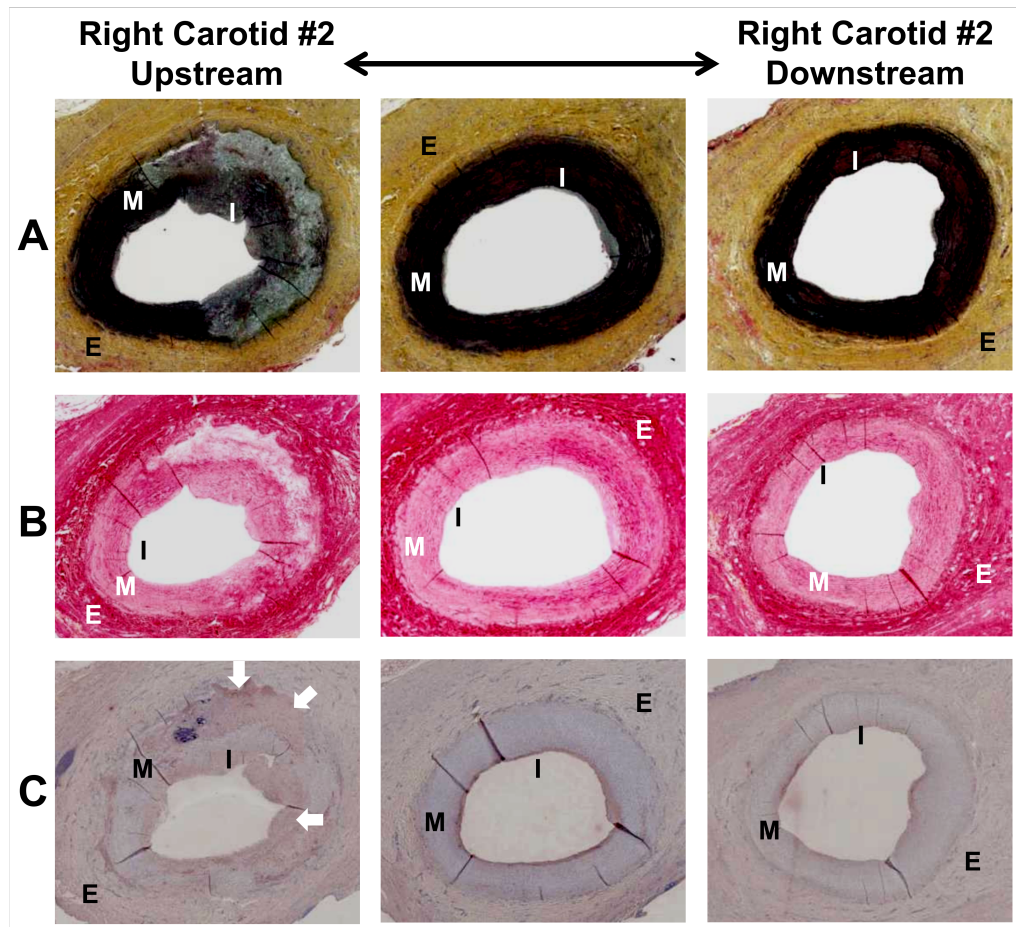


Figure 6.15: Cross-section of the right carotid artery #2 (RCA2) at upstream, middle and downstream of the vessel with (A) Movat staining for the connective tissue, (B) Picrosirius Red staining for collagen type I and III fibers, (C) E06 immunostaining for oxidized-LDL. I: tunica intima; M: tunica media; E: tunica externa.

6.7 EIS-derived Electrical Conductivity Maps

EIS Profiles

Using the 6-electrode array, we performed EIS measurements between every pair of electrodes (15 permutations) including 3 permutations to link the vertically aligned electrodes, 6 permutations to link the circumferentially paired, and 6 permutations to link the diagonally paired electrodes (Fig. 5.6). The frequency of the AC current was from 1-300 kHz and the sampling rate was 10 points per decade. This resulted in 26 data points within the entire frequency range.

We measured baseline EIS profiles in the carotid arteries prior to balloon inflation (Fig. 6.16, black series). The EIS impedance profiles of both RCA1 and RCA2 were consistently higher than those of LCA following balloon inflation (Fig. 6.16, colored

series). This result is not a surprise as there is more low conductivity oxLDL found in both RCA1 and RCA2. Note that the spectra of RCA1 has a broader range in terms of impedance magnitude, which is supported by the more prominent oxLDL distribution found in the histology.

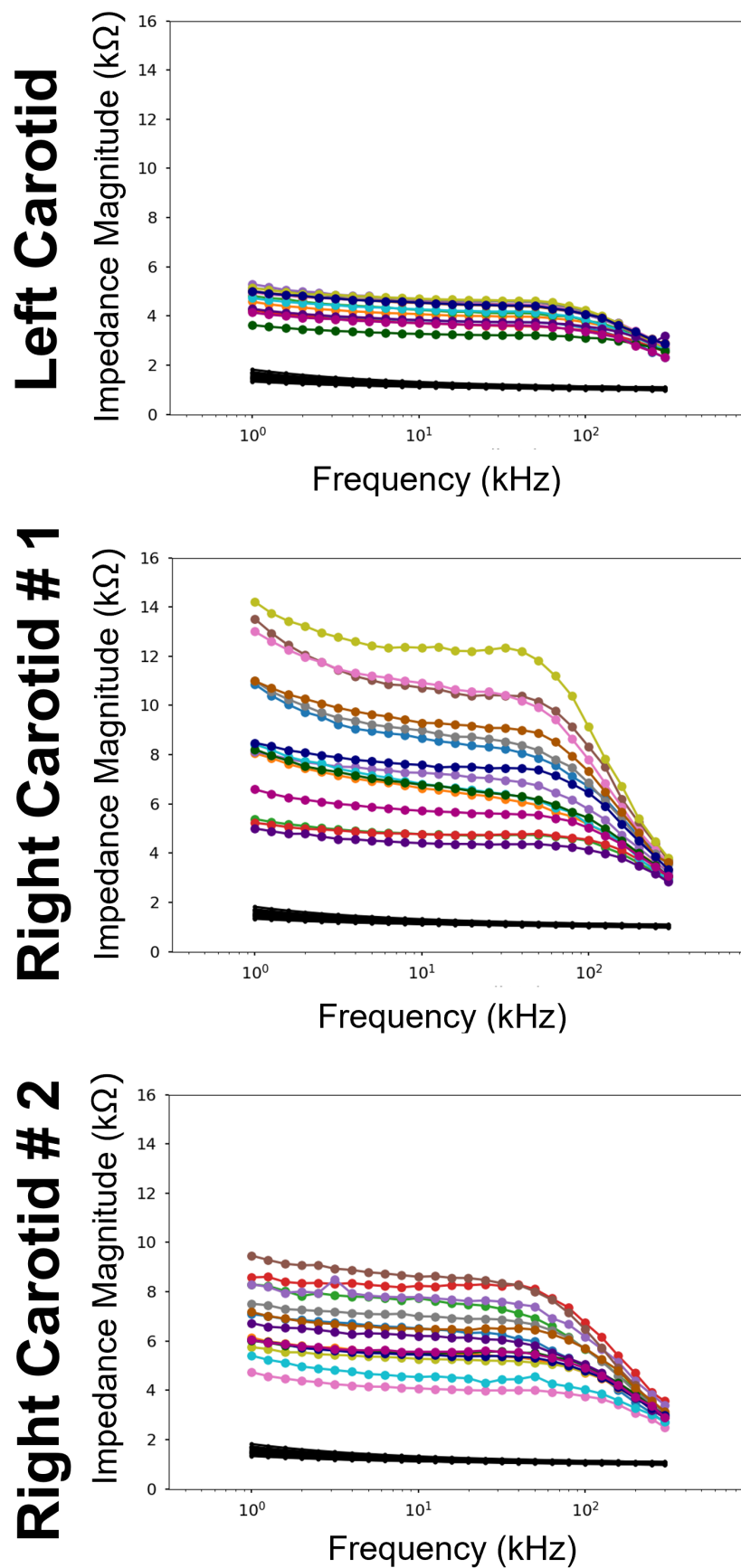


Figure 6.16: EIS profiles from 1-300 kHz were compared between the LCA (control) and RCA1 and RCA2.

EIS-derived EIT Maps

Next, we reconstructed the EIS-derived EIT mappings with the 15 impedance values at 10 kHz for the individual carotid arteries (Fig. 6.17). We observed a correlation between the EIS-derived EIT mapping and histology, as supported by the Movat stain for tissue composition, and E06 for oxLDL.

The conductivity mapping of the LCA (control) shows a yellow to orange color-coded gradient (Fig. 6.17, top), indicating the absence of oxLDL (Fig. 6.13), whereas in RCA1, the dark brown color-coded gradients (Fig. 6.17, middle) aligned with the prominent semi-circumferential E06 staining (Fig. 6.14, downstream). In RCA2, the dark brown gradients (Fig. 6.17, bottom) correspond to the presence of E06 staining in the right upper quadrant of the carotid circumference (Fig. 6.15, upstream). Thus, 3D EIS-derived EIT demonstrated an endoluminal mapping of metabolically active arteries.

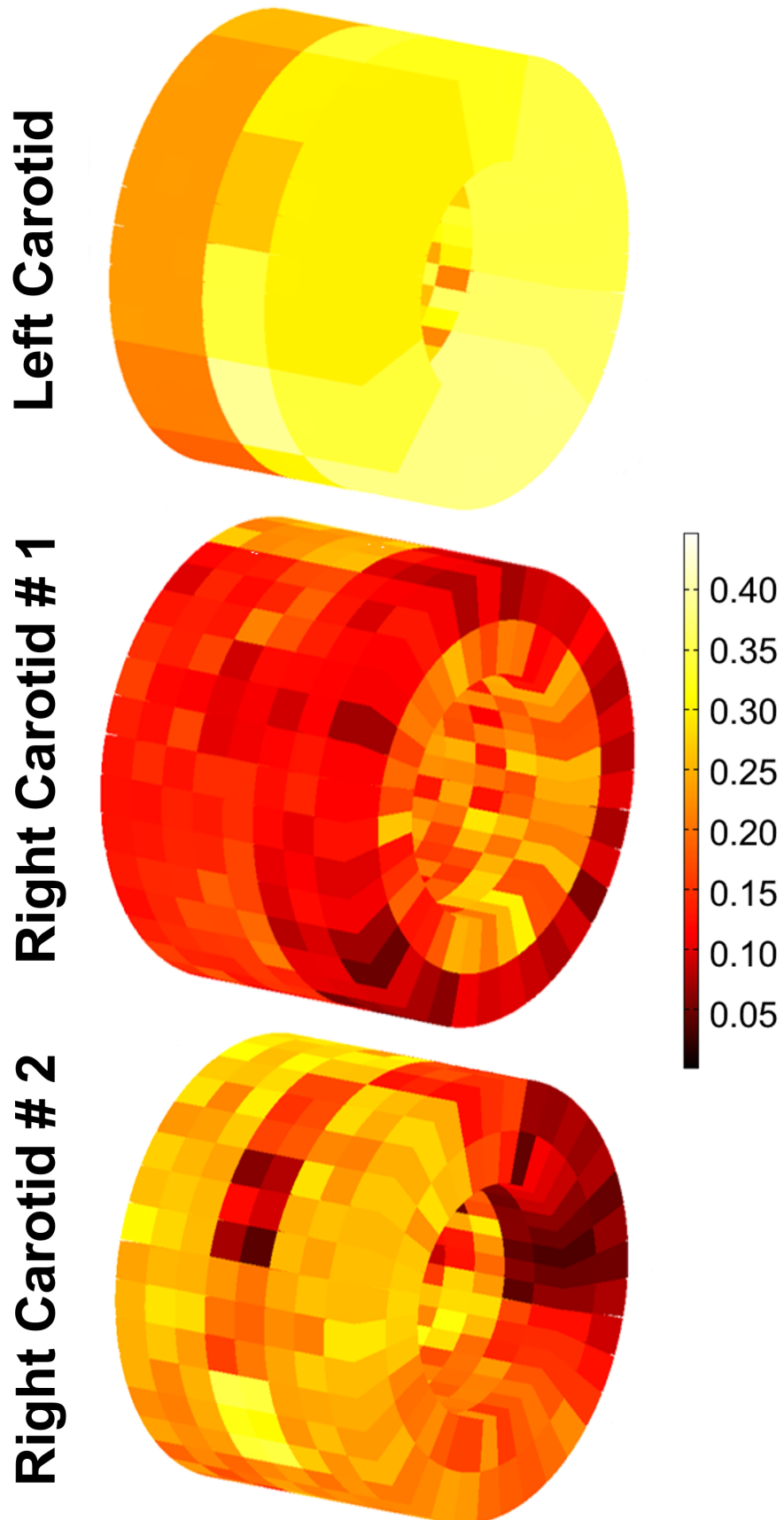


Figure 6.17: 3D EIS-derived conductivity mappings of the LCA and two RCAs (RCA1 and RCA2). The tunica intima and tunica media were constructed from the impedance magnitude at 10 kHz.

6.8 Reconstruction of Histology-based Modeling

Reconstruction Model

Based on the histology images, we reconstructed a 3D endoluminal model in COMSOL Multiphysics to simulate the impedance of each pair of electrodes to validate our *in vivo* EIS measurements.

As illustrated by the Movat staining, individual slices from the carotid arteries were divided into 3 regions: lumen, inner, and outer arterial wall. A histochemistry analysis showed that the outer wall was comprised of collagen (yellow), the inner wall was mostly smooth muscle cells (red), and a segment of the inner wall was positive for oxLDL (white) in the RCAs. The 2D outline of each layer was first extruded from the histological slices in AutoCAD and stacked to reconstruct a 3D model with the center aligned with the geometric center of the lumen. While the lumen was deformed by the inflated balloon (~ 1 cm long) during the EIS measurements, we approximated the lumen as a uniform circle for all cross-sections. The lumen circumference was then estimated using the average circumference of each slice (Fig. 6.18).

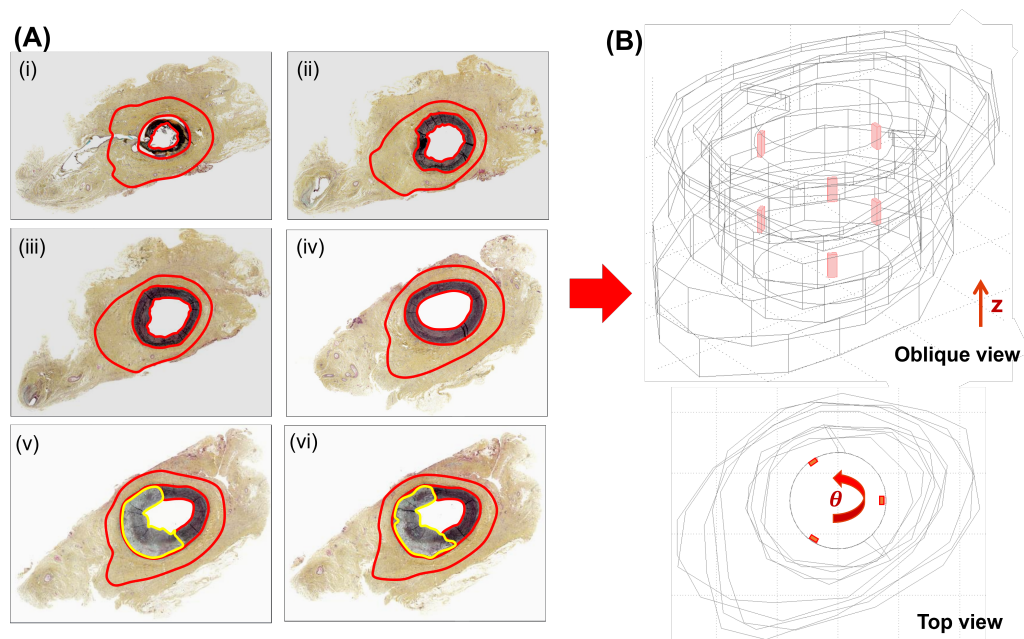


Figure 6.18: Finite Element Model for the impedance modeling. **(A)** Representative histological cross-sections from the right carotid artery were demarcated by the Movat staining for connective tissue, the boundaries for collagen, smooth muscle, and the lipid component. **(B)** These demarcations from the histological slices allowed for reconstruction of a 3D model. The positions of the electrodes (red) were defined by the z and θ coordinates.

In the absence of any *a priori* knowledge of the precise position of the electrodes relative to each artery, we scanned a wide range of electrode positions to optimally reproduce the measured EIS values. The electrode positions in the cylindrical coordinates corresponded to the distance between the edge of the electrodes $z = 0$, z , and the rotational angle, θ . We used 3 different z values (0, 0.7, and 1.4) and 12 different θ values (-150° , -120° ,, 0° , 30° ,, 150° and 180°) to generate 36 possible electrode positions for each arterial model, see Fig. 6.19.

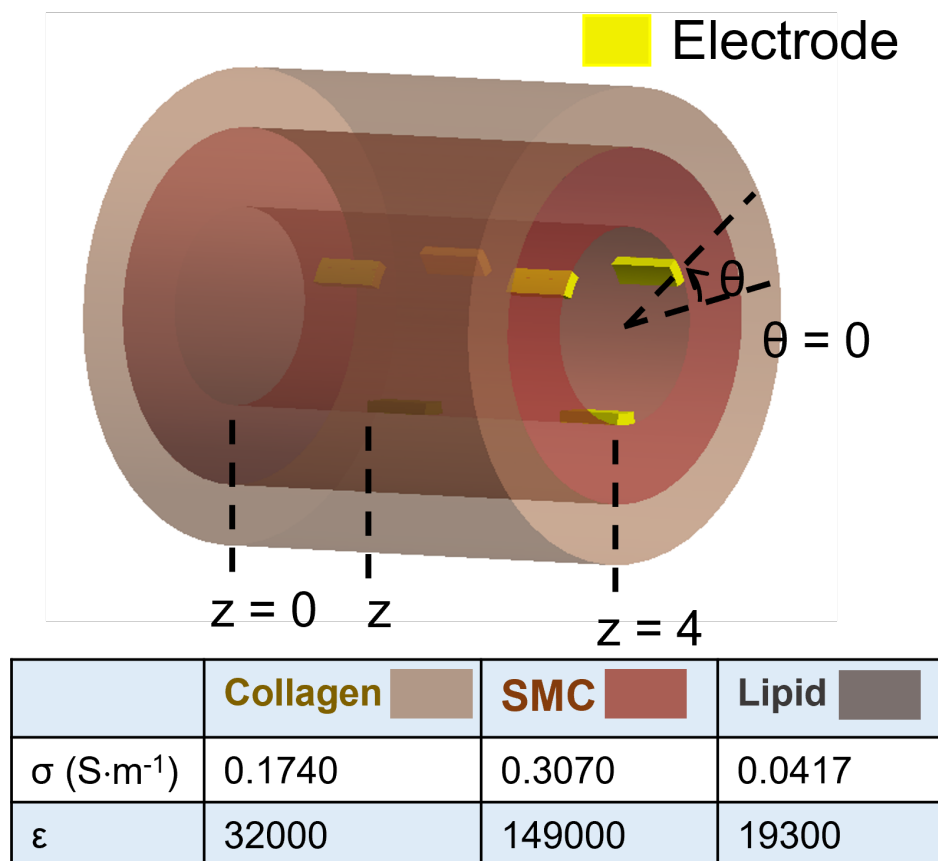


Figure 6.19: Electrode Position Definition. The position of the electrodes in the 3D model is defined by the polar coordinates, where z is the distance between the edge of the electrodes and $z = 0$, and θ is the angle between the midpoint of the first pair of electrodes and $\theta = 0$.

The computational EIS model was governed by the Time-Harmonic Maxwell equation. Assuming a negligible contribution from the magnetic field [68], we arrived at the following expression:

$$-\nabla \cdot \{(\sigma + j\omega\epsilon_0\epsilon_r)\nabla V\} = 0. \quad (6.1)$$

For each combination of z and θ , 15 impedance values were solved numerically by using the COMSOL AC/DC module in conjunction with the assigned material properties; namely, conductivity (σ) and permittivity (ε) for the collagen, lipid, and smooth muscle (Table. 6.1).

Tissue	σ (S/m)	ε
Collagen	0.174	32000
Smooth muscle cell	0.307	149000
Fatty tissue	0.042	193000

Table 6.1: Tissue properties used for the computational model.[91]

We reconstructed the individual arterial models from the histology, and compared the computational impedance with experimental impedance at 10 kHz to identify the possible electrode position during the experiments. We adopted the following mathematical criteria for the identification of the closest alignment: the impedance values for the 15 permutations from the experiments were sorted in the following order: $Z_{\text{exp}, 12}, Z_{\text{exp}, 13}, \dots, Z_{\text{exp}, 23}, \dots, Z_{\text{exp}, 34}, \dots, Z_{\text{exp}, 56}$. For each permutation in the corresponding simulation results, the impedance values were arranged analogously: $Z_{\text{sim}, 12}, Z_{\text{sim}, 13}, \dots, Z_{\text{sim}, 23}, \dots, Z_{\text{sim}, 34}, \dots, Z_{\text{sim}, 56}$. Next, we calculated the summation of the square of the differences between the experimental and simulated EIS as follows:

$$\Sigma = \sum_{i,j=1,i \neq j}^{15} (Z_{\text{exp}, ij} - Z_{\text{sim}, ij})^2. \quad (6.2)$$

Then we defined the deviation as the square root of the summation as follows:

$$\text{Deviation} = \sqrt{\Sigma}. \quad (6.3)$$

Simulation Results

First, using each electrode position (z, θ) and each artery, we calculated the deviation. The electrode position resulting in the largest reciprocal of the deviation (the square root of the summation) is defined as the best fit scenario. The best fit electrode positions were then illustrated in the 3D deviation plots (Fig. 6.20). A total of 36 electrode placements were tested in the simulation models for **(A)** LCA, **(B)** RCA1, **(C)** RCA2 position A, and **(D)** RCA2 position B. The best fit for the electrode positions is highlighted with the green circle. Note, for the right carotid #2 we did the EIS measurements at 2 different positions: A and B. The best fit electrode positions for those two cases were different in both z and θ .

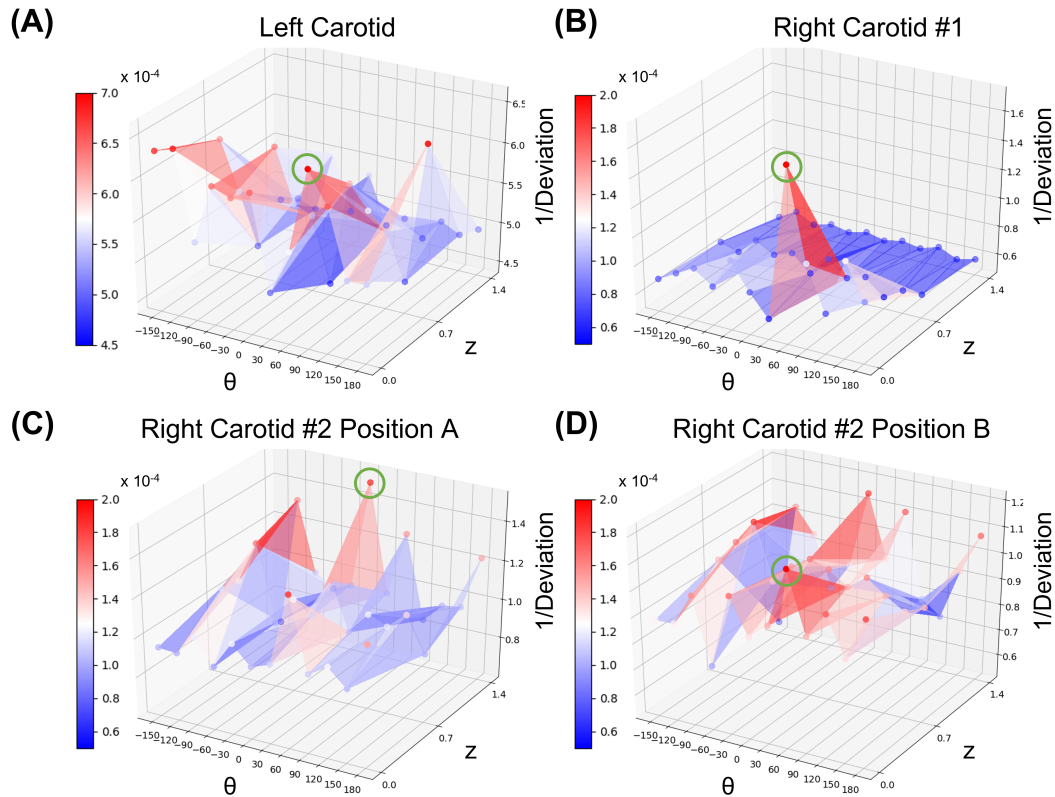


Figure 6.20: Deviation plots for (A) LCA, (B) RCA1, (C) RCA2 position A, and (D) RCA2 position B.

Scatter plots of the 15 impedance values from the measured EIS and representative computation model are presented with the best fit combination of z and θ as highlighted in light blue (Fig. 6.21). A simplified 3D schematic shows the position of the electrodes in the endolumen for the best fit scenario. An experimental impedance at 10 kHz is plotted alongside the modeling results at the given z and θ values.

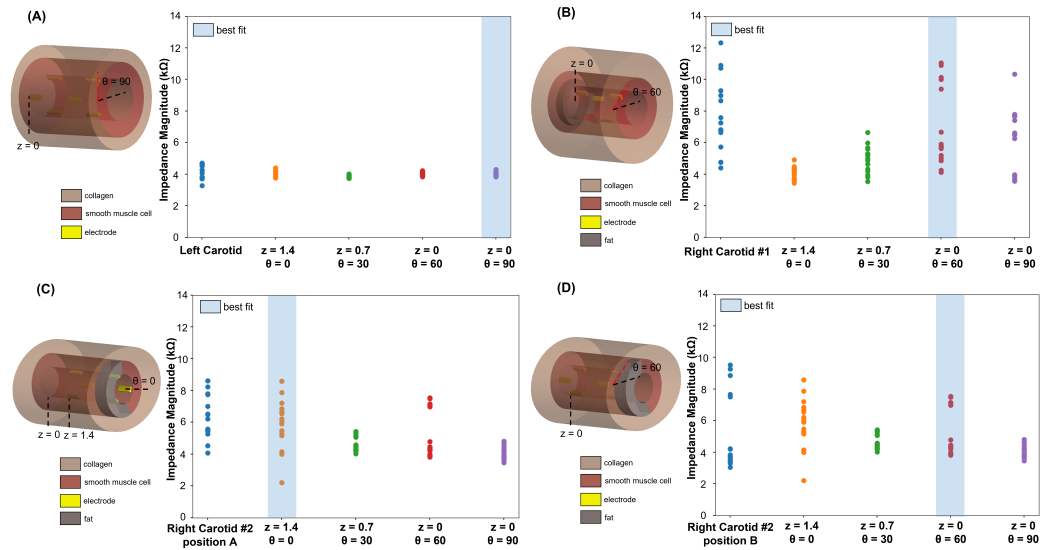


Figure 6.21: Computational EIS resulting from four different electrode positions are compared with the experimental EIS for (A) LCA, (B) RCA1, (C) RCA2 position A, and (D) RCA2 position B.

The simulation values were in agreement with the low impedance values in LCA as compared to both RCA1 and RCA2. In LCA, the changes in the electrode positions and rotations imparted no significant shift to the EIS profiles. This is because the vessel wall was uniform. The model also predicted the distributions of impedance measurements in RCA1 and RCA2. The different electrode positions in relation to the oxLDL-laden lumen engendered a distinct distribution of EIS profiles between RCA2-A and RCA2-B. In the presence of different electrode positions to the lipid-laden lumens, RCA2-B data revealed two distinct regions with broader impedance spectra as compared to RCA2-A data. By simulating these changes, we identified two combinations of z and θ values for reconstructing the impedance distributions that overlapped with the EIS measurements from RCA2-A and RCA2-B, respectively.

The 15 measured EIS profiles were also plotted with the simulation impedance at 10 kHz when electrodes were at the best fit scenario for (A) LCA, (B) RCA1, (C) RCA2 position A, and (D) RCA2 position B (Fig. 6.22).

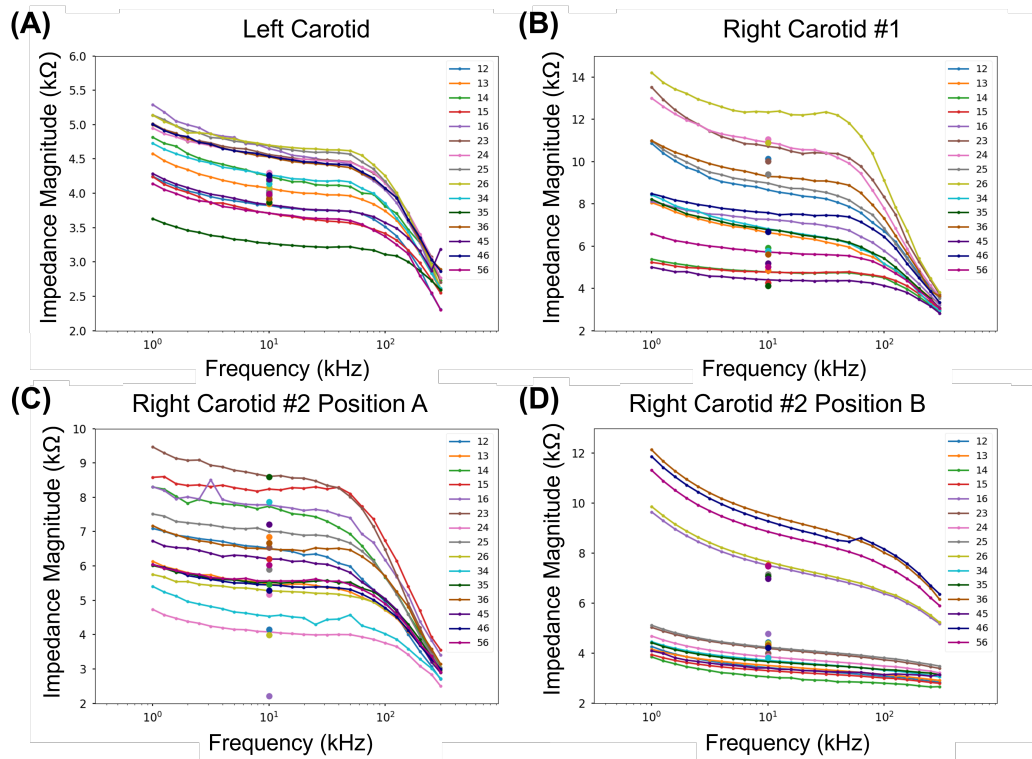


Figure 6.22: EIS profiles and simulation result comparison for (A) LCA, (B) RCA1, (C) RCA2 position A, and (D) RCA2 position B.

6.9 Discussion

Our investigation on EIS-derived EIT mapping introduces a transition from 2D intravascular spectroscopy to 3D tomography. This pre-clinical model of atherosclerosis recapitulated the oxidized lipid-laden endolumen for EIT mapping in the Yucatan mini-pigs that are reported to develop distal atheroembolism.[130] The 3D histology-derived computational model simulated impedance distributions to validate the measured EIS profiles. Overall, EIT mapping for *in vivo* detection of lipid-rich endolumen may be an efficient strategy to predict metabolically active, albeit for angiographically non-obstructive lesions prone to distal rupture.

Notably, our EIS-derived EIT algorithm directly solved the forward problem by obviating the inverse ill-posed problem encountered by other EIT algorithms.[68], [132] We used the “genetic algorithm” to optimize the conductivity distributions that were closely overlapping with the Movat staining for connective tissue and E06 staining for oxLDL, as represented by the color-coded gradients of 3D mapping. However, effective reconstruction of the 3D EIS-derived EIT is dependent on the number of electrodes. The current 6-electrode configuration could be expanded to

12 electrodes to enhance the spatial resolution. While increasing the number of electrodes would require additional computation for tomographic reconstruction, our current methodology provides a foundation for this work.

Our histological segmentation and 3D reconstruction of the carotid arteries also allowed for the creation of a computational model to validate the measured EIS profiles. Electrical impedance values are governed by the distinct tissue composition and precise boundary conditions of the organ system, and insufficient knowledge of arterial wall composition and topography may cause the computational modeling to deviate from experimental measurements. For this reason, we obtained multi-slice and axial histology to establish a 3D arterial computational model with well-defined layers of tissue properties (σ = tissue conductivity and ε = permittivity), including collagen, fatty tissue, and smooth muscle.

6.10 Summary

In conclusion, we have demonstrated the deployment and implementation of a balloon catheter with a multi-electrode configuration for 3D EIS measurements. Our acquired electrical impedance tomography of the artery is consistent with the histology in the pre-clinical model of atherosclerosis, supporting the detection of oxidized LDL-laden plaques with high-risk features for plaque rupture. Future studies will aim to calibrate the EIT gradients with the extent of lipid core for advancing our clinical understanding of the vulnerable plaque with translational implications in interventions aimed at plaque modification.

12-POINT EIS FOR ATHEROSCLEROSIS DETECTION

Previously, we have demonstrated a new method, EIS-derived EIT, and its application to plaque detection. In this chapter, we discuss atherosclerosis detection using an improved balloon catheter device with more electrodes. The EIS-derived EIT algorithm is modified and applied to reconstruct the conductivity map.

While our 6-point EIS device has demonstrated the capability of detecting plaque in swine models, we would like to increase the number of electrodes to improve the conductivity reconstruction. A 12-point electrode array and device assembly will be discussed and the preliminary reconstruction results of a vessel using this device will be presented.

7.1 12-point Device

Flexible polyimide electrodes (FPCexpress, Ontario, CA) were used for the EIS measurements; the electrodes layout is shown in Fig. 7.1. The electrode array was composed of 12 electrodes with a width of $200\ \mu\text{m}$ and a length of $600\ \mu\text{m}$, with a separation between the two rows of 1 mm. Unlike the 6-point electrode layout where every 2 electrodes are considered as a set on the same strip, the 12-point electrodes are all on the same piece of flexible polyimide PCB with laser cut slits to separate the 2-electrode groups.

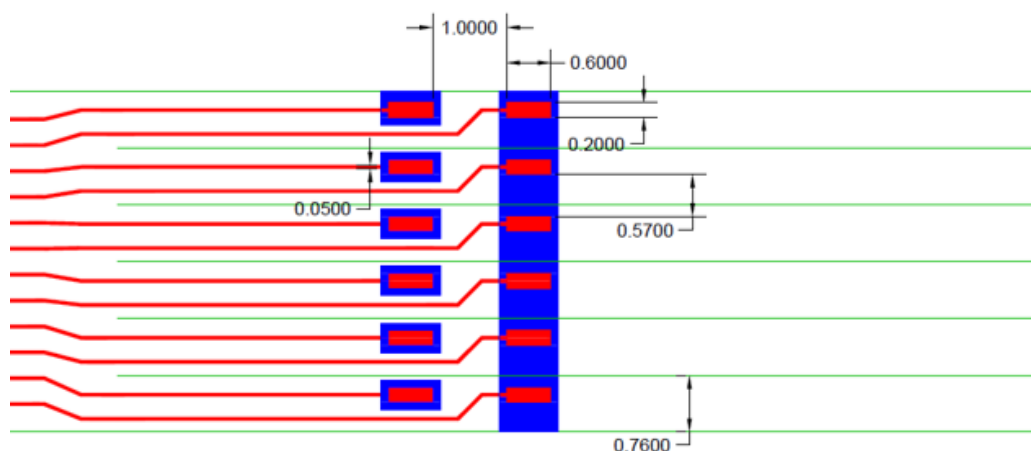


Figure 7.1: Polyimide PCB layout for 12-point EIS. Unit: mm.

The assembly of the 12-point electrode balloon catheter is similar to the procedure used for the 6-point device. Miniaturized holes were first created on a polyimide catheter side wall using the sharp tip of a tweezer to enable balloon inflation. An inner supporting tube was inserted inside the catheter to improve the mechanical strength.

An inflatable balloon was sleeved onto the distal end of the catheter and secured with biocompatible epoxy. Then, the catheter was encapsulated with a heat-shrink tube (Nordson Medical, NH) to prevent leaking. A catheter with a larger inner diameter was sleeved onto the balloon catheter to create more space for wrapping the flexible PCB, and was then fixed using epoxy. The syringe tip connector and a pair of tantalum foils were assembled as described previously.

To assemble the flexible electrodes on the balloon catheter, the PCB was rolled up and threaded through a section of heat shrink tube, then sleeved onto the catheter. After heating up, the heat shrink tube can secure the flexible electrodes onto the catheter (Fig. 7.2). Then, silicone adhesive was used to attach the electrodes to the balloon. The exposed contact pads at the terminal end of the flexible electrodes were connected to the impedance analyzer by zero insertion force (ZIF) connectors.



Figure 7.2: The 12-point electrode balloon catheter.

7.2 EIS Measurement Procedure

Electrical impedance spectroscopy measurements were conducted using the Gamry system (Gamry Series G 300 potentiostat, USA) in which 66 scans were performed. Multiplexers previously mentioned in Chapter 6 were again used to automatically switch the electrode pair connected to the Gamry system. The measurement procedure was equivalent to the 6-point EIS device procedure.

7.3 Preliminary Reconstruction Result

The 12-points EIS balloon catheters were deployed in 6 pigs for *in vivo* EIS measurements. The animal study was designed following the same procedure described in Chapter 6. All 6 pigs underwent right carotid arteries ligation with 16 weeks of a high fat diet. A histology analysis is currently underway for the carotid arteries.

Due to the limited time during the EIS measurement procedure, the number of scanning electrode permutations was reduced to 30. The 30 permutations are shown in Fig. 7.3. One of the main challenge for EIS measurements is the electrode-tissue contact requirement. To achieve good contact, the balloon must be inflated, resulting in occlusion of the vessel wall. Downstream ischemia and the rupture of vulnerable plaque could be a serious consequence of this requirement. Shortening the measurement time would help address the issue of ischemia. Deflation and reinflation of the balloon during the measurements could also reduce the risk of ischemia. However, the muscle in swine models is very prone to spasms with frequent mechanical stimulation.

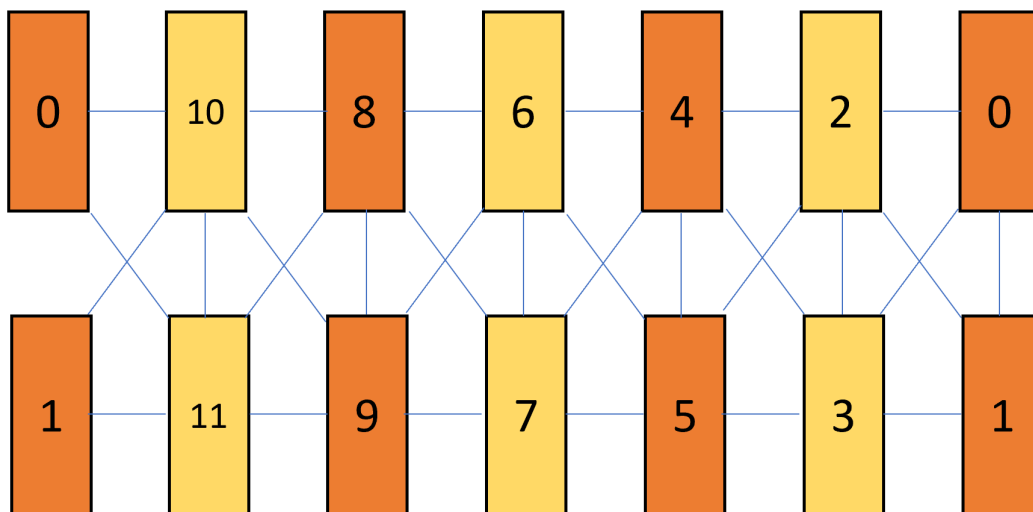


Figure 7.3: Schematic of the electrode arrays and the 30 permutations.

The EIS profiles for the 30 permutations measured from one of the animal right carotid arteries is shown in Fig. 7.4. The impedance magnitudes range from 2.5 kOhm to 4 kOhm, indicating very little or no fatty tissue contained in the vessel wall. However, this statement remains to be validated through histology staining of the E06.

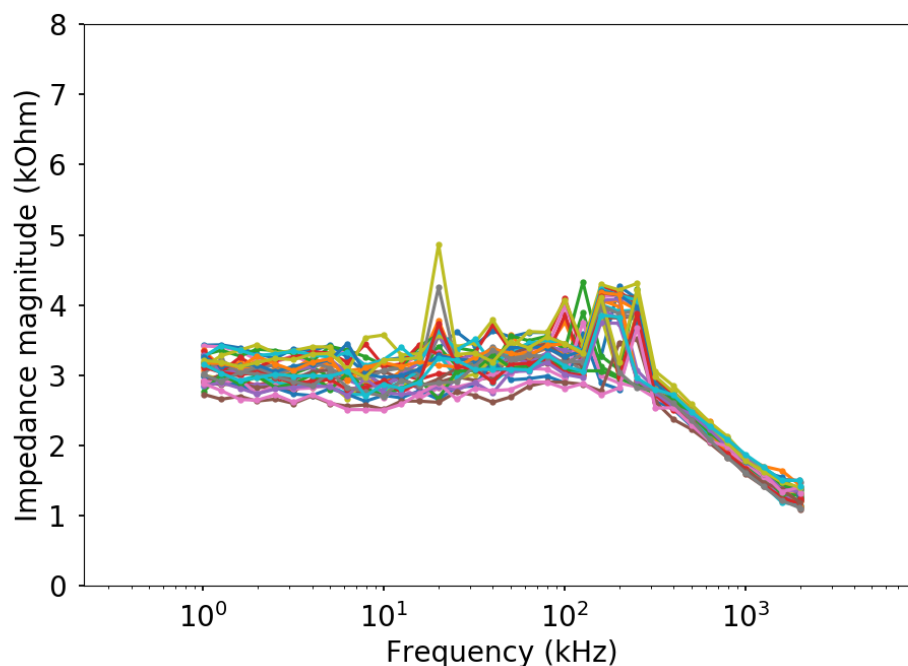


Figure 7.4: The EIS profiles of the ligated carotid artery (right) from 1 to 300 kHz with 30 permutations.

Using the impedance values at 10 kHz, we applied the same algorithm to reconstruct the EIS-derived EIT map. Without the geometry information of the vessel, we varied the lumen radius, smooth muscle cell layer thickness, and the collagen thickness to see how these parameters impact the fitness function (Eq. 5.2). The lumen radius, smooth muscle cell layer thickness, and the collagen thickness were set at 1, 3, and 1 mm, respectively, and one parameter was varied at a time with the others held constant (Fig. 7.5). Using the parameters that resulted in the lowest fitness value, we generated the EIS-derived EIT conductivity map as Fig. 7.6 shows. As the impedance profiles suggested, there was very little fatty tissue in the vessel wall. Thus, the color gradient in the conductivity map is relatively uniform and the average conductivity is around 0.45 S/m. However, this value is higher than the conductivity of smooth muscle cell suggested in the literature (Table. 6.1). Therefore, a more accurate geometry for the vessel model would be beneficial to achieve a better reconstruction result.

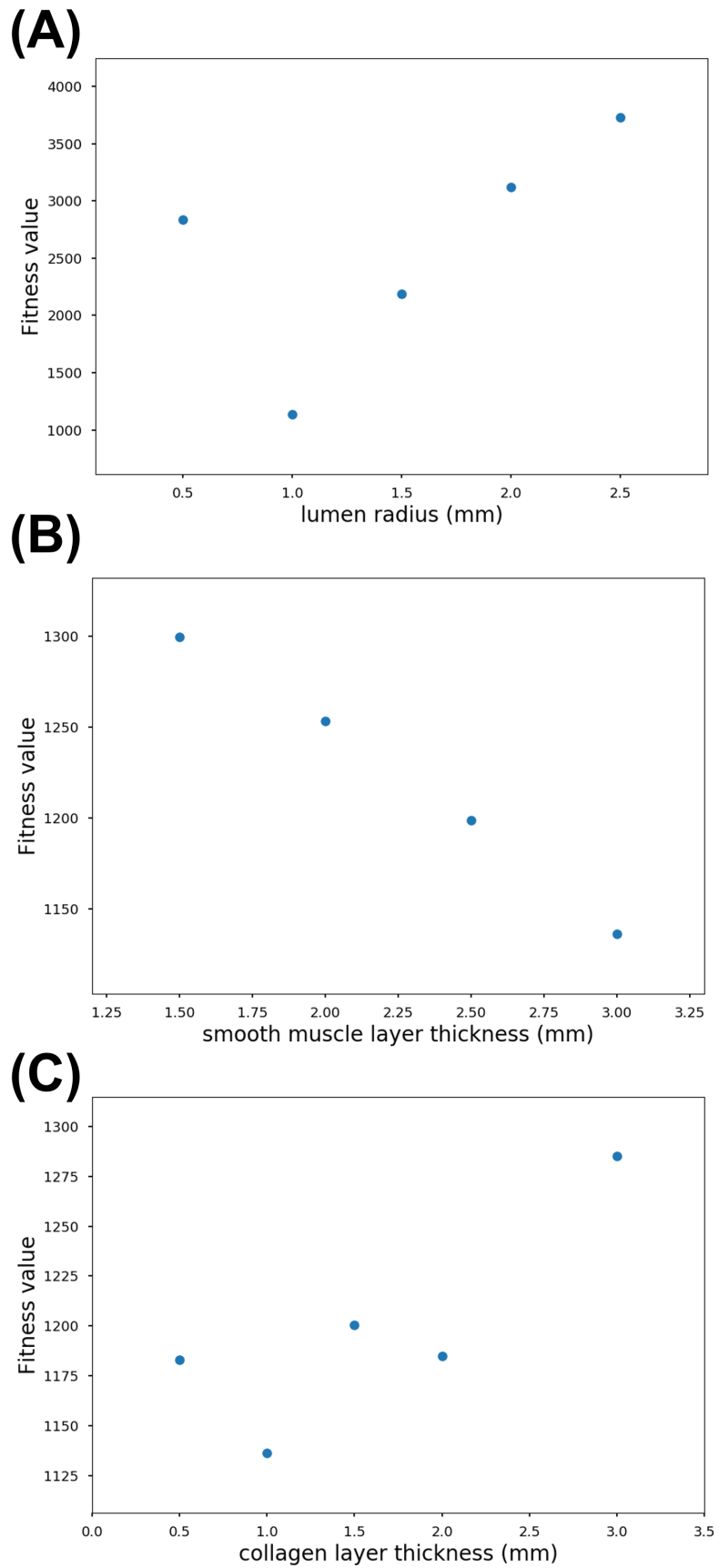


Figure 7.5: Fitness value vs dimension parameter of the vessel model including **(A)** lumen radius, **(B)** smooth muscle cell layer thickness, and **(C)** collagen layer thickness.

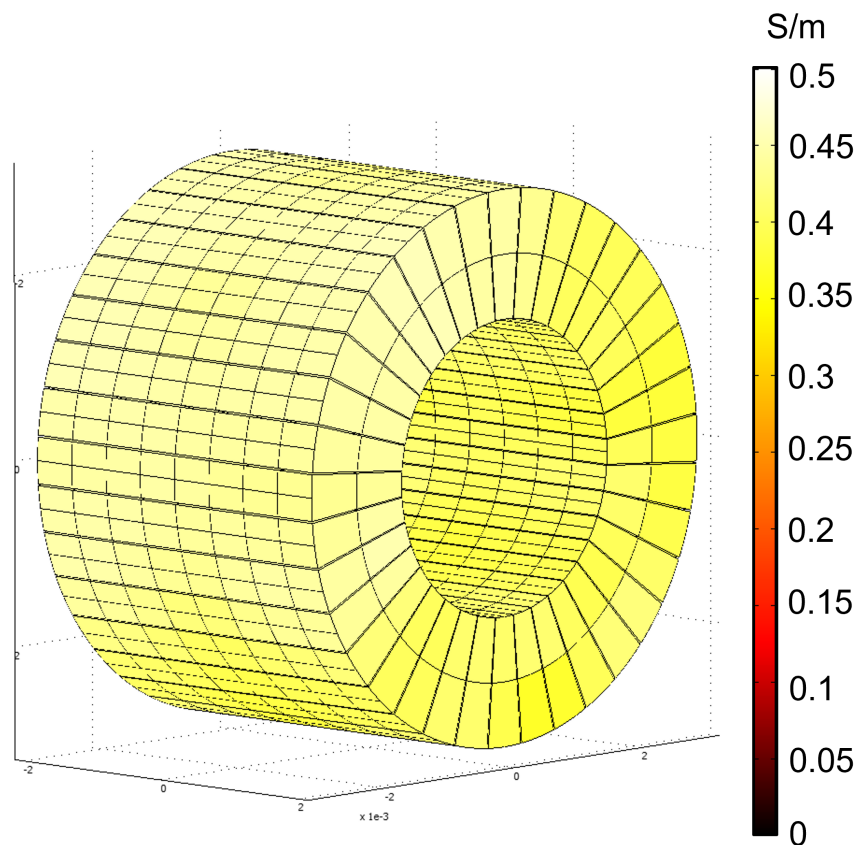


Figure 7.6: The reconstructed conductivity map using the impedance values measured by the 12-point EIS balloon catheter.

7.4 Summary

This chapter discusses the preliminary data for a 12-point EIS and the EIS-derived EIT for atherosclerosis detection. We have validated the feasibility to apply more electrode permutations. However, the optimization process for the conductivity distribution is still time consuming and would require further optimization.

*Chapter 8***FUTURE WORK**

In this final chapter, future improvements for the three projects: inward EIT for fatty liver detection (Chapters 2 and 3), outward EIT for atherosclerosis detection (Chapter 4), and EIS-derived EIT for atherosclerosis detection (Chapters 5, 6, and 7) will be discussed.

In Chapters 2 and 3, we have mentioned potential trajectories for the fatty liver EIT and have demonstrated preliminary results for 3D reconstruction and differential EIT for subcutaneous fat reconstruction. However, there is still work to be done. In terms of hardware, the current approach requires a manual connection between the ECG electrodes and the data acquisition electrode belt. An all-in-one electrode belt would be beneficial, with reusable and low contact impedance electrodes, and direct and stable wiring connections go directly to the Swisstom system. Larger electrode configurations should also be explored, i.e. 16 x 2 or 32 x 2, to increase the spacial resolution in the craniocaudal direction. Finally, as mentioned previously, stress sensors or location sensors should be combined with the EIT sensor belt to obtain the geometry information for the subjects thorax.

In regard to the EIT algorithm, a true 3D reconstruction should be investigated. Currently, only the liver boundary was reconstructed based on multiple slices of the MRI annotation, while the overall thorax boundary and subcutaneous boundary were the same along the craniocaudal direction. For the differential EIT, we reconstructed the subcutaneous fat layer using data measured at 50 kHz and 250 kHz as this data was readily available. However, we are not sure if 50 kHz and 250 kHz are the best frequency pair, showing the most distinct conductivity difference between normal tissue and fatty tissue. A thorough study examining the frequency response of fatty tissue over a wider frequency range (up to several MHz) should be conducted. Another parameter that should be considered is the injection pattern. In the past, we used a “skip 4” pattern, where 4 idle electrodes are placed between the active electrode pair to apply current and record the signal. A larger skipping pattern might allow for a deeper penetration of the current inside the thorax. In our previous fatty liver human experiments, we also collected data using skip 0, skip 1, skip 2, skip

8, and skip 14. Reconstruction of the EIT images using different injection patterns should be tested.

In Chapter 4, we demonstrated the feasibility of outward EIT on fatty tissue detection in *ex vivo* experiments. The major problem in this work is the size of the current device. In order to demonstrate the capability of the outward EIT in animal models, the diameter of the catheter should be 3-5 mm for swine carotid arteries. Also, incorporating the 32-electrode array onto the surface of a flexible balloon catheter may be another issue as the substrate of the electrodes should also be flexible. Parylene PCB is a good candidate as it is biocompatible and flexible, also it can be fabricated through a MEMS process. Just like the EIT for fatty liver detection, the electrode configuration and injection pattern should also be explored to optimize the outward fatty tissue detection. Furthermore, *a priori* knowledge might be needed for *in vivo* imaging as the geometry of the vessel will not be fixed. Using an inaccurate model may result in error in the reconstruction images. Thus a second modality may be required to obtain the lumen size, the vessel wall thickness, etc.

In Chapters 5, 6, and 7, EIS-derived EIT for plaque detection was demonstrated in swine models. The EIT images have high correlation with the histology images. As we have demonstrated in Chapter 7, a 12-point electrode array was assembled on a balloon catheter for carotid arteries measurements. However, the current device could not be deployed into coronary arteries, which are around 1-2 mm in diameter. Besides the minimization of the device, the catheter must be more flexible. The balloon catheter is usually deployed from the cut-down on femoral arteries passing through the aorta and goes to the heart. The catheter must have a large bending diameter in order to pass the aorta arch. Also, it must be able to be guided by the guide catheter and guide wire to reach the target coronary artery. New material for the catheter should be explored. Another topic that is worth studying is the robustness of the device. The fixation of the electrodes can be improved. In the past, the electrodes were detached from the balloon when the device was inserted into the shaft. An assembly method that better secures the electrodes to the balloon could improve robustness.

Another issue is the data acquisition rate. With 12 electrodes, a total of 66 permutations should be measured. Each EIS scan could take up to a minute. Since the balloon is inflated during the EIS measurements, blocking the vessel for an hour is not realistic. Downstream ischemia could cause heart failure. Multiplexers were used for faster switching of the electrode pairs, but new electronics should be built to

achieve a faster impedance scan. Another way to avoid downstream ischemia would be non-contact EIS. With precise inflation control, the electrodes could approach the vessel wall more slowly. The impedance should increase and plateau when the electrodes are close to the vessel wall with a minimum layer of conductive blood film. EIS scans when the electrodes are very close to the wall, but not in contact with the wall, might be able to obtain useful data for conductivity map reconstruction.

Besides device improvement, the reconstruction algorithm can be optimized. Currently we have implemented the genetic algorithm to create new conductivity sets. It is likely that the conductivity set is trapped in a local minimum and could take a lot of iterations to reach the global minimum. Other optimization algorithms should be considered in order to reduce the number of iterations. Also, our current model only contains 864 elements. More elements should be included to increase the resolution. As mentioned previously, just like the outward EIT, the geometry information of the vessel can greatly assist the reconstruction of the conductivity map.

BIBLIOGRAPHY

- [1] S. F. Khalil, M. S. Mohktar, and F. Ibrahim, “The theory and fundamentals of bioimpedance analysis in clinical status monitoring and diagnosis of diseases,” *Sensors*, vol. 14, no. 6, pp. 10 895–10 928, 2014.
- [2] C.-A. González-Correa, “Clinical applications of electrical impedance spectroscopy,” in *Bioimpedance in Biomedical Applications and Research*, Springer, 2018, pp. 187–218.
- [3] S. Grimnes and O. G. Martinsen, *Bioimpedance and bioelectricity basics*. Academic Press, 2011.
- [4] M. Alcañiz, J.-L. Vivancos, R. Masot, J. Ibañez, M. Raga, J. Soto, and R. Martinez-Mañez, “Design of an electronic system and its application to electronic tongues using variable amplitude pulse voltammetry and impedance spectroscopy,” *Journal of Food Engineering*, vol. 111, no. 1, pp. 122–128, 2012.
- [5] A. Manickam, A. Chevalier, M. McDermott, A. D. Ellington, and A. Hasibi, “A cmos electrochemical impedance spectroscopy (eis) biosensor array,” *IEEE Transactions on Biomedical Circuits and Systems*, vol. 4, no. 6, pp. 379–390, 2010.
- [6] D. Macdonald, “Some advantages and pitfalls of electrochemical impedance spectroscopy,” *Corrosion*, vol. 46, no. 3, pp. 229–242, 1990.
- [7] G. Walter, “A review of impedance plot methods used for corrosion performance analysis of painted metals,” *Corrosion Science*, vol. 26, no. 9, pp. 681–703, 1986.
- [8] W. Choi, H.-C. Shin, J. M. Kim, J.-Y. Choi, and W.-S. Yoon, “Modeling and applications of electrochemical impedance spectroscopy (eis) for lithium-ion batteries,” *Journal of Electrochemical Science and Technology*, vol. 11, no. 1, pp. 1–13, 2020.
- [9] R. Parsons, “The electrical double layer: Recent experimental and theoretical developments,” *Chemical Reviews*, vol. 90, no. 5, pp. 813–826, 1990.
- [10] J.-Y. Park and S.-M. Park, “Dna hybridization sensors based on electrochemical impedance spectroscopy as a detection tool,” *Sensors*, vol. 9, no. 12, pp. 9513–9532, 2009.
- [11] B.-Y. Chang and S.-M. Park, “Electrochemical impedance spectroscopy,” *Annual Review of Analytical Chemistry*, vol. 3, pp. 207–229, 2010.
- [12] J. E. Randles, “A cathode ray polarograph. part ii.—the current-voltage curves,” *Transactions of the Faraday Society*, vol. 44, pp. 327–338, 1948.

- [13] J.-L. Damez, S. Clerjon, S. Abouelkaram, and J. Lepetit, "Dielectric behavior of beef meat in the 1–1500 khz range: Simulation with the fricke/cole-cole model," *Meat Science*, vol. 77, no. 4, pp. 512–519, 2007.
- [14] L. Wu, Y. Ogawa, and A. Tagawa, "Electrical impedance spectroscopy analysis of eggplant pulp and effects of drying and freezing–thawing treatments on its impedance characteristics," *Journal of Food Engineering*, vol. 87, no. 2, pp. 274–280, 2008.
- [15] T. K. Bera, "Bioelectrical impedance methods for noninvasive health monitoring: A review," *Journal of Medical Engineering*, vol. 2014, 2014.
- [16] R. Bayford and A. Tizzard, "Bioimpedance imaging: An overview of potential clinical applications," *Analyst*, vol. 137, no. 20, pp. 4635–4643, 2012.
- [17] Y.-J. Huang, E.-Y. Huang, and K.-S. Cheng, "The correlation between extracellular resistance by electrical biopsy and the ratio of optical low staining area in irradiated intestinal tissues of rats," *Biomedical Engineering Online*, vol. 12, no. 1, pp. 1–13, 2013.
- [18] T. Whitman, J. Forrest, M. Morgan, and M. Okos, "Electrical measurement for detecting early postmortem changes in porcine muscle," *Journal of Animal Science*, vol. 74, no. 1, pp. 80–90, 1996.
- [19] T. K. Bera, J. Nagaraju, and G. Lubineau, "Electrical impedance spectroscopy (eis)-based evaluation of biological tissue phantoms to study multifrequency electrical impedance tomography (mf-eit) systems," *Journal of Visualization*, vol. 19, no. 4, pp. 691–713, 2016.
- [20] X. Bai, J. Hou, L. Wang, M. Wang, X. Wang, C. Wu, L. Yu, J. Yang, Y. Leng, and Y. Sun, "Electrical impedance analysis of pork tissues during storage," *Journal of Food Measurement and Characterization*, vol. 12, no. 1, pp. 164–172, 2018.
- [21] S. Spadaro, T. Mauri, S. H. Böhm, G. Scaramuzzo, C. Turrini, A. D. Waldmann, R. Ragazzi, A. Pesenti, and C. A. Volta, "Variation of poorly ventilated lung units (silent spaces) measured by electrical impedance tomography to dynamically assess recruitment," *Critical Care*, vol. 22, no. 1, pp. 1–9, 2018.
- [22] V. Tomicic and R. Cornejo, "Lung monitoring with electrical impedance tomography: Technical considerations and clinical applications," *Journal of Thoracic Disease*, vol. 11, no. 7, p. 3122, 2019.
- [23] B. H. Brown, "Electrical impedance tomography (eit): A review," *Journal of Medical Engineering & Technology*, vol. 27, no. 3, pp. 97–108, 2003.
- [24] M. Bodenstein, M. David, and K. Markstaller, "Principles of electrical impedance tomography and its clinical application," *Critical Care Medicine*, vol. 37, no. 2, pp. 713–724, 2009.

- [25] M. Christ, C. E. Kenig, and C. Sadosky, *Harmonic analysis and partial differential equations: essays in honor of Alberto P. Calderón*. University of Chicago Press, 2001.
- [26] E. L. Costa, R. G. Lima, and M. B. Amato, “Electrical impedance tomography,” *Yearbook of Intensive Care and Emergency Medicine*, pp. 394–404, 2009.
- [27] J. K. Seo, J. Lee, S. W. Kim, H. Zribi, and E. J. Woo, “Frequency-difference electrical impedance tomography (fdeit): Algorithm development and feasibility study,” *Physiological Measurement*, vol. 29, no. 8, p. 929, 2008.
- [28] C.-C. Chang, Z.-Y. Huang, S.-F. Shih, Y. Luo, A. Ko, Q. Cui, J. Sumner, S. Cavallero, S. Das, W. Gao, *et al.*, “Electrical impedance tomography for non-invasive identification of fatty liver infiltrate in overweight individuals,” *Scientific Reports*, vol. 11, no. 1, pp. 1–12, 2021.
- [29] Y. Luo, P. Abiri, S. Zhang, C.-C. Chang, A. H. Kaboodrangi, R. Li, A. K. Sahib, A. Bui, R. Kumar, M. Woo, *et al.*, “Non-invasive electrical impedance tomography for multi-scale detection of liver fat content,” *Theranostics*, vol. 8, no. 6, p. 1636, 2018.
- [30] Y. Z. Ider and Ö. Birgül, “Use of the magnetic field generated by the internal distribution of injected currents for electrical impedance tomography (mr-eit),” *Turkish Journal of Electrical Engineering & Computer Sciences*, vol. 6, no. 3, pp. 215–226, 2000.
- [31] A. Adler, A. Boyle, M. Crabb, H. Gagnon, B. Grychtol, N. Lesparre, and W. Lionheart, “Eidors version 3.8,” Jun. 2015. DOI: 10.5281/zenodo.17559.
- [32] J. Schöberl, “Netgen an advancing front 2d/3d-mesh generator based on abstract rules,” *Computing and Visualization in Science*, vol. 1, no. 1, pp. 41–52, 1997.
- [33] D. Chiumello, S. Froio, B. Bouhemad, L. Camporota, and S. Coppola, “Clinical review: Lung imaging in acute respiratory distress syndrome patients-an update,” *Critical Care*, vol. 17, no. 6, pp. 1–13, 2013.
- [34] I. Frerichs, M. B. Amato, A. H. Van Kaam, D. G. Tingay, Z. Zhao, B. Grychtol, M. Bodenstern, H. Gagnon, S. H. Böhm, E. Teschner, *et al.*, “Chest electrical impedance tomography examination, data analysis, terminology, clinical use and recommendations: Consensus statement of the translational eit development study group,” *Thorax*, vol. 72, no. 1, pp. 83–93, 2017.
- [35] I. Frerichs, J. Scholz, and N. Weiler, “Electrical impedance tomography and its perspectives in intensive care medicine,” in *Intensive Care Medicine*, Springer, 2006, pp. 437–447.
- [36] P. Angulo, “Nonalcoholic fatty liver disease,” *New England Journal of Medicine*, vol. 346, no. 16, pp. 1221–1231, 2002.

- [37] M. A. Castro, M. J. Fassett, T. B. Reynolds, K. J. Shaw, and T. M. Goodwin, "Reversible peripartum liver failure: A new perspective on the diagnosis, treatment, and cause of acute fatty liver of pregnancy, based on 28 consecutive cases," *American Journal of Obstetrics and Gynecology*, vol. 181, no. 2, pp. 389–395, 1999.
- [38] M. E. Rinella, "Nonalcoholic fatty liver disease: A systematic review," *Jama*, vol. 313, no. 22, pp. 2263–2273, 2015.
- [39] M. E. Rinella and A. J. Sanyal, "Management of nafld: A stage-based approach," *Nature Reviews Gastroenterology & Hepatology*, vol. 13, no. 4, pp. 196–205, 2016.
- [40] J. Chhimwal, V. Patial, and Y. Padwad, "Beverages and non-alcoholic fatty liver disease (nafld): Think before you drink," *Clinical Nutrition*, vol. 40, no. 5, pp. 2508–2519, 2021.
- [41] V. W.-S. Wong, W.-K. Chan, S. Chitturi, Y. Chawla, Y. Y. Dan, A. Duseja, J. Fan, K.-L. Goh, M. Hamaguchi, E. Hashimoto, *et al.*, "Asia-pacific working party on non-alcoholic fatty liver disease guidelines 2017—part 1: Definition, risk factors and assessment," *Journal of Gastroenterology and Hepatology*, vol. 33, no. 1, pp. 70–85, 2018.
- [42] E. Ahlqvist, P. Storm, A. Käräjämäki, M. Martinell, M. Dorkhan, A. Carlsson, P. Vikman, R. B. Prasad, D. M. Aly, P. Almgren, *et al.*, "Novel subgroups of adult-onset diabetes and their association with outcomes: A data-driven cluster analysis of six variables," *The Lancet Diabetes & Endocrinology*, vol. 6, no. 5, pp. 361–369, 2018.
- [43] M. Lazo and J. M. Clark, "The epidemiology of nonalcoholic fatty liver disease: A global perspective," in *Seminars in Liver Disease*, © Thieme Medical Publishers, vol. 28, 2008, pp. 339–350.
- [44] N. Kemmer, G. W. Neff, E. Franco, H. Osman-Mohammed, J. Leone, E. Parkinson, E. Cece, and A. Alsina, "Nonalcoholic fatty liver disease epidemic and its implications for liver transplantation," *Transplantation*, vol. 96, no. 10, pp. 860–862, 2013.
- [45] G. Marchesini, E. Bugianesi, G. Forlani, F. Cerrelli, M. Lenzi, R. Manini, S. Natale, E. Vanni, N. Villanova, N. Melchionda, *et al.*, "Nonalcoholic fatty liver, steatohepatitis, and the metabolic syndrome," *Hepatology*, vol. 37, no. 4, pp. 917–923, 2003.
- [46] H. Maeda, M. Hosokawa, T. Sashima, K. Murakami-Funayama, and K. Miyashita, "Anti-obesity and anti-diabetic effects of fucoxanthin on diet-induced obesity conditions in a murine model," *Molecular Medicine Reports*, vol. 2, no. 6, pp. 897–902, 2009.
- [47] D. C. Rockey, S. H. Caldwell, Z. D. Goodman, R. C. Nelson, and A. D. Smith, "Liver biopsy," *Hepatology*, vol. 49, no. 3, pp. 1017–1044, 2009.

- [48] A. A. Bravo, S. G. Sheth, and S. Chopra, "Liver biopsy," *New England Journal of Medicine*, vol. 344, no. 7, pp. 495–500, 2001.
- [49] J. Glen, L. Floros, C. Day, and R. Pryke, "Non-alcoholic fatty liver disease (nafld): Summary of nice guidance," *BMJ*, vol. 354, 2016.
- [50] I. D. D'Agata and W. F. Balistreri, "Evaluation of liver disease in the pediatric patient," *Pediatrics in Review*, vol. 20, pp. 376–390, 1999.
- [51] G. Shiha, A. Ibrahim, A. Helmy, S. K. Sarin, M. Omata, A. Kumar, D. Bernstien, H. Maruyama, V. Saraswat, Y. Chawla, *et al.*, "Asian-pacific association for the study of the liver (apasl) consensus guidelines on invasive and non-invasive assessment of hepatic fibrosis: A 2016 update," *Hepatology International*, vol. 11, no. 1, pp. 1–30, 2017.
- [52] N. Peleg, A. Issachar, O. Sneh-Arbib, and A. Shlomain, "Ast to platelet ratio index and fibrosis 4 calculator scores for non-invasive assessment of hepatic fibrosis in patients with non-alcoholic fatty liver disease," *Digestive and Liver Disease*, vol. 49, no. 10, pp. 1133–1138, 2017.
- [53] V. Vilgrain, M. Ronot, M. Abdel-Rehim, M. Zappa, G. d'Assignies, O. Bruno, and M.-P. Vullierme, "Hepatic steatosis: A major trap in liver imaging," *Diagnostic and Interventional Imaging*, vol. 94, no. 7-8, pp. 713–727, 2013.
- [54] S. B. Reeder, H. H. Hu, and C. B. Sirlin, "Proton density fat-fraction: A standardized mr-based biomarker of tissue fat concentration," *Journal of Magnetic Resonance Imaging: JMRI*, vol. 36, no. 5, p. 1011, 2012.
- [55] T. Yokoo, S. D. Serai, A. Pirasteh, M. R. Bashir, G. Hamilton, D. Hernando, H. H. Hu, H. Hetterich, J.-P. Kühn, G. M. Kukuk, *et al.*, "Linearity, bias, and precision of hepatic proton density fat fraction measurements by using mr imaging: A meta-analysis," *Radiology*, vol. 286, no. 2, pp. 486–498, 2018.
- [56] A. Shuster, M. Patlas, J. Pinthus, and M. Mourtzakis, "The clinical importance of visceral adiposity: A critical review of methods for visceral adipose tissue analysis," *The British Journal of Radiology*, vol. 85, no. 1009, pp. 1–10, 2012.
- [57] A. Tang, G. Cloutier, N. M. Szeverenyi, and C. B. Sirlin, "Ultrasound elastography and mr elastography for assessing liver fibrosis: Part 1, principles and techniques," *American Journal of Roentgenology*, vol. 205, no. 1, pp. 22–32, 2015.
- [58] B. H. Brown and A. D. Seagar, "The sheffield data collection system," *Clinical Physics and Physiological Measurement*, vol. 8, no. 4A, p. 91, 1987.
- [59] J. Wilkinson and V. Thanawala, "Thoracic impedance monitoring of respiratory rate during sedation—is it safe?" *Anaesthesia*, vol. 64, no. 4, pp. 455–456, 2009.

- [60] B. H. Brown, “Impedance pneumography,” *WO*, vol. 1997020499, A1, 1997.
- [61] R. Pikkemaat, S. Lundin, O. Stenqvist, R.-D. Hilgers, and S. Leonhardt, “Recent advances in and limitations of cardiac output monitoring by means of electrical impedance tomography,” *Anesthesia & Analgesia*, vol. 119, no. 1, pp. 76–83, 2014.
- [62] S. Zlochiver, D. Freimark, M. Arad, A. Adunsky, and S. Abboud, “Parametric eit for monitoring cardiac stroke volume,” *Physiological Measurement*, vol. 27, no. 5, S139, 2006.
- [63] I. Frerichs, T. Becher, and N. Weiler, “Electrical impedance tomography imaging of the cardiopulmonary system,” *Current Opinion in Critical Care*, vol. 20, no. 3, pp. 323–332, 2014.
- [64] R. H. Bayford, “Bioimpedance tomography (electrical impedance tomography),” *Annu. Rev. Biomed. Eng.*, vol. 8, pp. 63–91, 2006.
- [65] B. H. Brown, “Electrical impedance tomography (eit): A review,” *Journal of Medical Engineering & Technology*, vol. 27, no. 3, pp. 97–108, 2003.
- [66] M. Christ, C. E. Kenig, and C. Sadosky, *Harmonic analysis and partial differential equations: essays in honor of Alberto P. Calderón*. University of Chicago Press, 2001.
- [67] M. Cheney, D. Isaacson, and J. C. Newell, “Electrical impedance tomography,” *SIAM Review*, vol. 41, no. 1, pp. 85–101, 1999.
- [68] D. S. Holder, *Electrical impedance tomography: Methods, history and applications*. CRC Press, 2004.
- [69] D. Isaacson, M. Cheney, and J. C. Newell, “Comments on reconstruction algorithms,” *Clinical Physics and Physiological Measurement*, vol. 13, no. A, p. 83, 1992.
- [70] X. Zhong, M. D. Nickel, S. A. Kannengiesser, B. M. Dale, B. Kiefer, and M. R. Bashir, “Liver fat quantification using a multi-step adaptive fitting approach with multi-echo gre imaging,” *Magnetic Resonance in Medicine*, vol. 72, no. 5, pp. 1353–1365, 2014.
- [71] A. Adler, P. O. Gaggero, and Y. Maimaitijiang, “Adjacent stimulation and measurement patterns considered harmful,” *Physiological Measurement*, vol. 32, no. 7, p. 731, 2011.
- [72] C. Rücker, T. Günther, and K. Spitzer, “Three-dimensional modelling and inversion of dc resistivity data incorporating topography—i. modelling,” *Geophysical Journal International*, vol. 166, no. 2, pp. 495–505, 2006.
- [73] M. Krautblatter and C. Hauck, “Electrical resistivity tomography monitoring of permafrost in solid rock walls,” *Journal of Geophysical Research: Earth Surface*, vol. 112, no. F2, 2007.

- [74] G. Bolton, M. Bennett, M. Wang, C. Qiu, M. Wright, K. Primrose, S. Stanley, and D. Rhodes, "Development of an electrical tomographic system for operation in a remote, acidic and radioactive environment," *Chemical Engineering Journal*, vol. 130, no. 2-3, pp. 165–169, 2007.
- [75] A. P. Calderón, "On an inverse boundary value problem," *Computational & Applied Mathematics*, vol. 25, pp. 133–138, 2006.
- [76] J. K. Seo and E. J. Woo, *Nonlinear inverse problems in imaging*. John Wiley & Sons, 2012.
- [77] M. Crabb, J. Davidson, R. Little, P. Wright, A. Morgan, C. Miller, J. Naish, G. Parker, R. Kikinis, H. McCann, *et al.*, "Mutual information as a measure of image quality for 3d dynamic lung imaging with eit," *Physiological Measurement*, vol. 35, no. 5, p. 863, 2014.
- [78] P. Grasland-Mongrain, J.-M. Mari, J.-Y. Chapelon, and C. Lafon, "Lorentz force electrical impedance tomography," *Irbm*, vol. 34, no. 4-5, pp. 357–360, 2013.
- [79] M.-Y. Chen, G. Hu, W. He, Y.-L. Yang, and J.-Q. Zhai, "A reconstruction method for electrical impedance tomography using particle swarm optimization," in *Life system modeling and intelligent computing*, Springer, 2010, pp. 342–350.
- [80] A. R. S. Feitosa, R. R. Ribeiro, V. A. F. Barbosa, R. E. de Souza, and W. P. dos Santos, "Reconstruction of electrical impedance tomography images using particle swarm optimization, genetic algorithms and non-blind search," in *5th ISSNIP-IEEE Biosignals and Biorobotics Conference (2014): Biosignals and Robotics for Better and Safer Living (BRC)*, 2014, pp. 1–6.
- [81] S. J. Hamilton and A. Hauptmann, "Deep d-bar: Real-time electrical impedance tomography imaging with deep neural networks," *IEEE Transactions on Medical Imaging*, vol. 37, no. 10, pp. 2367–2377, 2018.
- [82] X. Li, Y. Zhou, J. Wang, Q. Wang, Y. Lu, X. Duan, Y. Sun, J. Zhang, and Z. Liu, "A novel deep neural network method for electrical impedance tomography," *Transactions of the Institute of Measurement and Control*, vol. 41, no. 14, pp. 4035–4049, 2019.
- [83] Z. Luo, J. Li, G. Hong, and H. Li, "Strain-based displacement field reconstruction method for thin rectangular plate through orthogonal deflection curves bridging," *Structural Control and Health Monitoring*, vol. 27, no. 1, e2457, 2020.
- [84] J. M. Khor, A. Tizzard, A. Demosthenous, and R. Bayford, "Wearable sensors for patient-specific boundary shape estimation to improve the forward model for electrical impedance tomography (eit) of neonatal lung function," *Physiological Measurement*, vol. 35, no. 6, p. 1149, 2014.

- [85] S. de Gelidi, N. Seifnaraghi, A. Bardill, A. Tizzard, Y. Wu, E. Sorantin, S. Nordebo, A. Demosthenous, and R. Bayford, "Torso shape detection to improve lung monitoring," *Physiological Measurement*, vol. 39, no. 7, p. 074001, 2018.
- [86] P. Darma, M. Baidillah, M. Sifuna, and M. Takei, "Real-time dynamic imaging method for flexible boundary sensor in wearable electrical impedance tomography," *IEEE Sensors Journal*, vol. 20, no. 16, pp. 9469–9479, 2020.
- [87] J. K. Seo, J. Lee, S. W. Kim, H. Zribi, and E. J. Woo, "Frequency-difference electrical impedance tomography (fdeit): Algorithm development and feasibility study," *Physiological Measurement*, vol. 29, no. 8, p. 929, 2008.
- [88] B. Sun, M. R. Baidillah, P. N. Darma, T. Shirai, K. Narita, and M. Takei, "Evaluation of the effectiveness of electrical muscle stimulation on human calf muscles via frequency difference electrical impedance tomography," *Physiological Measurement*, vol. 42, no. 3, p. 035008, 2021.
- [89] T. Menden, J. Orschulik, S. Dambrun, J. Matuszczyk, S. A. Santos, S. Leonhardt, and M. Walter, "Reconstruction algorithm for frequency-differential eit using absolute values," *Physiological Measurement*, vol. 40, no. 3, p. 034008, 2019.
- [90] Y. Luo, D. Huang, Z.-Y. Huang, T. K. Hsiai, and Y.-C. Tai, "An ex vivo study of outward electrical impedance tomography (oeit) for intravascular imaging," *IEEE Transactions on Biomedical Engineering*, 2021.
- [91] P. A. Hasgall, E. Neufeld, M.-C. Gosselin, A. Klingenböck, N. Kuster, P. A. Hasgall, and M.-C. Gosselin, "It'is database for thermal and electromagnetic parameters of biological tissues," 2012.
- [92] R. R. S. Packard, Y. Luo, P. Abiri, N. Jen, O. Aksoy, W. M. Suh, Y.-C. Tai, and T. K. Hsiai, "3-d electrochemical impedance spectroscopy mapping of arteries to detect metabolically active but angiographically invisible atherosclerotic lesions," *Theranostics*, vol. 7, no. 9, p. 2431, 2017.
- [93] D.-H. Kim, N. Lu, R. Ghaffari, Y.-S. Kim, S. P. Lee, L. Xu, J. Wu, R.-H. Kim, J. Song, Z. Liu, *et al.*, "Materials for multifunctional balloon catheters with capabilities in cardiac electrophysiological mapping and ablation therapy," *Nature Materials*, vol. 10, no. 4, pp. 316–323, 2011.
- [94] W. Li, D. C. Rodger, A. Pinto, E. Meng, J. D. Weiland, M. S. Humayun, and Y.-C. Tai, "Parylene-based integrated wireless single-channel neurostimulator," *Sensors and Actuators A: Physical*, vol. 166, no. 2, pp. 193–200, 2011.
- [95] E. Meng, P.-Y. Li, and Y.-C. Tai, "A biocompatible parylene thermal flow sensing array," *Sensors and Actuators A: Physical*, vol. 144, no. 1, pp. 18–28, 2008.

- [96] A. Adler, A. Boyle, M. Crabb, H. Gagnon, B. Grychtol, N. Lesparre, and W. Lionheart, "Eidors version 3.8 proc. of the 16th int," in *Conf. on Biomedical Applications of Electrical Impedance Tomography (Neuchâtel, Switzerland, 2–5 June)*, vol. 19, 2015.
- [97] M. Kumar, M. Husain, N. Upreti, and D. Gupta, "Genetic algorithm: Review and application," *Available at SSRN 3529843*, 2010.
- [98] V. P. Rolnik and P. Seleglim Jr, "A specialized genetic algorithm for the electrical impedance tomography of two-phase flows," *Journal of the Brazilian Society of Mechanical Sciences and Engineering*, vol. 28, pp. 378–389, 2006.
- [99] G.-P. Shi, I. Bot, and P. T. Kovanen, "Mast cells in human and experimental cardiometabolic diseases," *Nature Reviews Cardiology*, vol. 12, no. 11, pp. 643–658, 2015.
- [100] J. Hurtubise, K. McLellan, K. Durr, O. Onasanya, D. Nwabuko, and J. F. Ndisang, "The different facets of dyslipidemia and hypertension in atherosclerosis," *Current Atherosclerosis Reports*, vol. 18, no. 12, pp. 1–12, 2016.
- [101] L. H. Arroyo and R. T. Lee, "Mechanisms of plaque rupture: Mechanical and biologic interactions," *Cardiovascular Research*, vol. 41, no. 2, pp. 369–375, 1999.
- [102] B. J. Maron, W. J. McKenna, G. K. Danielson, L. J. Kappenberger, H. J. Kuhn, C. E. Seidman, P. M. Shah, W. H. Spencer, P. Spirito, F. J. Ten Cate, *et al.*, "American college of cardiology/european society of cardiology clinical expert consensus document on hypertrophic cardiomyopathy: A report of the american college of cardiology foundation task force on clinical expert consensus documents and the european society of cardiology committee for practice guidelines," *Journal of the American College of Cardiology*, vol. 42, no. 9, pp. 1687–1713, 2003.
- [103] A. P. Burke, A. Farb, G. T. Malcom, Y.-h. Liang, J. Smialek, and R. Virmani, "Coronary risk factors and plaque morphology in men with coronary disease who died suddenly," *New England Journal of Medicine*, vol. 336, no. 18, pp. 1276–1282, 1997.
- [104] R. Virmani, F. D. Kolodgie, A. P. Burke, A. Farb, and S. M. Schwartz, "Lessons from sudden coronary death: A comprehensive morphological classification scheme for atherosclerotic lesions," *Arteriosclerosis, Thrombosis, and Vascular Biology*, vol. 20, no. 5, pp. 1262–1275, 2000.
- [105] R. Virmani, A. P. Burke, A. Farb, and F. D. Kolodgie, "Pathology of the vulnerable plaque," *Journal of the American College of Cardiology*, vol. 47, no. 8S, pp. C13–C18, 2006.
- [106] P. R. Moreno, "Vulnerable plaque: Definition, diagnosis, and treatment," *Cardiology Clinics*, vol. 28, no. 1, pp. 1–30, 2010.

- [107] M. Ouimet, H. N. Ediriweera, U. M. Gundra, F. J. Sheedy, B. Ramkhelawon, S. B. Hutchison, K. Rinehold, C. van Solingen, M. D. Fullerton, K. Cecchini, *et al.*, “MicroRNA-33–dependent regulation of macrophage metabolism directs immune cell polarization in atherosclerosis,” *The Journal of Clinical Investigation*, vol. 125, no. 12, pp. 4334–4348, 2015.
- [108] S. Solanki, P. R. Dube, L. Birnbaumer, and G. Vazquez, “Reduced necrosis and content of apoptotic m1 macrophages in advanced atherosclerotic plaques of mice with macrophage-specific loss of *trpc3*,” *Scientific reports*, vol. 7, no. 1, pp. 1–11, 2017.
- [109] G. Chinetti-Gbaguidi, S. Colin, and B. Staels, “Macrophage subsets in atherosclerosis,” *Nature Reviews Cardiology*, vol. 12, no. 1, pp. 10–17, 2015.
- [110] R. Vergallo and F. Crea, “Atherosclerotic plaque healing,” *New England Journal of Medicine*, vol. 383, no. 9, pp. 846–857, 2020.
- [111] I. Cuadrado, M. Saura, B. Castejón, A. M. Martín, I. Herruzo, N. Balatsos, J. L. Zamorano, and C. Zaragoza, “Preclinical models of atherosclerosis. the future of hybrid pet/mr technology for the early detection of vulnerable plaque,” *Expert Reviews in Molecular Medicine*, vol. 18, 2016.
- [112] G. N. Levine, E. R. Bates, J. C. Blankenship, S. R. Bailey, J. A. Bittl, B. Cercek, C. E. Chambers, S. G. Ellis, R. A. Guyton, S. M. Hollenberg, *et al.*, “2011 accf/aha/scai guideline for percutaneous coronary intervention: A report of the american college of cardiology foundation/american heart association task force on practice guidelines and the society for cardiovascular angiography and interventions,” *Journal of the American College of Cardiology*, vol. 58, no. 24, e44–e122, 2011.
- [113] G. J. W. Bech, B. De Bruyne, N. H. Pijls, E. D. De Muinck, J. C. Hoorn-tje, J. Escaned, P. R. Stella, E. Boersma, J. Bartunek, J. J. Koolen, *et al.*, “Fractional flow reserve to determine the appropriateness of angioplasty in moderate coronary stenosis: A randomized trial,” *Circulation*, vol. 103, no. 24, pp. 2928–2934, 2001.
- [114] P. A. Tonino, B. De Bruyne, N. H. Pijls, U. Siebert, F. Ikeno, M. vant Veer, V. Klauss, G. Manoharan, T. Engstrøm, K. G. Oldroyd, *et al.*, “Fractional flow reserve versus angiography for guiding percutaneous coronary intervention,” *New England Journal of Medicine*, vol. 360, no. 3, pp. 213–224, 2009.
- [115] B. De Bruyne, W. F. Fearon, N. H. Pijls, E. Barbato, P. Tonino, Z. Piroth, N. Jagic, S. Mobius-Winckler, G. Rioufol, N. Witt, *et al.*, “Fractional flow reserve–guided pci for stable coronary artery disease,” *New England Journal of Medicine*, vol. 371, no. 13, pp. 1208–1217, 2014.
- [116] D. J. Kereiakes, R. W. Yeh, J. M. Massaro, P. Driscoll-Shempp, D. E. Cutlip, P. G. Steg, A. H. Gershlick, H. Darius, I. T. Meredith, J. Ormiston, *et al.*, “Antiplatelet therapy duration following bare metal or drug-eluting

- coronary stents: The dual antiplatelet therapy randomized clinical trial,” *JAMA*, vol. 313, no. 11, pp. 1113–1121, 2015.
- [117] B. De Bruyne, N. H. Pijls, B. Kalesan, E. Barbato, P. A. Tonino, Z. Piroth, N. Jagic, S. Möbius-Winkler, G. Rioufol, N. Witt, *et al.*, “Fractional flow reserve–guided pci versus medical therapy in stable coronary disease,” *New England Journal of Medicine*, vol. 367, no. 11, pp. 991–1001, 2012.
- [118] N. H. Pijls, N. Tanaka, and W. F. Fearon, “Functional assessment of coronary stenoses: Can we live without it?” *European Heart Journal*, vol. 34, no. 18, pp. 1335–1344, 2013.
- [119] U. Siebert, B. Bornschein, P. Schnell-Inderst, J. Rieber, N. Pijls, J. Wasem, and V. Klauss, “Measurement of fractional flow reserve to guide decisions for percutaneous coronary intervention,” *GMS Health Technology Assessment*, vol. 4, 2008.
- [120] F. Sharif and R. T. Murphy, “Current status of vulnerable plaque detection,” *Catheterization and Cardiovascular Interventions*, vol. 75, no. 1, pp. 135–144, 2010.
- [121] K. Mizuno, A. Miyamoto, K. Satomura, A. Kurita, M. Sakurada, S. Yanagida, H. Nakamura, and T. Arai, “Angioscopic coronary macromorphology in patients with acute coronary disorders,” *The Lancet*, vol. 337, no. 8745, pp. 809–812, 1991.
- [122] J. A. Schaar, F. Mastik, E. Regar, C. A. den Uil, F. J. Gijsen, J. J. Wentzel, P. W. Serruys, and A. W. van der Stehen, “Current diagnostic modalities for vulnerable plaque detection,” *Current Pharmaceutical Design*, vol. 13, no. 10, pp. 995–1001, 2007.
- [123] N. Bom, W. Li, A. Van Der Steen, C. Lancee, E. Cespedes, C. Slager, and C. De Korte, “Intravascular imaging,” *Ultrasonics*, vol. 36, no. 1-5, pp. 625–628, 1998.
- [124] W. M. Suh, A. H. Seto, R. J. Margey, I. Cruz-Gonzalez, and I.-K. Jang, “Intravascular detection of the vulnerable plaque,” *Circulation: Cardiovascular Imaging*, vol. 4, no. 2, pp. 169–178, 2011.
- [125] T. Yonetsu and I.-K. Jang, “Advances in intravascular imaging: New insights into the vulnerable plaque from imaging studies,” *Korean Circulation Journal*, vol. 48, no. 1, pp. 1–15, 2018.
- [126] S. A. Boppart, B. E. Bouma, C. Pitris, J. F. Southern, M. E. Brezinski, and J. G. Fujimoto, “In vivo cellular optical coherence tomography imaging,” *Nature Medicine*, vol. 4, no. 7, pp. 861–865, 1998.
- [127] G. J. Tearney, I.-K. Jang, and B. E. Bouma, “Optical coherence tomography for imaging the vulnerable plaque,” *Journal of Biomedical Optics*, vol. 11, no. 2, p. 021 002, 2006.

- [128] F. Yu, X. Dai, T. Beebe, and T. Hsiai, “Electrochemical impedance spectroscopy to characterize inflammatory atherosclerotic plaques,” *Biosensors and Bioelectronics*, vol. 30, no. 1, pp. 165–173, 2011.
- [129] H. Cao, F. Yu, Y. Zhao, N. Scianmarello, J. Lee, W. Dai, N. Jen, T. Beebe, R. Li, R. Ebrahimi, *et al.*, “Stretchable electrochemical impedance sensors for intravascular detection of lipid-rich lesions in new zealand white rabbits,” *Biosensors and Bioelectronics*, vol. 54, pp. 610–616, 2014.
- [130] Z.-S. Shi, L. Feng, X. He, A. Ishii, J. Goldstine, H. Vinters, and F. Vinuela, “Vulnerable plaque in a swine model of carotid atherosclerosis,” *American Journal of Neuroradiology*, vol. 30, no. 3, pp. 469–472, 2009.
- [131] F.-F. Zhou, Y.-h. Liu, P.-C. Ge, Z.-H. Chen, X.-Q. Ding, J.-Y. Liu, Q.-W. Jia, F.-H. An, L.-H. Li, L.-S. Wang, *et al.*, “Coronary artery diameter is inversely associated with the severity of coronary lesions in patients undergoing coronary angiography,” *Cellular Physiology and Biochemistry*, vol. 43, no. 3, pp. 1247–1257, 2017.
- [132] A. Adler and A. Boyle, “Electrical impedance tomography: Tissue properties to image measures,” *IEEE Transactions on Biomedical Engineering*, vol. 64, no. 11, pp. 2494–2504, 2017.

Appendix A

EIT RECONSTRUCTION CODE

```

%%%%%%%%%%%%%%%%%%%%%%%%%%%%%%%%%%%%%%%%%%%%%%%%%%%%%%%%%%%%%%%%%%%%%%%% Set Parameters %%%%%%%%%
tic
skip = 4 ; %skip pattern
inj_current = 0.04;
%unit is Amp; range: 0.001~0.05, minimum step: 0.001
contact_imp = 10; %in ohm range: 1-20; minimum step: 1
hp =40e-4;
%hyperparameter range (regularization parameter): 1e-5 ~ 1e-3;
minimum step: 1e-5
zeros = get_v_data(['file path', 'skip4_zero_ignore2.txt']);
%zero_ignore0, zero_ignore1, zero_ignore2

%%%%%%%%%%%%%%%%%%%%%%%%%%%%%%%%%%%%%%%%%%%%%%%%%%%%%%%%%%%%%%%%%%%%%%%% Import data %%%%%%%%%
datadir = 'file path';
vi = get_v_data([datadir, 'data.txt']);%

%%%%%%%%%%%%%%%%%%%%%%%%%%%%%%%%%%%%%%%%%%%%%%%%%%%%%%%%%%%%%%%%%%%%%%%% Reconstruction FEM Model %%%%%%%%%
n = 32; % electrode number
%%%%%%%%%%%%%%%%%%%%%%%%%%%%%%%%%%%%%%%%%%%%%%%%%%%%%%%%%%%%%%%%%%%%%%%% electrode shape_str code %%%%%%%%%
[shape_str, elec_pos, elec_shape, elec_obj] =
mk_inward_ring_elec(n);

%%%%%%%%%%%%%%%%%%%%%%%%%%%%%%%%%%%%%%%%%%%%%%%%%%%%%%%%%%%%%%%%%%%%%%%% thorax shape code %%%%%%%%%
% abdomen boundary
thorax_2f = [x1, x2, ...
            y1, y2, ...]';
thxf = thorax./80;

% subcutaneous fat boundary
subQ = [x1, x2, ...
        y1, y2, ...]';

```

```

bb = subQ./80;

shape = { 0,          % height= 0 for 2D, nonzero for 3D
         {thxf,bb},  % contours
         [4,20],     % perform smoothing with 50 points
         0.02};     % small maxh (fine mesh)

elec_pos = [ 32,      % number of elecs per plane
            1]';     % equidistant spacing
% third parameter can be added for 3D, a single z-plane

elec_shape = [0.05]; % radius
% for 3D
% elec_shape = [0.05, % radius
%              0,     % circular electrode
%              0.05 ]'; % maxh (electrode refinement)

fmdl = ng_mk_extruded_model(shape, elec_pos, elec_shape);
% make the FEM model
figure(1);
imdl = select_imdl(fmdl);
clf; show_fem(fmdl);

% Set stimulation patterns. Use meas_current
imdl.fwd_model.stimulation = mk_stim_patterns(n,1,[0 skip+1],
[0 skip+1],{'meas_current'},inj_current);
imdl.fwd_model.meas_select = zeros;

for i = 1:n;
    imdl.fwd_model.electrode(i).z_contact = contact_imp;
end

% obtain the coordinate for each mesh
ctrs= interp_mesh(imdl.fwd_model);
xe= ctrs(:,1); ye= ctrs(:,2); %ze = ctrs(:,3); for 3D

```

```

%%%%%%%%%%%%%%%%%%%%%%%%%%%%%%%%%%%%%%%%%%%%%%%%%%%%%%%%%%%%%%%%%%%%%%%%%% liver boundary %%%%%%%%%%%
%%% marker slice%%%
Im=imread('file path'); % read in the liver annotation
Im_binary = Im/255;

% for finding the boundary for specific region
Border= bwboundaries(Im_binary, 'noholes');
Boundary=Border{1,1}; % export the data from cell struct
liver_b = Boundary;
liver_b(:,1) = -192/2+Boundary(:,2);
liver_b(:,2) = -Boundary(:,1)+168/2;
liver_b = liver_b./80;
[in,on] = inpolygon(xe,ye,liver_b(:,1),liver_b(:,2));
index=(in(:)==1);
liver = in ;
% obtain the mesh coordinate that is within the liver

%%%%%%%%%%%%%%%%%%%%%%%%%%%%%%%%%%%%%%%%%%%%%%%%%%%%%%%%%%%%%%%%%%%%%%%%%% Set Solver Params %%%%%%%%%%%
imdl.solve = @inv_solve_abs_GN_constrain ;
imdl.parameters.term_tolerance= 1.1e-5;
imdl.parameters.max_iterations=1;
imdl.hyperparameter.value=
hp*ones(1,length(imdl.fwd_model.elems))+ hp*5*liver';
% setting the regularization parameter
imdl.inv_solve.calc_solution_error = 0;
imdl.reconst_type= 'static';
imdl.RtR_prior = @prior_laplace;
imdl.parameters.min_s = 0.0;
imdl.parameters.max_s = 0.6;
imdl.jacobian_bkgnd.value = 0.32*ones(size(fmdl.elems,1),1);
imdl.jacobian_bkgnd.value( fmdl.mat_idx{1} ) = 0.1;

%%%%%%%%%%%%%%%%%%%%%%%%%%%%%%%%%%%%%%%%%%%%%%%%%%%%%%%%%%%%%%%%%%%%%%%%%% Reconstruction begins %%%%%%%%%%%
rec_img = inv_solve(imdl,vi);

liver_mean_GN = mean(rec_img.elem_data(liver))

```

```
% average liver conductivity
liver_std_GN = std(rec_img.elem_data(liver)) % std

%%%%%%%%%%%%%%%%%%%%%%%%%%%%%%%%%%%%%%%%%%%%%%%%%%%%%%%%%%%%%%%%%%%%%%%%%% Result image display %%%%%%%%%%%%%%%
img_max = (max(rec_img.elem_data)+min(rec_img.elem_data))/2;
img_ref = img_max;

calc_colours('defaults');
calc_colours('cmap_type','blue_white_red');
PLANE = [inf,inf,0];

rec_img.calc_colours.npoints = 128*4;
rec_img.calc_colours.ref_level = 0.3;
rec_img.calc_colours.clim = 0.3;

figure(2);
show_slices(rec_img,PLANE);

axis equal
axis off
axis tight

%%%%%%%%%%%%%%%%%%%%%%%%%%%%%%%%%%%%%%%%%%%%%%%%%%%%%%%%%%%%%%%%%%%%%%%%%% Reconstruction end %%%%%%%%%%%%%%%
toc
```

Appendix B

EIS RECONSTRUCTION CODE

Forward Solve

```

function impedance = forward_solve(conductance)
%%%%%%%%%%%%%%%%%%%%%%%%%%%%%%%%%%%%%%%%%%%%%%%%%%%%%%%%%%%%%%%%%%%%%%%% Model parameters %%%%%%%%%%
n_elec = 6; %Number of electrode
r_lumen = 1.6;
r_wall = 3;
length = 4; %Height of vessel
conduct = max(conductance);%Conductivity

n=6; %electrode number
inj_current=0.00001; %50 mV/5k ohm 0.01 mA

%%%%%%%%%%%%%%%%%%%%%%%%%%%%%%%%%%%%%%%%%%%%%%%%%%%%%%%%%%%%%%%%%%%%%%%% Model parameters %%%%%%%%%%
incyl = sprintf('cylinder(0,0,%f; 0,0,%f; %f)',-1,1,r_lumen);
cyl = sprintf('cylinder(0,0,%f; 0,0,%f; %f)',-1,1,r_wall);
p1 = sprintf('plane(0,0,%f;0,0,1)',length/2);%z plan
p2 = sprintf('plane(0,0,%f;0,0,-1)',-length/2);

%%%%%%%%%%%%%%%%%%%%%%%%%%%%%%%%%%%%%%%%%%%%%%%%%%%%%%%%%%%%%%%%%%%%%%%% Electrode %%%%%%%%%%
[elec_pos, elec_shape, elec_obj] =
make_ring_electrodes_2(n_elec, r_lumen, 'incyl');
elec_shape = [0.2, 0.6, 0.2]; % width length mesh size

shape_str = [ 'solid p1= ',p1,';\n'...
'solid p2= ',p2,';\n'...
'solid incyl = ',incyl,';\n' ...
'solid cyl = ',cyl,';\n'...
'solid mainobj = cyl and p1 and p2 and not incyl -maxh=0.3;\n'...
'tlo mainobj;\n'];

```

```

%%%%%%%%%%%%%%%%%%%%%%%%%%%%%%%%%%%%%%%%%%%%%%%%%%%%%%%%%%%%%%%%%%%%%%%%%% Forward model %%%%%%%%%%%%%%%
impedance = [];
for skip = 0:n-2
    skip = 0;
        fmdl = ng_mk_gen_models(shape_str, elec_pos,
            elec_shape, elec_obj);%Generate model
        fmdl.stimulation = mk_stim_patterns(n,1,[0 skip+1],
            [0 skip+1],{'meas_current'},inj_current);

%     figure(1)
%     show_fem(fmdl,[0,1]);
%check if the electrodes are correct

%%%%%%%%%%%%%%%%%%%%%%%%%%%%%%%%%%%%%%%%%%%%%%%%%%%%%%%%%%%%%%%%%%%%%%%%%% Forward solve and Inclusion applied %%%%%%%%%%%%%%%
        img_i = mk_image(fmdl,conduct);

        ctrs= interp_mesh(img_i.fwd_model);
        xe= ctrs(:,1); ye= ctrs(:,2); ze= ctrs(:,3);
        r_half = (r_lumen + r_wall)/2;

        layer = 8;
        theta = 10;
        ring = 3;
        deltaz = length/layer;
        n_element = ring*layer*360/theta;
        block_array = zeros(size(xe,1), n_element);
        block_array = logical(block_array);
        re = sqrt((xe).^2+(ye).^2);

        %%%inner ring%%
        for i = 1:8
            for j = 1: 9
                temp = (re < r_half & -length/2+ deltaz*(i-1) <ze

```

```

& ze <-length/2+ deltaz*i
& ye-tan((2*j-1)*(theta/2)*pi/180)*xe <0
& ye-tan((2*j-3)*(theta/2)*pi/180)*xe >0);
block_array(:,360/theta*(i-1)+j) = temp;
end
for j = 10:10
temp = (re < r_half & -length/2+ deltaz*(i-1) <ze
& ze <-length/2+ deltaz*i
& ye-tan((2*j-1)*(theta/2)*pi/180)*xe >0
& ye-tan((2*j-3)*(theta/2)*pi/180)*xe >0);
block_array(:,360/theta*(i-1)+j) = temp;
end
for j = 11:18
temp = (re < r_half & -length/2+ deltaz*(i-1) <ze
& ze <-length/2+ deltaz*i
& ye-tan((2*j-1)*(theta/2)*pi/180)*xe >0
& ye-tan((2*j-3)*(theta/2)*pi/180)*xe <0);
block_array(:,360/theta*(i-1)+j) = temp;
end
for j = 19:27
temp = (re < r_half & -length/2+ deltaz*(i-1) <ze
& ze <-length/2+ deltaz*i
& ye-tan((2*(j-18)-1)*(theta/2)*pi/180)*xe >0
& ye-tan((2*(j-18)-3)*(theta/2)*pi/180)*xe <0);
block_array(:,360/theta*(i-1)+j) = temp;
end
for j =28:28
temp = (re < r_half & -length/2+ deltaz*(i-1) <ze
& ze <-length/2+ deltaz*i
& ye-tan((2*(j-18)-1)*(theta/2)*pi/180)*xe <0
& ye-tan((2*(j-18)-3)*(theta/2)*pi/180)*xe <0);
block_array(:,360/theta*(i-1)+j) = temp;
end
for j =29:36
temp = (re < r_half & -length/2+ deltaz*(i-1) <ze
& ze <-length/2+ deltaz*i

```

```

        & ye-tan((2*(j-18)-1)*(theta/2)*pi/180)*xe <0
        & ye-tan((2*(j-18)-3)*(theta/2)*pi/180)*xe >0);
        block_array(:,360/theta*(i-1)+j) = temp;
    end
end

%%%outer ring%%%%%
for i = 1:8
    for j = 1: 9
        temp = (re > r_half & re < r_wall
        & -length/2+ deltaz*(i-1) <ze
        & ze <-length/2+ deltaz*i
        & ye-tan((2*j-1)*(theta/2)*pi/180)*xe <0
        & ye-tan((2*j-3)*(theta/2)*pi/180)*xe >0);
        block_array(:,360/theta*(i-1)+j+288) = temp;
    end
    for j = 10:10
        temp = (re > r_half & re < r_wall
        & -length/2+ deltaz*(i-1) <ze
        & ze <-length/2+ deltaz*i
        & ye-tan((2*j-1)*(theta/2)*pi/180)*xe >0
        & ye-tan((2*j-3)*(theta/2)*pi/180)*xe >0);
        block_array(:,360/theta*(i-1)+j+288) = temp;
    end
    for j = 11:18
        temp = (re > r_half & re < r_wall
        & -length/2+ deltaz*(i-1) <ze
        & ze <-length/2+ deltaz*i
        & ye-tan((2*j-1)*(theta/2)*pi/180)*xe >0
        & ye-tan((2*j-3)*(theta/2)*pi/180)*xe <0);
        block_array(:,360/theta*(i-1)+j+288) = temp;
    end
    for j = 19:27
        temp = (re > r_half & re < r_wall
        & -length/2+ deltaz*(i-1) <ze

```

```

    & ze <-length/2+ deltaz*i
    & ye-tan((2*(j-18)-1)*(theta/2)*pi/180)*xe >0
    & ye-tan((2*(j-18)-3)*(theta/2)*pi/180)*xe <0);
    block_array(:,360/theta*(i-1)+j+288) = temp;
end
for j =28:28
    temp = (re > r_half & re < r_wall
    & -length/2+ deltaz*(i-1) <ze
    & ze <-length/2+ deltaz*i
    & ye-tan((2*(j-18)-1)*(theta/2)*pi/180)*xe <0
    & ye-tan((2*(j-18)-3)*(theta/2)*pi/180)*xe <0);
    block_array(:,360/theta*(i-1)+j+288) = temp;
end
for j =29:36
    temp = (re > r_half & re < r_wall
    & -length/2+ deltaz*(i-1) <ze
    & ze <-length/2+ deltaz*i
    & ye-tan((2*(j-18)-1)*(theta/2)*pi/180)*xe <0
    & ye-tan((2*(j-18)-3)*(theta/2)*pi/180)*xe >0);
    block_array(:,360/theta*(i-1)+j+288) = temp;
end
end

%%collagen ring%%
for i = 1:8
    for j = 1: 9
        temp = (re > r_wall & -length/2+ deltaz*(i-1) <ze
        & ze <-length/2+ deltaz*i
        & ye-tan((2*j-1)*(theta/2)*pi/180)*xe <0
        & ye-tan((2*j-3)*(theta/2)*pi/180)*xe >0);
        block_array(:,360/theta*(i-1)+j+576) = temp;
    end
    for j = 10:10
        temp = (re > r_wall & -length/2+ deltaz*(i-1) <ze
        & ze <-length/2+ deltaz*i
        & ye-tan((2*j-1)*(theta/2)*pi/180)*xe >0

```

```

        & ye-tan((2*j-3)*(theta/2)*pi/180)*xe >0);
        block_array(:,360/theta*(i-1)+j+576) = temp;
    end
    for j = 11:18
        temp = (re > r_wall & -length/2+ deltaz*(i-1) <ze
        & ze <-length/2+ deltaz*i
        & ye-tan((2*j-1)*(theta/2)*pi/180)*xe >0
        & ye-tan((2*j-3)*(theta/2)*pi/180)*xe <0);
        block_array(:,360/theta*(i-1)+j+576) = temp;
    end
    for j = 19:27
        temp = (re > r_wall & -length/2+ deltaz*(i-1) <ze
        & ze <-length/2+ deltaz*i
        & ye-tan((2*(j-18)-1)*(theta/2)*pi/180)*xe >0
        & ye-tan((2*(j-18)-3)*(theta/2)*pi/180)*xe <0);
        block_array(:,360/theta*(i-1)+j+576) = temp;
    end
    for j =28:28
        temp = (re > r_wall & -length/2+ deltaz*(i-1) <ze
        & ze <-length/2+ deltaz*i
        & ye-tan((2*(j-18)-1)*(theta/2)*pi/180)*xe <0
        & ye-tan((2*(j-18)-3)*(theta/2)*pi/180)*xe <0);
        block_array(:,360/theta*(i-1)+j+576) = temp;
    end
    for j =29:36
        temp = (re > r_wall & -length/2+ deltaz*(i-1) <ze
        & ze <-length/2+ deltaz*i
        & ye-tan((2*(j-18)-1)*(theta/2)*pi/180)*xe <0
        & ye-tan((2*(j-18)-3)*(theta/2)*pi/180)*xe >0);
        block_array(:,360/theta*(i-1)+j+576) = temp;
    end
end

%assign conductivance to each block

for a = 1: n_element

```

```
        block = block_array(:,a);
        img_i.elem_data(block) = conductance(a);
    end

    vi = fwd_solve(img_i);%calculate voltage

    vi_result = [vi.meas(1)
                vi.meas(8)
                vi.meas(15)
                vi.meas(22)
                vi.meas(29)];
    impedance = [impedance; vi_result];
end
impedance = impedance/inj_current;
impedance(10)=[];%drop the values we don't need
impedance(13:14)=[];
impedance(15:17)=[];
impedance(16:19)=[];
end
```

Genetic Algorithm

```

tic
impedance_meas = get_v_data(['file path','EIS_data.txt']);
conductance = get_v_data_2(['file path','initial.txt']);
%conductance values for each block

sigma = 1.3;
low = min(conductance);
high = max(conductance);

for ii = 1:99
    data = conductance+0.0002*randn(size(conductance));
    data_t = conductance;
    conductance = data;
    impedance_GA = forward_solve(conductance);
    temp(ii) = norm(impedance_GA - impedance_meas);
    population(:,ii) = data;
    conductance = data_t;
end
population(:,100) = conductance;
temp(100) = norm(forward_solve(conductance) - impedance_meas);
population_t = [temp; population];
p=population_t';
pt=sortrows(p);
pt(:,1)=[];
pt=pt';
random_v=rand(10,1);
sum_random=sum(random_v);
random_v=random_v./sum_random;
sum_p=pt(:,1)+pt(:,2)+pt(:,3)+pt(:,4)+pt(:,5)
+pt(:,6)+pt(:,7)+pt(:,8)+pt(:,9)+pt(:,10);

for u=1:100
for kk=1:10
    data = pt(:,kk);
    data_t = conductance;

```

```

    conductance = data;
    impedance_GA = forward_solve(conductance);
    temp_elite(kk) = norm(impedance_GA - impedance_meas);
    conductance = data_t;
end

for jj=1:90
    random_v=rand(10,1);
    sum_random=sum(random_v);
    random_v=random_v./sum_random;
    population_d(:,jj)=
    (sigma*random_v(1)*pt(:,1)+(1-sigma)*random_v(1)*sum_p/10)
    +(sigma*random_v(2)*pt(:,2)+(1-sigma)*random_v(2)*sum_p/10)
    +(sigma*random_v(3)*pt(:,3)+(1-sigma)*random_v(3)*sum_p/10)
    +(sigma*random_v(4)*pt(:,4)+(1-sigma)*random_v(4)*sum_p/10)
    +(sigma*random_v(5)*pt(:,5)+(1-sigma)*random_v(5)*sum_p/10)
    +(sigma*random_v(6)*pt(:,6)+(1-sigma)*random_v(6)*sum_p/10)
    +(sigma*random_v(7)*pt(:,7)+(1-sigma)*random_v(7)*sum_p/10)
    +(sigma*random_v(8)*pt(:,8)+(1-sigma)*random_v(8)*sum_p/10)
    +(sigma*random_v(9)*pt(:,9)+(1-sigma)*random_v(9)*sum_p/10)
    +(sigma*random_v(10)*pt(:,10)+(1-sigma)*random_v(10)*sum_p/10);
    impedance_GA = forward_solve(population_d(:,jj));
    temp_d(jj) = norm(impedance_GA - impedance_meas);
end

    random_mut = randsample(1:90, 5);
for x=1:5
    random_mut_2 = randsample(1:864, 10);
for y=1:10
    population_d(random_mut_2(y),random_mut(x))
    = low + (high-low)*rand(1,1);
end
end

temp_dd=[temp_d,temp_elite];
popu_des=[population_d,pt(:,1:10)];

```

```
population_t=[temp_dd;popu_des];
p=population_t';
pt=sortrows(p);
pt(:,1)=[];
pt=pt';
random_v=rand(10,1);
sum_random=sum(random_v);
random_v=random_v./sum_random;
sum_p=pt(:,1)+pt(:,2)+pt(:,3)+pt(:,4)+pt(:,5)
+pt(:,6)+pt(:,7)+pt(:,8)+pt(:,9)+pt(:,10);
count=u
end
conductance = pt(:,1);
impedance_GA = forward_solve(conductance);
temp_min = norm(impedance_GA - impedance_meas);
toc
```